HYDROKINETIC ENERGY HARNESSING BY ENHANCEMENT OF FLOW INDUCED MOTION USING PASSIVE TURBULENCE CONTROL

by

Che-Chun Chang

A dissertation submitted in partial fulfillment
of the requirements for the degree of
Doctor of Philosophy
(Naval Architecture and Marine Engineering)
in The University of Michigan
2010

Doctoral Committee:

Professor Michael M. Bernitsas, Chair
Professor Armin W. Troesch
Associate Professor Bogdan Epureanu
Ajith Kumar Raghavan

To my parents,
Jenny Chen and Jack Chang.

ACKNOWLEDGEMENTS

Completion of this dissertation represents an important milestone in my life. Though my name will be the only one that appears on the cover of this dissertation, this work would have not been possible to complete without the support from many people to whom I owe my gratitude.

My deepest gratitude is to my advisor, Dr. Michael M. Bernitsas, who convincingly conveyed a spirit of adventure in regard to scientific research and scholarship. I will never forget the day I failed my first qualification examination. Professor Bernitsas's encouragement brought me out from the darkest days in my life. It is because of his continuous support, I have been able to explore, to experiment, and to learn from failures in my graduate life and overcome obstacles here at the University of Michigan. Without his guidance, I could not have reached this important stage of scholarship.

It is an honor for me to dedicate this work to my parents, Shueh-Bin Chang and Jin-Mian Chen, who have raised and educated me with their unconditional love. My parents are the ones showing me the joy of intellectual pursuit ever since my childhood. Their encouragement has walked me through unexpected challenges, and their teaching has cultivated me into who I am today. Without my parents, I could not have accomplished numerous challenging tasks in my life. There are no adequate words to express my appreciation to them. Thank you, dad and mom. I would also like to thank my grandmother, my brother, Joe Chang, and my sister-in-law, Tsu-Min Yeh. I can't imagine where would I be without my family.

I have also derived determination and perseverance from Tina Chen, my fiance with whom I am fortunate enough to share my life. I thank her for always supporting me with her faith and love. It is through her eyes that I could see my ability to conquer the fear, to release the worry, and to carve a future.

In addition, my work would not have been complete without the help and support from many friends with whom I have shared my graduate life here in Ann Arbor. I would like to express my immerse gratitude to my ex-roommates, Joe Chou, Chia-Yin Lin, and Hsien-Chang Lin, who have made my life in the past four years colorful. I would also like to thank Wei-Wei Yu, a great friend that I am incredibly fortunate to have in my life in Ann Arbor.

Collective and individual acknowledgements are also owed to my colleagues, Ajith Kumar, Hong-Rae Park, Eun Soo Kim. We have spent numerous days and nights in the laboratory and the office. We worked as a team, we shared the successes and failures in countless experiments, and we certainly will have a life-long friendship after the completion of this dissertation.

The following support is gratefully acknowledged: (1) ONR grant N00014-03-1-0983 to the University of Michigan, Program Manager Kelly Copper. (2) ONR grant N00014-08-1-0601 to the University of Michigan, Program Manager Kelly Copper. (3) NSF-SBIR grant to Vortex Hydro Energy and the University of Michigan award # IIP-0810426, Program Manager William Haynes.

Last but not least, I would like to thank everyone who was important to the successful realization of this thesis. Also, I would like to convey my apology to all the important people that I failed to acknowledge by name in this relatively short statement.

TABLE OF CONTENTS

LIST OF FIGURES

LIST OF TABLES

GLOSSARY

Greek symbols

α	Angle of attack
α_{PTC}	PTC placement angle measured from front
α'	(m*+Ca). ζ_{total}, Product of sum of mass ratio and added mass coefficient with damping ratio
Φ_{max}	$\tan(\Phi_{max}) = 2\pi A^*/U^*$, maximum flow incidence angle
μ	Fluid dynamic viscosity
ν	Fluid kinematic viscosity
ζ	Damping ratio = $\frac{c}{2\sqrt{Km}}$
ζ_{harn}	Additional damping ratio for energy harnessing
$\zeta_{structure}$	Structural damping ratio
ζ_{system}	$\zeta_{system} = \zeta_{structure} + \zeta_{harn}$
ζ_{total}	Total damping ratio exerted on cylinder including hydrodynamic damping. $\zeta_{total}=\zeta_{system}+\zeta_{fluid}$
η_{max}	Max. Energy conversion (efficiency)

Roman symbols

A	Oscillation amplitude
A_{max}	Max. ten amplitude ratio
A*	A/D, Amplitude ratio
A^*_M	A*/log10(0.41 Re0.36)
A^*_{max}	A_{max}/D, Maximum amplitude ratio
Ca	Potential added mass coefficient of a cylinder
C_D	Drag coefficient

c_{harn}	Nm/s, extra damping for energy harnessing
$c_{structure}$	Nm/s, structural damping
c_{system}	Nm/s, $c_{system} = c_{structure} + c_{harn}$
c_{total}	Nm/s, total damping ratio exerting on cylinder including hydrodynamic damping
C_y	Hydrodynamic lift-force coefficient
F_{fluid}	Fluid force
D	Diameter of cylinder
$f_{n,\ water}$	Natural frequency in water in = Hz, $\frac{1}{2\pi}\sqrt{\frac{K}{m_{osc}+m_a}}$
f_{osc}	Body oscillation frequency in Hz,
f_v	Vortex-shedding frequency in Hz,
f*	$f^*=f_{osc}/f_{n,water}$, oscillation frequency ratio
K	Stiffness in N/m
K_{spring}	Spring stiffness in N/m
$K_{virtual}$	Virtual stiffness generated by motor in N/m
k	Roughness grit size
L	Cylinder length
m_d	Water mass displaced by cylinder
m_{osc}	Oscillating mass
m*	Mass ratio
m_a	Added mass
p	Sieve thickness of PTC in mm,
Re	Reynolds number based on diameter = U*D/ν
S	Strouhal number = f_v*D/U
S_G	Skop-Griffin parameter = 2π*3S*2*(m*ζtotal)
U	Flow velocity in m/s or knots,
U*	$U^* = U / (f_{n,\ water} D)$, reduced velocity
U^*_{start}	Beginning reduced velocity of lower branch
U^*_{end}	End reduced velocity of lower branch

ABSTRACT

Horizontal Marine Hydro-Kinetic (MHK) energy in the form of currents/tides/rivers is worldwide available. The vast majority flows at speeds slower than 3 knots while turbines require an average of 5-7knots to be financially viable. The VIVACE Converter (Vortex Induced Vibration for Aquatic Clean Energy) is an innovative energy converter, which is highly scalable and can thus extract energy from even slow flows using the potentially disastrous phenomenon of Vortex Induced Vibrations (VIV) or galloping. Due to the self-limiting nature of VIV, the range of synchronization and the amplitude of oscillation restrict the amount of energy generated.

The goal of this thesis is to enable VIVACE to attain higher power generation with higher efficiency using high damping required for energy harnessing. Passive Turbulence Control (PTC) utilizing roughness strips is developed and tested experimentally to enhance Flow Induced Motion (FIM). Experiments are conducted for $4\times10^4<Re<1.2\times10^5$ using PTC on a circular cylinder undergoing VIV and galloping. PTC is applied as straight roughness strips at specific circumferential locations on a circular cylinder surface to alter its FIM in a steady flow. Effectively, geometry is changed to non-circular, which results in a flow incidence angle, leading to high-amplitude oscillations known as galloping. All model tests were conducted with broad-field laser visualization at $4\times10^4<Re<1.2\times10^5$ in the Marine Renewable Energy Laboratory of the University of Michigan. The following observations and conclusions are made: (1) PTC coverage of

16° is effective in the range of 10°-64°. (2) PTC reduces VIV amplitudes, but extends the VIV synchronization range followed by high-amplitude galloping. (3) Galloping initiates at a critical reduced velocity $U^*_{gallop,}$ manifests to fully-developed galloping with no reduced velocity upper-end reached. (4) U^*_{gallop} is found to depend primarily on the PTC location. (5) Galloping amplitude of 3 diameters is achieved. (6) Wake structures change dramatically reaching up to ten vortices shed per cycle of galloping oscillation. (7) The higher the surface roughness, the higher is the maximum amplitude of galloping oscillation within the tested roughness range. (8) Two important cross-sectional geometry parameters have been identified and can be used to predict the onset of galloping of a circular cylinder with PTC. (9) Optimal harnessed power envelop of VIVACE converter with PTC was generated for $0.4m/s<U<1.45m/s$.

CHAPTER 1

MARINE RENEWABLE ENERGY CONVERSION

1.1. Introduction

In order to combat global warming, the awareness of harvesting and using renewable energy has been raised in many developed countries. Specifically, European Union leaders reached an agreement in March 2007 that 20% of the energy consumed by the area should be produced from renewable sources in order to cut carbon dioxide emissions in five years. Among all the renewable energy sources, ocean represents an invaluable alternative energy source today, as oceans cover more than 70% of the Earth's surface. Such a renewable energy source calls for invention and development of new mechanical devices to utilize this gift from nature.

Flexibly mounted circular cylinders exposed to fluid flow are known to experience flow-induced vibrations (Leonardo DaVinci 1504). Vortex-induced oscillation is the most commonly noticed hydrodynamic excitation caused due to the formation of a vortex street in the wake of a cylinder. The vortex street is formed due to the alternating shedding of vortices from either side of the cylinder. Each time a vortex is shed from the body, it alters the local pressure distribution around the body and, consequently, the body experiences a time-varying force at the frequency of vortex shedding. For a flexibly mounted cylinder, when the vortex shedding frequency approaches the natural frequency of the spring-cylinder system, the body would be excited to significant amplitudes with the shedding frequency 'locked-in' to the oscillation frequency. During 'lock-in', the cylinder oscillates at or near the natural frequency of the system and vortex shedding is synchronized with the oscillation frequency.

Bernitsas and Raghavan (2007) have been successful in utilizing this potentially dis-

astrous phenomenon, Vortex-Induced Vibration (VIV), to generate power with their invention of the VIVACE (Vortex-Induced Vibration for Aquatic Clean Energy) converter. VIVACE has been patented through University of Michigan. It is to be emphasized that, the existing ocean energy harnessing devices for horizontal MHK (Marine Hydro Kinetic) energy such as water-mills and turbines are efficient only for current speeds greater than 4 knots and financially viable for average speed 5-7 knots. The VIVACE converter, on the other hand, is highly scalable to convert fluid power to electricity in the flow speed range of 0.8 knots to 3 knots and beyond. Yet, due to the self-limiting nature of VIV, harnessed power from single VIVACE is constrained by the limited oscillating amplitude and synchronization range.

In an attempt to overcome this limitation, research initiatives are undertaken to further enhance the cylinder excitation levels and thus, the power harnessed. Experiments were carried out on a surface-modified circular-cylinder, at the Low-Turbulence Free Surface Water Channel (LTFSW Channel) of the Marine Hydrodynamics Laboratory (MHL). The surface modification is brought about by employing straight, waterproof, sandpaper strips applied along the entire span of the cylinder at some specific circumferential locations. Thus, the test-geometry employed throughout this study is a circular cylinder fitted with roughness strips and these strips act as Passive Turbulence Control (PTC). Effects of roughness height, strip location, and strip area coverage on the Flow-Induced Motion (FIM) are investigated in this study. Apart from Vortex-Induced Vibrations, high amplitude galloping oscillations are also observed when applying the PTC in this research. Apart from advancing the power output of the VIVACE converter, the results of this research reveal quite interesting features of cylinder vibrations, particularly regarding the galloping phenomenon.

As is well known, a smooth circular cylinder cannot gallop in isolated conditions (Y. H. Nakamura, 1994), whereas, various non-circular sections could be subjected to large amplitude galloping oscillations (Y. H. Nakamura, 1994; Parkinson, 1979). VIV of circular sections is commonly observed in many engineering applications such as cooling towers, chimneys, heat exchangers, pipeline suspension bridges etc. VIV could occur both in the cross-flow and in-line directions, but cross-flow vibrations are in general significantly

more severe than the in-line oscillations (J. J. Mercier 1973, F. S. Hover, 1998; Sarpkaya 2004, Williamson 1988). As mentioned earlier, all non-circular cross-sections are susceptible to galloping. Non-circular shape causes wake structure asymmetry on either sides of the body and this in turn, creates an additional lift force in the direction of the body motion in cross-flow direction resulting in the so-called galloping instability. The cross-sectional geometry with PTC employed in the present study, effectively being a non-circular section, is highly prone to galloping instability besides VIV. Further, the wake structures around the oscillating smooth as well as rough cylinder are also analyzed as part of the present investigation. A mathematical model of galloping is applied to all the experimental results to fully investigate galloping on circular cylinder with surface roughness on particular location. Two significant cross-sectional geometry factors were found and verified by the experimental results. Thus, the results of this investigation proved to be quite interesting both with regard to the physics of the oscillatory features of the test-cylinder and also with regard to the promising energy harnessing potential thereof.

The first VIVACE machine built by Bernitsas et al (2006, 2007) at the University of Michigan, Ann Arbor consists of a spring-mounted circular cylinder capable of executing cross flow oscillations when mounted in a uniform, steady fluid flow. Their efforts are further extended in the present study by additionally utilizing a virtual damping (V_{ck}) system (Lee 2009). Harnessed power is calculated by means of introduction of virtual damping into the system.

In this thesis, harnessed energy calculation results with smooth and rough cylinders show that VIVACE is enabled to attain higher efficiency successfully by extending VIV and triggering galloping. With the application of PTC, the maximum power density of VIVACE (349 W/m^3) is amplified 1.38 times than that of VIVACE with smooth surface cylinder (253 W/m^3) at flow speed U= 1.45m/s.

1.2. Literature review

In this section, a review of the literature on the following areas is presented: ocean energy conversion, vortex induced vibrations, galloping, and effect of surface roughness

on flow past a body.

1.2.1. Ocean energy conversion

Until today, numerous devices have been designed and patented, along with several pilot programs launched to test the viability and efficiency for alternative energy production. However, each had its flaws that prevented further development due to inability to satisfy CEC (California Energy Commission) requirements. Some of the examples are given below:

a) Converters based on surface oscillation, namely, water column, buoy, flap, or pendulum (Thorpe, 1998), have high-energy output only in a very narrow band of wave frequencies near resonance.
b) Converters of wind or tidal current energy (turbines, water-mills) can extract energy proportional to their projected surface at efficiency of 15-30% and only for currents stronger than 2m/sec (~4 knots), below which they do not function efficiently (Pontes, M.T., & Falcao, A., 2001).
c) Tidal energy converters require at least a 5m head, and are very large and as obtrusive and damaging to the environment as water dams. They also require a 5~7-year construction period and significant initial capital cost (Pontes, M.T., & Falcao, A., 2001).
d) Most of the converters operate near shore and occupy valuable coastal real estate.
e) Converters such as water mills, turbines, or tidal dams disturb marine life.

In summary, previous designs of ocean energy converters, as listed above, failed to meet life-cycle cost targets, high-energy density, while being unobtrusive with low maintenance cost, and being robust with a minimum of 10-year service life. How to produce an efficient and viable energy converter that satisfies these requirements still remains a challenge to the today engineering/scientific world. Such a challenge has been the focus for more than 40 years of international efforts particularly in Europe and Japan while to a lesser extent in the United States (Pontes, M.T. & Falcao, A., 2001; Thorpe, T.W., 1992, 1998). Meanwhile, with the recent oil-spill incident in 2010, it is inevitable that the United States will join this global brainstorming effort in search of a universally acceptable converter. The present investigation is, in one sense, a promising effort in this direc-

tion and no doubt it has to be continued till it practically becomes a fully viable means of power generation in the future.

1.2.2. Vortex induced vibrations

The phenomenon of Vortex Induced Vibrations (VIV) of circular cylinders, which are flexible or rigid but mounted on springs, has been studied extensively in the past one hundred years. As mentioned before, alternating vortex shedding creates alternating surface pressure fluctuations generating oscillatory lift forces on the body (cylinder). Major body oscillations take place perpendicular to the flow direction. Thus, the cylinder undergoing VIV absorbs energy from the fluid flow. This phenomenon has been observed in several engineering disciplines: offshore (pipelines, marine risers, cables, legs of drilling and production platforms, etc); nuclear (fuel rods in reactors); mechanical (heat exchangers); civil (bridges, flag poles). As an inherently nonlinear, self-excited phenomenon, researchers have been working for decades on how to eliminate or at least regulate this unsteady fluid-structure interaction phenomenon since it has been identified as the major cause for many structural failures. Unlike the previous efforts to suppress the occurrence of this phenomenon, VIVACE works on enhancing VIV to maximize it and convert the power extracted from the fluid flow into electrical power.

As mentioned before, during VIV, the oscillation frequency and vortex shedding frequency 'locked-in' where the body oscillations control the shedding process. This 'lock-in' phenomenon is also known as "synchronization, wake capture, hydro-elastic fluid-elastic oscillations, or self-excited oscillations" (Sarpkaya 1979). During the 'lock-in' phenomenon, as the flow velocity increases, the body oscillation frequency (f_{osc}) and vortex-shedding frequency (f_v) collapse together into a broad range of reduced velocity U*, which is closer to the natural system frequency ($f_{n,\ water}$). U* is defined as

$$U^* = U / (f_{n,water} D)$$

It is notable that the cylinder oscillation is a function of mass ratio. During 'lock-in', for systems with high mass ratios (such as in air), the cylinder oscillates at or very near the natural frequency of the system with the frequency of vortex shedding synchronized

with the body oscillation frequency. In other words, under the lock-in condition, $f_n \sim f_{osc}$ when the VIV system is operating in air. In contrary, for VIV systems with low mass ratios (such as in water), the oscillation frequency could deviate significantly from the vortex shedding frequency due to the effect of added mass, m_a (Khalak and Williamson, 1997; Sarpkaya 1979, 2004). This aspect bears specific importance to the present study as it is conducted using water as the fluid medium. VIV could occur both in the cross flow and in-line directions, but cross flow vibrations are in general significantly more severe than in-line oscillations (J.J. Mercier 1973, F. S. Hover, 2001).

1.2.3. Galloping

Galloping is known to be a single degree of freedom, high-amplitude, low frequency oscillation typically experienced by non-circular cross-section bodies (Blevins, 1977). The galloping generation-mechanism is the interruption of communication between separated upper and lower flows. Because communication of two separated flows tend to induce pressure difference on upper and lower surfaces of cylinder. In hydrokinetics, such an interrupting communication between two separated flows can be accomplished by the following three mechanisms: (1) Adding a long downstream splitter plate behind the body in its wake. (2) A vanishing effect of wake undulation at low wind velocity related with low-speed galloping (LSG). (3) A critical geometry at high wind velocity producing a reattachment-type pressure distribution caused by separated-flow/edge interaction related with high-speed galloping (HSG) (H. Sakamoto, 2005). Karman vortex shedding is produced by communication of upper and lower separated flows. In other words, Karman vortex shedding promotes communication between two separated flows. Therefore, the interruption of this communication between two separated flows should be identical to the interruption of Karman vortex shedding. It can be further explained that mitigation or suppression of Karman vortex shedding can excite galloping instability.

Non-circular sections (such as square) could be subjected to large amplitude galloping oscillations (Parkinson and Sullivan, 1979; Bokaian and Geoola, 1984b). Circular sections with attachment (such as splitter plate) could experience galloping (Nakamura et al., 1994). Furthermore, proximity of another cylinder would also induce galloping excitation in circular cylinders (Bokain and Geoola, 1984a). These studies on galloping of

circular cylinders bring to light the fact that a fluid dynamic change brought about by virtue of attachments or proximity to other bodies may cause galloping in circular cylinders. This aspect is relevant to the context of the present study where the geometry of the circular cylinder is altered by attaching roughness strips on its surface.

1.2.4. Effect of surface roughness on flow past body

To understand the effect of PTC (selectively distributed surface roughness in the form of sand strips) on the flow around a circular cylinder, it is important to consider the effect of edge of the sand strip and also the roughness protrusion of the strip on the flow.

The edge of PTC acts like a 'step' and in a sense acts like a tripping wire being conjugated with three-dimensional roughness. The flow around the cylinder with trip wire has been classified into three patterns by Igarashi as shown in Figure 1.1. In pattern A, the flow reattaches in a laminar manner beyond the wire with a separation bubble. In pattern C, the flow reattaches with a separation bubble as a turbulent boundary layer, and in pattern D, the flow separates at the wire. Pattern C is the transition regime between A and D. It can be seen that, separation bubble formation occurs in cases A and C. Separation bubble was observed by Higuchi et al (Higuchi et al. 1989a) at Re= 8×10^4 and it existed in the range 60° - 90° from the stagnation point occurring in cells along the cylinder span. Recently, Huang et al. (2006) observed a separation bubble at a lower Reynolds number of Re> 5.5×10^4 (Figure 1.2). In general, a separation bubble is classified based on the nature of the boundary layer at the separation and reattachment points, as it could be laminar, transitional or turbulent. For a laminar separation bubble, the boundary layer is laminar at both the separation and reattachment points, while for a transitional bubble the boundary layer is laminar at separation and turbulent at reattachment. For a turbulent separation bubble, the boundary layer is turbulent at both the separation and reattachment points. Pattern A in Figure 1.1 is similar to the separation bubble on a smooth cylinder when the Reynolds number is $5.5\times10^4<Re<1\times10^5$. In addition, a separation bubble is characterized by its length and height and accordingly, it is classified as 'short' and 'long'. Since it alters the nature of boundary layer interaction with the body surface, it is expected to influence the flow-induced motions as well. It could also be noted that, in the case of isolated roughness like tripping wire, earlier formation of separation bubble can

be induced (Igarashi, 1986). These cases of trip-wire (Figure 1.1) are presented here since similar boundary layer interactions could be expected to occur in the present research, i.e., with roughness strips applied on the cylinder surface.

Introducing roughness around a bluff body initiates early transition of boundary layer and it also results in the elimination of few flow regimes (Zdravkovich, 1997). Achenbach and Heinecke (1981) noted that the transition of critical Reynolds number is reduced for a circular cylinder as the roughness height is increased as shown by the following relation:

$$\mathrm{Re}_{critical} = \frac{6000}{(k_s/D)^{1/2}} \tag{1.1}$$

In equation (1.1), k_s is the sand-grain roughness height and D is the cylinder diameter.

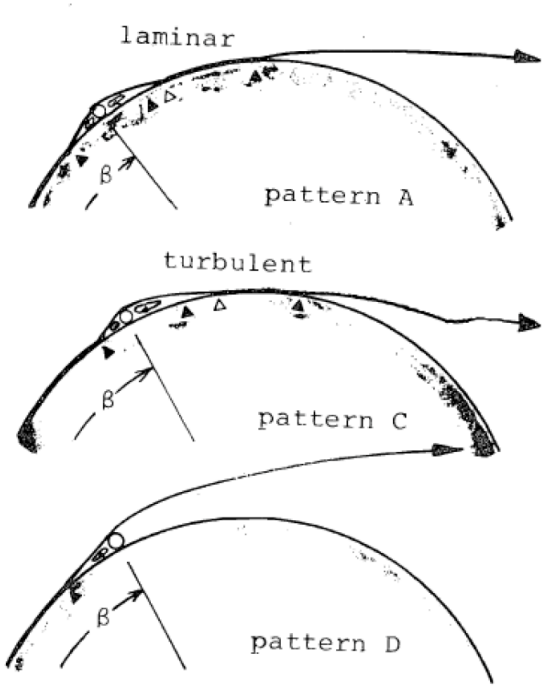

Figure 1.1. Flow around circular cylinder with trip wire (Huang et al. 2006)

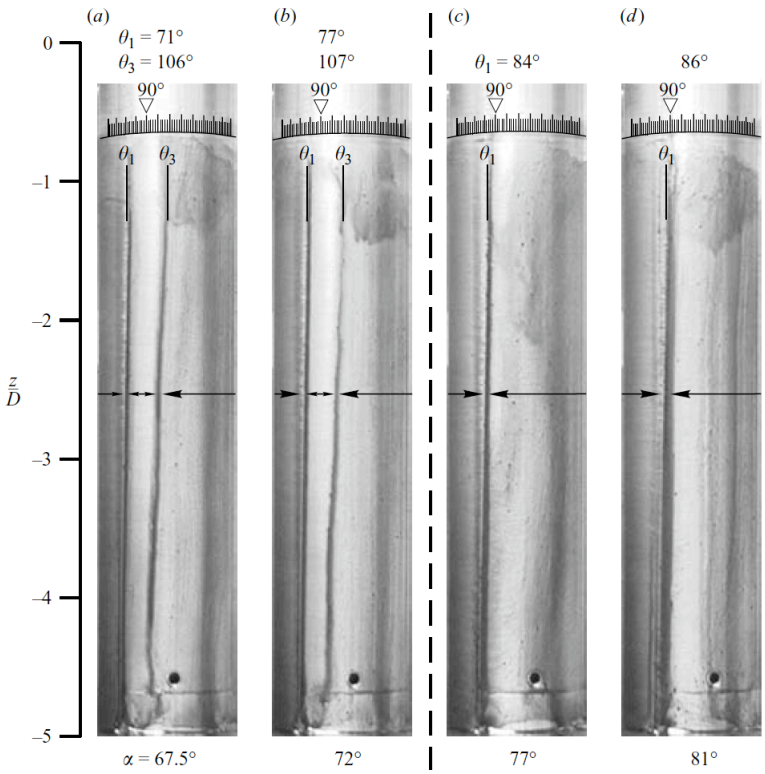

Figure 1.2. Surface oil-flow patterns of a modulated circular cylinder at ReD = 0.5×10^5. (a) α = 67.5◦, (b) 72◦, (c) 77◦, (d) 81◦. (Huang et al. 2006)

In the experimental work presented in this dissertation, a circular cylinder is geometrically modified using straight roughness strips (PTC) placed on the cylinder surface. Furthermore, roughness is selectively applied on the surface of the cylinder in contrast to most of the previous studies where roughness is uniformly distributed over the entire cylinder surface (Achenbach 1971, Guven et al., 1980; Achenbach and Heinecke, 1981; Nakamura and Tomonari, 1982). Width, roughness height, and circumferential location of the roughness strips (PTC) are varied to investigate their effect on the cylinder oscillatory characteristics. It is specifically pointed out that, the majority of the previous studies involving surface roughness were aimed at studying features like surface pressure distribution, flow separation and Strouhal number characteristics and were not focused on the hydrodynamic excitation of the body. Dynamic response is of high practical value particularly with regard to energy conversion, such as the one undertaken in the present research.

1.3. VIVACE converter

The VIVACE Converter is an energy conversion device operating based on the fundamental phenomenon of Flow-Induced Motion (FIM), particularly Vortex-Induced Vibrations (VIV) and galloping. It was invented by Bernitsas and Raghavan (2006) and is the first ocean energy converter aiming to utilize FIM and produce energy from this natural phenomenon.

In its simplest form, the converter modulus consists of an elastically mounted (real springs) circular cylinder. Basically, a flexibly mounted circular cylinder undergoes FIM when it is subjected to fluid flow. Hence, this self-excited vibration of the cylinder is what is available to harness energy in VIVACE. This mechanical energy is converted to electrical energy through a generator.

1.3.1. System description

When VIVACE was first designed and built in 2006, a real spring system was used with physical bearings and a motor to generate power from VIV. Under these conditions, VIVACE functions according to the following principles (Bernitsas, 2008).

a) *Vortex-induced vibrations of a rigid circular cylinder mounted on linear springs:* The VIV phenomenon has been known to be disastrous to structures particularly since the Tacoma Narrows bridge collapse in 1940. Previous efforts focused on spoiling vortex-shedding consequently suppressing VIV. However, VIVACE Converter works with an entirely opposite perception on VIV. It exploits the flow-induced vibrations to generate useful power and electricity. The more vigorous VIV, the more MHK energy is converted to mechanical energy in the VIVACE cylinders.
b) *Non-linear resonance:* Unlike other Ocean energy Convertors functioning under the principle of linear resonance (i.e. boys, water columns), the VIVACE Convertor has more productive operating range of power generation. Specifically, as discussed in the previous sections, for the VIVACE Convertor, the oscillating body frequency locks onto the vortex shedding frequency over a broad range of Reynolds number during VIV. In addition, the body oscillations control the shedding process. Vortices are shed at about the natural frequency of the system over a broad range of flow ve-

locity in apparent violation of the Strouhal relationship.

c) *Correlation length:* In Vortex-Induced Vibrations, correlation length is defined as the body span over which the vortex shedding is occurring nearly in phase. Theoretically, the higher the correlation length, the higher is the induced lift force implying higher amplitude of oscillations. The VIVACE Converter is designed with an aspect ratio (*L/D)* in the range of $7 < L/D < 20$.

d) *Electricity generation:* A belt and gear system transmits the mechanical energy to a generator to convert it to electrical energy. It is important to acknowledge the role of system damping for the VIVACE Convertor. When the damping is too high, VIV is suppressed. On the other hand, if the system damping is too small, energy harnessing will be negligible. This principle is especially important in the context of the present study since introduction of passive turbulence control (PTC) alters the total system damping, which will be discussed in detail in the chapters 10.

The elements of a VIVACE module are as follows: a rigid circular cylinder of diameter D and length L, two supporting linear springs, one or more generators, and a gear box for transmission of harnessed power. The cylinder is placed perpendicular to the flow direction. The cylinder oscillates under VIV and galloping in transverse direction of the flow.

Figure 1.3. VIVAVE converter Lab module in LTFSW Channel.

1.3.2. Virtual C-K system

To recall, the foundation idea to generate power using the VIVACE Converter was laid down by Bernitsas and Raghavan (Bernitsas et al. 2006, 2007,2008) and the system initially built by them basically comprised of a spring-damping-cylinder system. Due to hardware limitations, harnessed power is optimized only in a limited range of spring stiffness and damping ratio. In an attempt to fill this lacuna, a virtual damper/spring (V_{CK}) system was developed in the MRELab wherein the action of springs and damping forces are replaced with equivalent force produced by a motor. Lee (2010) has designed a virtual damper/spring system (V_{ck}), the V_{ck} VIVACE model, which provides damper-spring force based on displacement and velocity feedback while the hydrodynamic force is exerted on the cylinder. The rotational motion of the motor is converted to a linear motion by the timing-belt, which encircles two pulleys. The cylinder and its support strut are connected to the timing-belt and oscillate along the shafts driven by the motor. Figure 2.3 shows a drawing of the V_{CK} VIVACE apparatus.

1.3.3. Passive Turbulence Control

Energy harnessing through the VIVACE Converter is enhanced mainly by utilizin straight roughness strips, which act as Passive Turbulence Controller (PTC). Three guiding principles underlying the function of Passive Turbulence Control (PTC) are:

a) Control vortex shedding to maintain the correlation length past the end of VIV. This is a little controversial as it is not certain whether the correlation length is a cause or an effect.
b) Jump through transition from laminar to turbulent flow in the boundary layer by surface roughness.
c) Fixing the flow separation point on circular cylinder surface and utilizing the possible negative hydrodynamic damping caused by the effect of angle of attack.

PTC is implemented by applying straight roughness strips with certain width and roughness height glued to the surface of the cylinder at various circumferential locations along the span of the test circular cylinder. The effects of roughness location, roughness

height, and coverage area are studied in Chapters 3, 4, 5 and 6, respectively, based on experimental measurements. Additionally, in a quest to understand the underlying flow physics, flow visualization tests are carried out and results are summarized in Chapter 11 for smooth cylinder and cylinder with PTC. All tests were conducted in the Low Turbulence Water Channel located in the Marine Renewable Energy Laboratory of the University of Michigan. The present study covers the range of Reynolds numbers of $10^4 < Re < 1.2x10^5$ (primarily the TrSL3 flow regime [Zdravkovich, 1997]).

CHAPTER 2

EXPERIMENTAL APPARATUS, SETUPS AND CALIBRATION

This chapter contains information on the experimental setup. This includes the facility, the VIVACE Converter model, passive turbulence control, instrumentation, visualization, the virtual device, and data analysis.

2.1. Facility

All model tests presented in this dissertation are conducted in the Low Turbulence Free Surface Water (LTFSW) channel of the Marine Hydrodynamics Laboratory (MHL) of the University of Michigan, Ann Arbor. The LTFSW Channel witnesses a continuous flow past a VIVACE cylinder, as indicated by Figure 2.1 below.

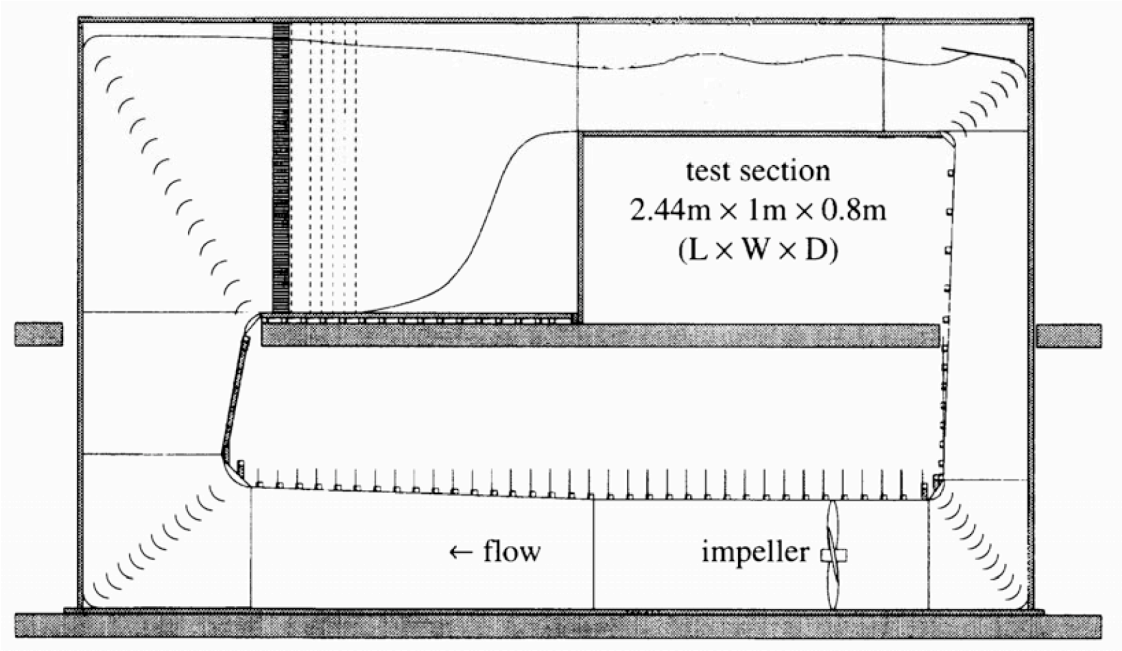

Figure 2.1. Low Turbulence Free Surface Water Channel

In the LTFSW channel, a re-circulating water flow is created past a circular cylinder. An alternative way to create current effect is by towing the cylinder at a constant speed in calm water. In those two cases, the relative flow past the cylinder is identical since the forward motion is independent of time. Raghavan (2007) claims that using either method, i.e., either LTFSW Channel or the towing tank, has benefits and limitations. Carefully maneuvering the towing tank with sufficient time between runs reduces the free-stream turbulence to negligible levels. However, the length of the towing tank presents a limit to the number of cylinder oscillations that could be monitored per run of experiment. On the other hand, the LTFSW Channel has no such limitations, because the water flow is generated by a rotating impeller. However, it is difficult to achieve low turbulence levels in the LTFSW because it is inevitable to produce turbulence due to the presence of the VIVACE Converter in VIV or galloping.

After evaluating the costs and benefits of using each method, the LTFSW Channel was chosen for the present study because of the advantages listed above. In addition, the free stream turbulence level is low and acceptable (Walker et al 1996). The primary reason to use the LTFSW Channel is to study the fundamental aspects of turbulent flows. In this dissertation, experiments were carried out in the LTFSW Channel to primarily evaluate the power harnessed from the flow-induced motions of a surface modified circular cylinder apart from the cylinder dynamics thereof. The water channel is two-story high and it recirculates approximately 8,000 gallons of softened and filtered water. Recirculation of water flow through the channel is made possible by a four bladed bronze impeller with a diameter of 0.787m and is powered by a 20 hp three-phase induction motor. This channel has maximum flow speed of 2m/s with a test section 2.44m long, 1m across and 0.8m deep. The sidewalls of the test-section are made up of transparent, acrylic to enable flow visualization experiments also aiding to record measurements with optical instrumentation. Furthermore, Walker et al. (1996) reports the turbulence intensity normalized by the free-stream velocity as 0.095%.

Velocity surveys are conducted to measure the velocity of the flow at different water depths of the LTFSW Channel, by using a Pitot tube. An array of Pitot tubes is positioned at 30cm above the bottom and at half-width of the tank. A factor for various water depths

is found out, which when multiplied by the frequency of the impeller gives the flow velocity. Using the Pitot tube and determining water depths, the velocity profiles are measured at one downstream location yet at four other frequency settings on the drive motor at six different depths. From these profiles, the relationship between the impeller frequency and the free-stream velocity can thus be found out as shown by the following equation:

$$U\ (m/s) = (-0.000034 \times (\text{Depth (mm)}) + 0.061177) \times \text{Impeller Frequency} \quad (2.1)$$

The correlation coefficient for this linear equation between free-stream velocity and the water depth is R^2=0.994211. As Raghavan (2007) suggests, these values match well with the average value measured used in K. Maki's Ph.D thesis (Maki, 2005).

2.2. VIVACE converter – laboratory model

A simple schematic of single module of the VIVACE Converter considered in this thesis as depicted in Figure 2.2. The elements of this module are: a rigid circular cylinder of diameter D and length L, two supporting linear springs each of stiffness $K_{spring}/2$, damping of transmission mechanism c_{system}. The cylinder is placed with its axis in the z-direction, perpendicular to the flow velocity U, which is in the x-direction. The cylinder oscillates in the y-direction, which is perpendicular to its axis in z and the flow velocity in x.

This module is used to study the effect of Passive Turbulence Control (PTC) location, roughness height, and area coverage on the induced oscillations of the cylinder. This module is designed as a low damping system with a fixed mass ratio, m*. It was later improved to accommodate additional damping to study the effect of PTC on VIVACE performance in high damping conditions.

To study the energy generation aspect of VIVACE, a V_{ck} system was introduced to the first VIVACE module. The motor was used to generate virtual spring torque and damping torque measuring the angle and angular velocity while the hydrodynamic force is exerted on the cylinder. The rotational motion of the motor is converted to a linear motion by a timing-belt, which encircles two pulleys. The moving part, consisting of the cyl-

inder with its support strut, is connected to the timing-belt and oscillates along the shafts driven by the motor. Lee (2010) has developed a method of system calibration to find out the nonlinear damping induced in the V_{ck} VIVACE. Commercially available Lab-View software is used to program the controller and simulate the motor torque as spring and damping force. A simple schematic of the V_{CK} module of the VIVACE is shown in Figure 2.3.

Some of the properties of VIVACE lab module and V_{CK} VIVACE module are listed in Table 1 and 2, respectively.

TABLE 1. SYSTEM PROPERTIES OF VIVACE LAB MODULE

Operating system	Real damping spring VIVACE converter
D: diameter of cylinder (m)	0.0889 (3.5" cylinder)
L: length of cylinder (m)	0.9144
Aspect ratio	10.29
m_{osc}: mass of oscillation (kg)	9.78
m_d: displaced mass (kg)	5.67
m*: mass ratio	1.72
K: stiffness (N/m)	775 and 826
$f_{n,water}$: natural frequency in calm water (Hz)	1.12 (K=775N/m); 1.16 (K=826N/m)
C_{system}: structural damping coefficient (Ns/m)	3
Z_{system}: structural damping ratio	0.017 (K=775N/m); 0.016 (K=826N/m)

TABLE 2. SYSTEM PROPERTIES OF V_{CK} VIVACE LAB MODULE

Operating system	Virtual damping spring VIVACE converter
D: diameter of cylinder (m)	0.0889 (3.5" cylinder)
L: length of cylinder (m)	0.9144
Aspect ratio	10.29
m_{osc}: total mass of oscillation (kg)	10.75
m_{eff}: effective mass (kg)	2.05
m_d: displaced mass (kg)	5.67
m*: mass ratio	1.88
K: stiffness (N/m)	400 to 2000
$f_{n,water}$: natural frequency in calm water (Hz)	0.78 to 1.76
C_{system}: structural damping (Ns/m)	3.2
ζ_{harn}: extra damping ratio for energy harnessing (Ns/m)	0, 0.04, 0.08, 0.12 and 0.16

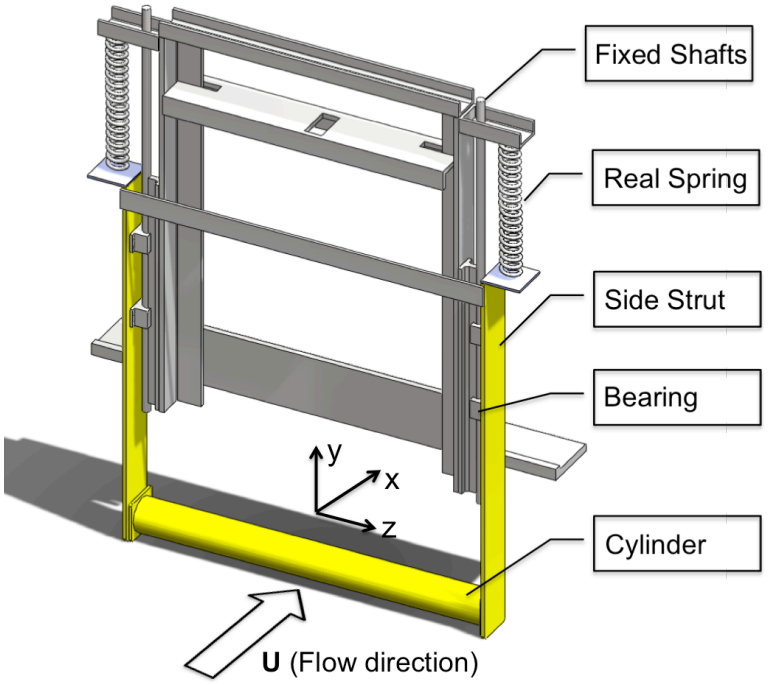

Figure 2.2. Simple schematic of VIVACE converter (real spring system)

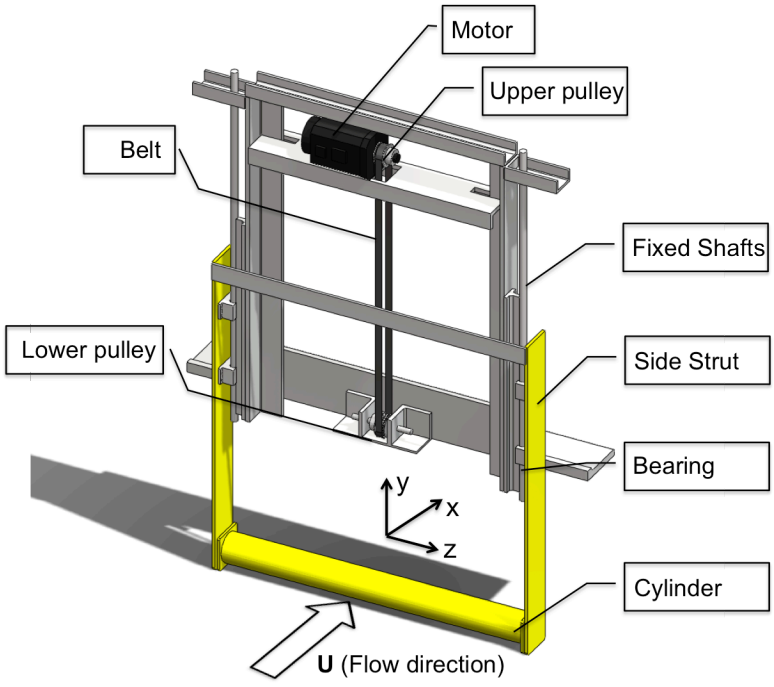

Figure 2.3. Simple schematic of V_{ck} VIVACE converter

2.3. Passive Turbulence Control

Different strips with roughness designations P60, P80, P120 and P150 have been used as Passive Turbulence Controllers (PTC) for the research in this dissertation; higher 'P' value indicates smoother surface strip. The total thickness (T) of PTC strips is defined as T=k+P, where k is the roughness height and p is the paper thickness. Physical dimension of surface roughness used in this dissertation are listed in Table 5 in Chapter 4. Waterproof sandpaper strip is cut into specific width for testing. A thin double-sided tape is applied as adhesive medium between of PTC and cylinder surface. The thickness of double-sided tape is 95 micrometer per layer. The PTC location is referred to as "placement angle" (α_{PTC}) throughout the text of this dissertation, which is the circumferential location of the upstream edge of PTC (the edge closer to the front stagnation point) on the cylinder surface. All properties for describing PTC used in the experiments are shown in Figure 2.5.

For all the tests conducted, a circular cylinder of diameter D=3.5inch with an aspect ratio of 10.29 was use Figure 2.5 shows the schematic sketch of cylinder with roughness strip.

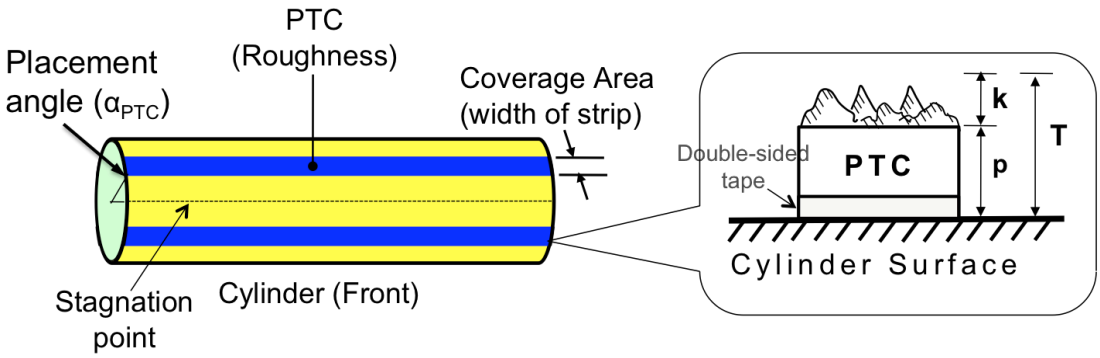

Figure 2.4. Configuration of roughness strip (PTC) around the cylinder

2.4. Flow visualization

Flow visualization of the near wake of the oscillating circular cylinder is conducted to facilitate understanding the near-wake flow features and how they relate to the cylinder vibrations (VIV or galloping) under various flow conditions, stiffness, damping, and

geometrical configurations with roughness strips. Visualization of flow is made possible by mixing appropriate amount of aluminum oxide particle of 100microns and fluorescent particles in the 8,000 gallons of re-circulating water. These particles are at first placed in a container of suitable size specially made for this purpose and mixed thoroughly with water.

To seed aluminum oxide particles into the flow, a dispenser tube (small, perforated circular rod, 6mm in diameter) is added at the base of the container. A series of small perforations are made in the rod so that the aluminum oxide mix flows into the water steadily, as issuing jets, thus enabling uniform powder deployment in the water covering well the cylinder cross section where the laser sheet is formed. Thus, the flow over the cylinder can be clearly visualized. Actual visualization was made possible by creating a laser sheet perpendicular to the cylinder axis. Instead of using a dispenser tube, a syringe needle with 0.45mm-diameter opening is placed one meter upstream of the cylinder in a streamline shape (see Figure 2.6) to seed fluorescent particles into the flow.

Figure 2.5 shows a block diagram of the laser arrangement for flow visualization. The laser beam emitted from an Argon Laser Unit (Continuous Type; Make: Coherent Inc, USA; Maximum Power 5W) is transmitted through a system of lenses and reflectors to obtain a uniformly distributed laser light sheet to illuminate the test section. Depending on the flow speed, adjustments are made in the laser power to optimize the light intensity in the test area. Poor or too bright laser illumination result in improper visualization of the flow field.

Flow visualization images are recorded by Kodak® High resolution digital low noise camera with 1048x1048 pixels resolution equipped with a 12mm focal length, wide range lens. Physical area framed during the experiment is about 500mm (Wide) x 600mm (long). The digital camera is mounted on a height and angle adjustable tripod and placed 1.8m away from the center of the cylinder. Maximum recording rate is 32 frames/second. Examples of flow visualization results are shown in Figure 2.7 and Figure 2.8.

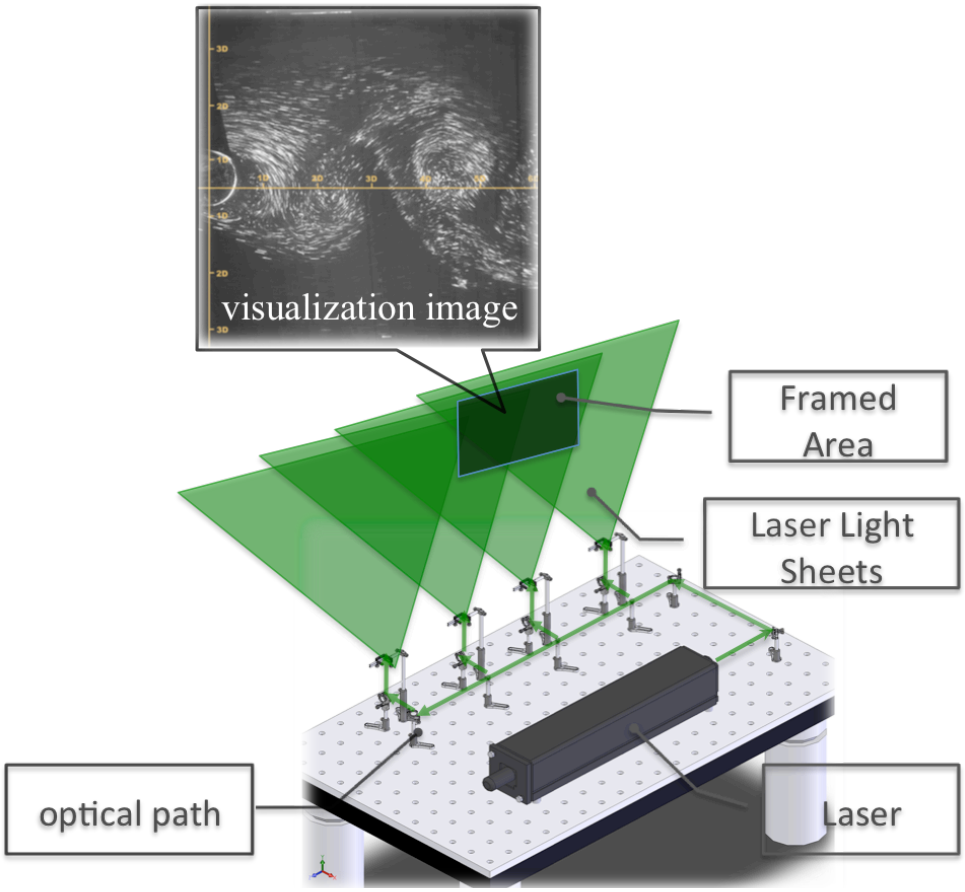

Figure 2.5. Simple schematic of lab flow visualization

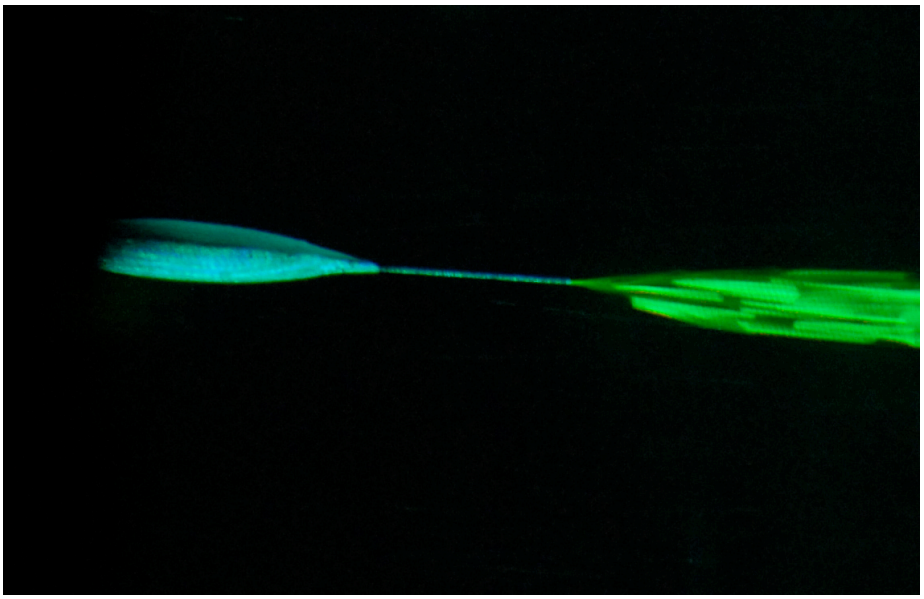

Figure 2.6. Fluorescent particles seeding device.

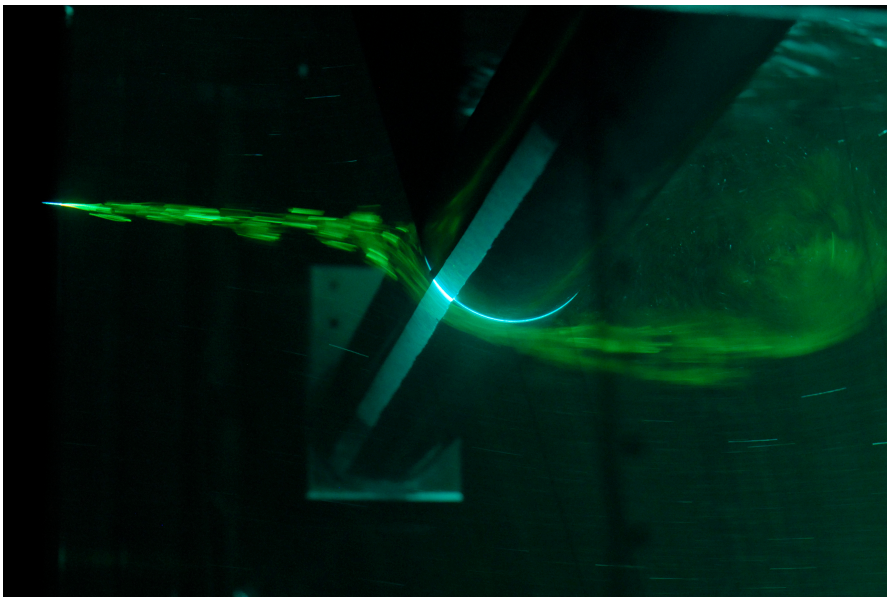

Figure 2.7. Photograph of flow visualization using fluorescent particles.

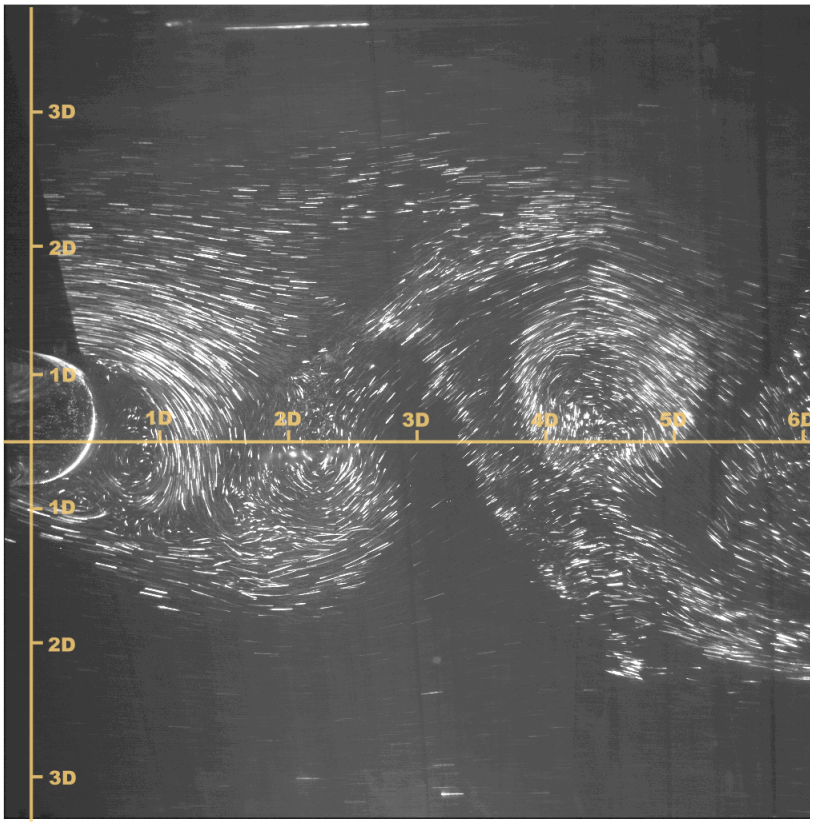

Figure 2.8. Example of flow visualization (aluminum oxide particles)

2.5. Damping identification

Since the motion of cylinder is constrained by linear bearings to oscillate freely in the y-direction (transverse to the flow), friction force is generated when the bearing slides on shaft. Structural damping could be changed because of the design (number of bearings), fabrication and mounting of the VIVACE. Therefore, the damping model is very sensitive to any possible changes in the model. In the experiments presented in this dissertation, damping identification tests are conducted whenever any modifications were made on the VIVACE converter models.

The damping of the system is assumed to be a linear viscous damping and is proportional to velocity of motion. Damping ratio can be found by measuring free oscillation response after giving an initial displacement of the cylinder (free decay test). A Matlab code is used to simulate the recorded free-oscillation decay curve to estimate damping ratio. Three free-decay tests were carried out for each given initial displacement. The average value from all tests is used as the system damping.

2.6. Data measurement

The cylinder oscillatory displacements are measured using a Celesco cable extension position transducer (yo-yo potentiometer). The voltage measurement was done by directly connecting the generator to the data acquisition system. The latter consists of a 16-bit analog to digital converter with four-pole, low-pass, Butterworth filters collecting all the data at a 100Hz-sampling rate. All the data for large amplitude oscillations were recorded for a time interval of 60s. In V_{ck} VIVACE, oscillatory displacements and velocities are measured by an encoder built in the motor at a scanning frequency of 100Hz.

CHAPTER 3

EFFECT OF PASSIVE TURBULENCE CONTROL LOCATION ON VIVACE

3.1. Background

In order to create roughness strips generating passive truculence control (PTC), a pair of symmetrically-located, one-inch wide strips are pasted on the surface of the cylinder with their upstream edge located at α_{PTC}=20°, 30°, 40°, 50°, 64°, covering circumferential surface area equivalent to 16° for each strip (one inch wide PTC strip). Smooth cylinder response, is also plotted in the same figures presented in this chapter, providing a basis for assessing roughness effects. To establish a valid comparison set of data, prior to analyzing effects of strip location on rough cylinders, smooth cylinder response is first discussed and compared with results in the open literature. Reynolds number effect on VIV is considered. This chapter concludes with a discussion on critical PTC locations for galloping. In Figure 3.1, typical oscillatory amplitude (shown by black lines) and frequency (shown by blue lines) plots are shown with respect to Reynolds number (x-axis). Zones corresponding to VIV, VIV-Galloping transition and "Fully Developed Galloping" are clearly marked on the figures.

In connection with the results of the present study on the oscillatory features of rough cylinders (with PTC), the following points need be noted (see Figure 3.1):

a) VIV is characterized by an initial branch and an upper branch. The lower branch is noted only for smooth cylinder response. For cylinders with PTC, this response branch is absent. The possible reduced velocity range for lower branch is taken over by galloping oscillations.
b) Galloping instability is assumed to be initiated at the reduced velocity ($U^*_{galloping}$) at which the oscillation frequency drops or stops to increase further. At this critical re-

duced velocity, negative hydrodynamic damping is thought to begin acting on the system. It is particularly important that; the initiation of galloping cannot be identified by amplitude trend alone since, just at the point of inception, an abrupt jump in amplitude does not occur. Here, the frequency trend aims to mark the onset of galloping.

c) Galloping instability being initiated at $U^*_{galloping}$, is only manifested fully over a range of reduced velocity (indicated as 'galloping transition' zone in Figure 3.1). In this range, the hydrodynamic damping becomes progressively negative until a reduced velocity is reached at the point, which the amplitude up-shoot occurs. The point of amplitude up-shoot is referred to as 'fully developed galloping'. Thus, for the occurrence and full manifestation of galloping, our present study suggests a range of possible reduced velocity unlike the results presented in other studies claiming that a single value of reduced velocity is the only way to produce a fully developed galloping.

d) Further details of galloping instability are worked out in Chapter.10.

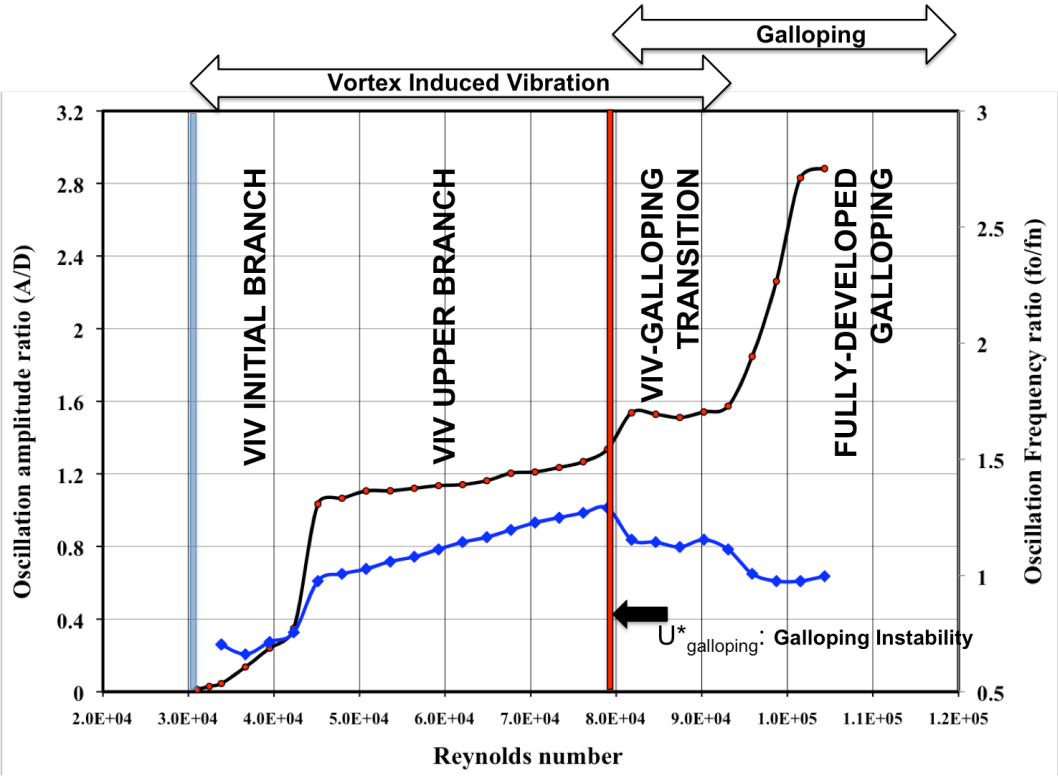

Figure 3.1. Response zone nomenclature for cylinder with PTC

3.2. Smooth cylinder response

The vibratory response of a smooth circular cylinder is first studied in this section. The amplitude response of a smooth cylinder is given in Figure 3.2. The typical VIV response consists of an initial branch ($4.0 \leq U^* \leq 5.5$) followed by an upper branch ($5.5 \leq U^* \leq 9.8$) and a lower branch ($10.7 \leq U^* \leq 12.2$), ending in de-synchronization ($U^* > 12.2$). This result complies with the observations in previous studies for cylinder response at low mass ratios (Khalak and Williamson, 1996; 1997; 1999). Despite of the fact that the general trend looks similar, the profile of VIV response in this study is different from what has been reported in previous open literature. For instance, in the upper branch for present study, the amplitude variation with respect to reduced velocity is nearly linear, contrary to the curve-linear profile reported by Khalak and Williamson (1999) and Govardhan and Williamson (2000). Further, the upper branch in this VIV response is much broader occupying most of the VIV synchronization range. In fact, as Bernitsas at al. (2008) show for Reynolds number in the TrSL3 regime, the upper branch fully overtakes the lower branch in the VIV response. In addition to the different profiles of upper branch, as Figure 3.2 shows, the lower branch amplitude decreases steadily in this VIV response in contrast to the nearly flat and broader profile observed by Khalak and Williamson (1999) and the precipitous drop with no lower branch observed by Bernitsas et al. (2008). In addition, unlike previous studies, a small 'kink' is observed at the beginning of the lower branch in this VIV response indicated at $U^*=11.0$.

As the present results show (Figure 3.2), the maximum amplitude of oscillation ratio, A^*_{max}, is about 1.65 occurring in the upper branch; $A^*_{max} = A_{max}/D$ where A_{max} is the average of the top ten maximum amplitudes out of about 60 cycles of measurements per test. The frequency response is shown in Figure 3.3. In present study, the value of $A^*_{max}=1.65$ obtained for $m^*=1.725$, $\zeta=0.0233$, and at $Re=100{,}000$ which is significantly higher than the maximum amplitude value of 1.13 obtained by Vikestad (1998) for $m^*=1.714$, $\zeta=0.007$, and $Re=33{,}000$. At still higher Reynolds numbers reported by Bernitsas et al. (2009) and Ding at al. (2006), results show higher A_{max}/D response near 1.9-2.0.

As can be seen in Figure 3.3, the frequency ratio $f^*=f_{osc}/f_{n,water}$ of oscillatory fre-

quency (f_{osc}) to system natural frequency ($f_{n,w}$) in water increases with reduced velocity throughout the synchronization range for the smooth cylinder. For $U^* \cong 5.0$, f^* shows a jump to a higher value corresponding to the jump from the initial branch to the upper branch. However, the jump in present study is found to be less steep than what is observed by Govardhan and Williamson (2000). In the same figure, f^* can be seen departing from unity, reaching about 1.3 at $U^* \cong 11$, tallying with the observations of previous investigators (Moe and Wu, 1990; Khalak and Williamson, 1997). This deviation of f^* from unity is attributed to the expected influence of added mass as discussed by Bearman (1984).

The present smooth cylinder results exhibit similar characteristics (three branch response) as previous results at low mass ratios (m^*) despite of higher Reynolds numbers used in this thesis. This observation further confirms the response boundary map in Figure 3.4 by Govardhan and Williamson (2006) where results from this thesis have been added. In the present case, the lower branch starts at about $U_{start}^*=10.7$ and ends at about $U_{end}^*=12.20$ as opposed to the values of $U_{start}^*=8.72$ and $U_{end}^*=14.0$, calculated by using the equations suggested by Govardhan and Williamson (2000):

$$U_{start}^* = \sqrt{\frac{(m^* + C_a)}{(m^* - 0.54)}} \qquad and \quad U_{end}^* = \sqrt{\frac{(m^* + C_a)}{(m^* - 0.54)}} \tag{3.1}$$

Based on the results of our experiments and those by Lee and Bernitsas (2010), the response boundary map is depicted in Figure 3.4, where the additional data at higher Reynolds numbers shown in the map are tabulated in Table 3. The present study and Lee and Bernitsas (2010) confirm the early results by Bernitsas et al. (2006, 2009) that VIV strongly depends on Reynolds number.

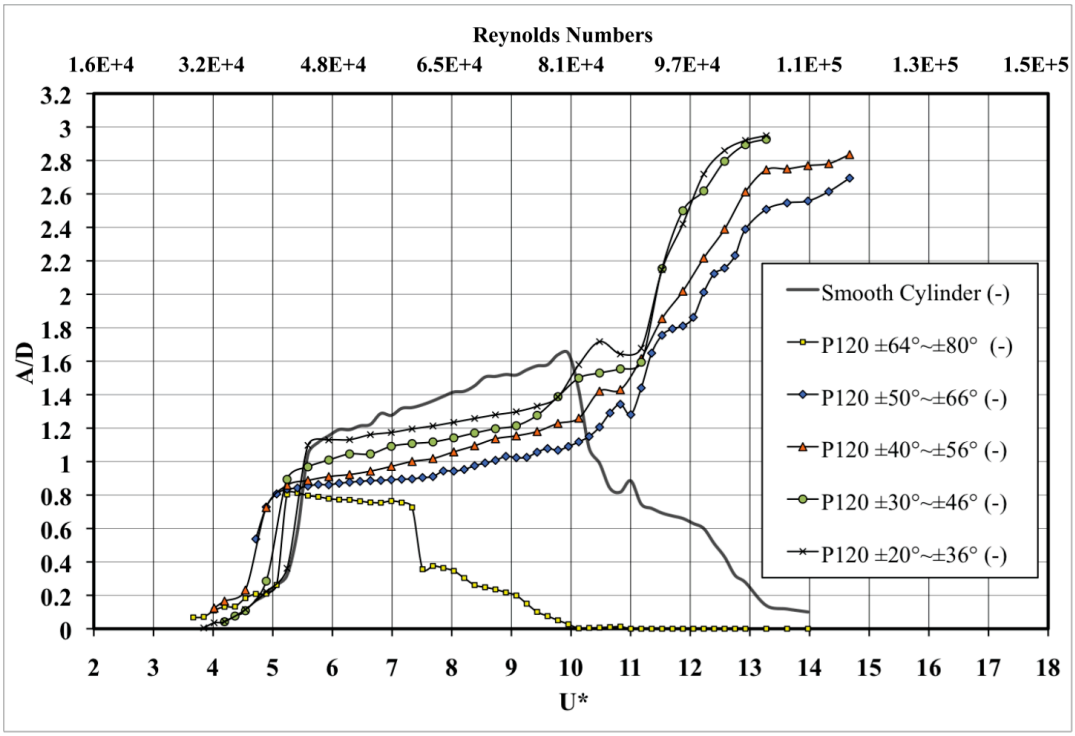

Figure 3.2. Cylinder amplitude vs. reduced velocity at different strip locations for P120 roughness.

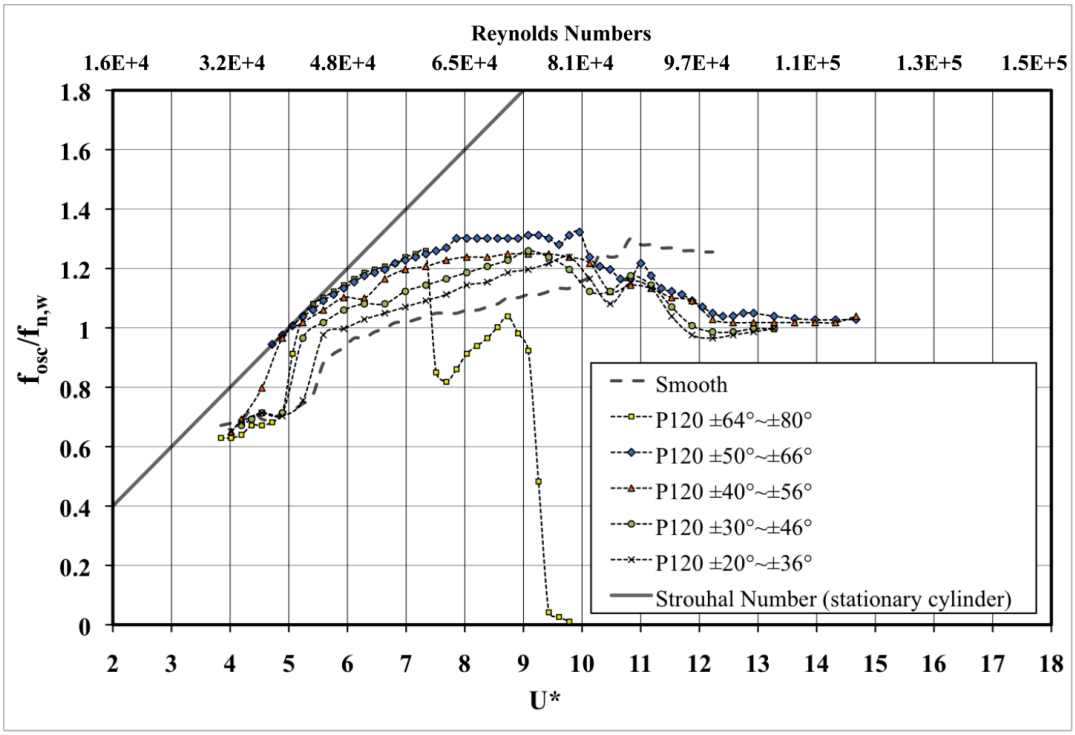

Figure 3.3. Frequency response versus reduced velocity at different strip locations.

TABLE 3. DATA FROM PRESENT STUDY AND LEE AND BERNITSAS, 2010

Re	U*	A*max	$f_{osc}/f_{n,w}$	α	m*	S_G	A^*_M	ζ
60645	7.91	0.95	0.973	0.554	1.9275	0.9041	0.7118	0.189
63533	8.29	1.09	1.018	0.4365	1.9275	0.713	0.8123	0.149
63533	8.29	0.95	1.0	0.554	1.9275	0.9041	0.708	0.189
66420	8.67	1.37	1.073	0.2023	1.9275	0.3304	1.016	0.069
69308	9.04	1.22	1.091	0.3194	1.9275	0.5216	0.9	0.109
75084	9.80	1.37	1.155	0.2023	1.9275	0.3304	1.0015	0.069
77972	10.17	1.53	1.164	0.0852	1.9275	0.14	1.114	0.029
80000 (present study)	9.80	1.65	1.30	0.064	1.725	0.997	1.21	0.0233
86635	10.11	1.73	1.122	0.0762	1.9275	0.124	1.244	0.026
89523	8.26	1.70	1.045	0.06	1.9275	0.098	1.22	0.021
89523	8.83	1.77	1.075	0.064	1.9275	0.105	1.27	0.022
89523.	9.54	1.78	1.096	0.0694	1.9275	0.113	1.276	0.024
92411	8.04	1.71	1.042	0.056	1.9275	0.0923	1.22	0.019

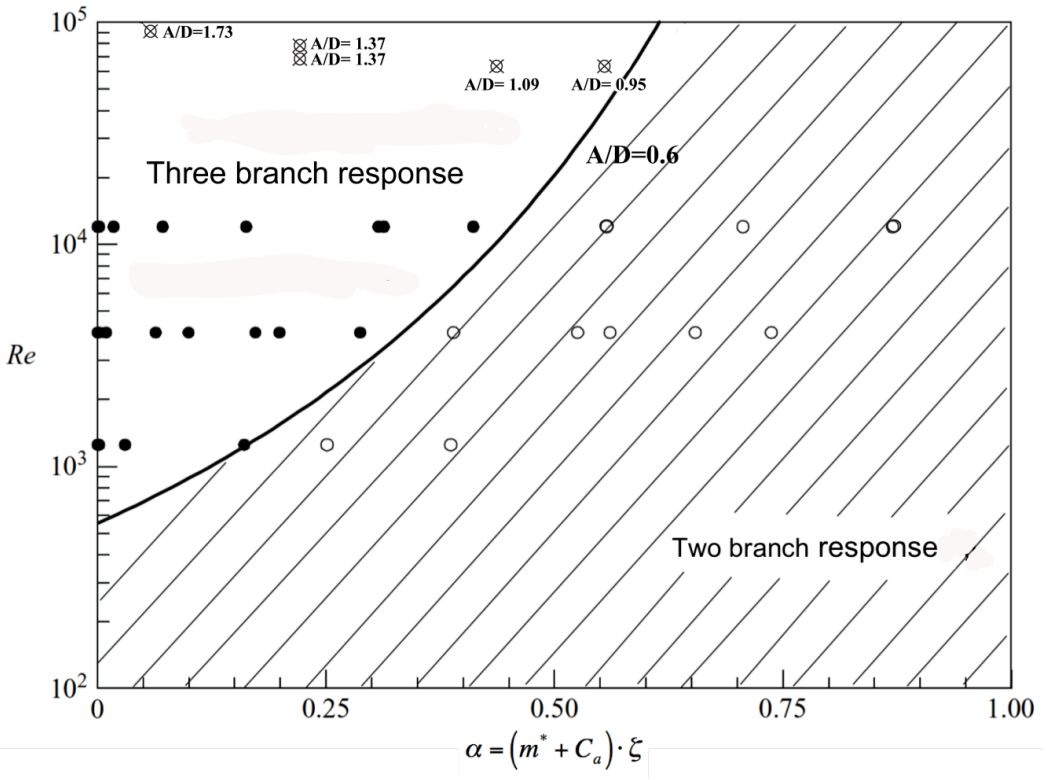

Figure 3.4. Response boundary map with data superimposed from Table 3

Data presented in Table 3 also shows the value of the Skop-Griffin parameter S_G, which can also be introduced into the Skop-Griffin graph of Figure 3.5 below. The peak amplitude predicted by the classical Griffin plot is about 1.1, which is much lower than the values in Table 3 which reach up to A^*_{max} = 1.78 for Re= 89,523. Other high values of A^*_{max} reaching up to 1.9, have been reported by Bernitsas et al. (2006b), Bernitsas et al (2009), and Raghavan and Bernitsas (2010). Deviations in A^*_{max} from the values in the Skop-Griffin plot have been observed by: (a) Hover et al. (1998) [$0.6 < A^*_{max} < 0.8$]; (b) Khalak and Williamson. (1999) [$0.55 < A^*_{max} < 1.20$] ; and (c) Govardhan and Williamson (2000) [$0.6 < A^*_{max} < 0.9$] .

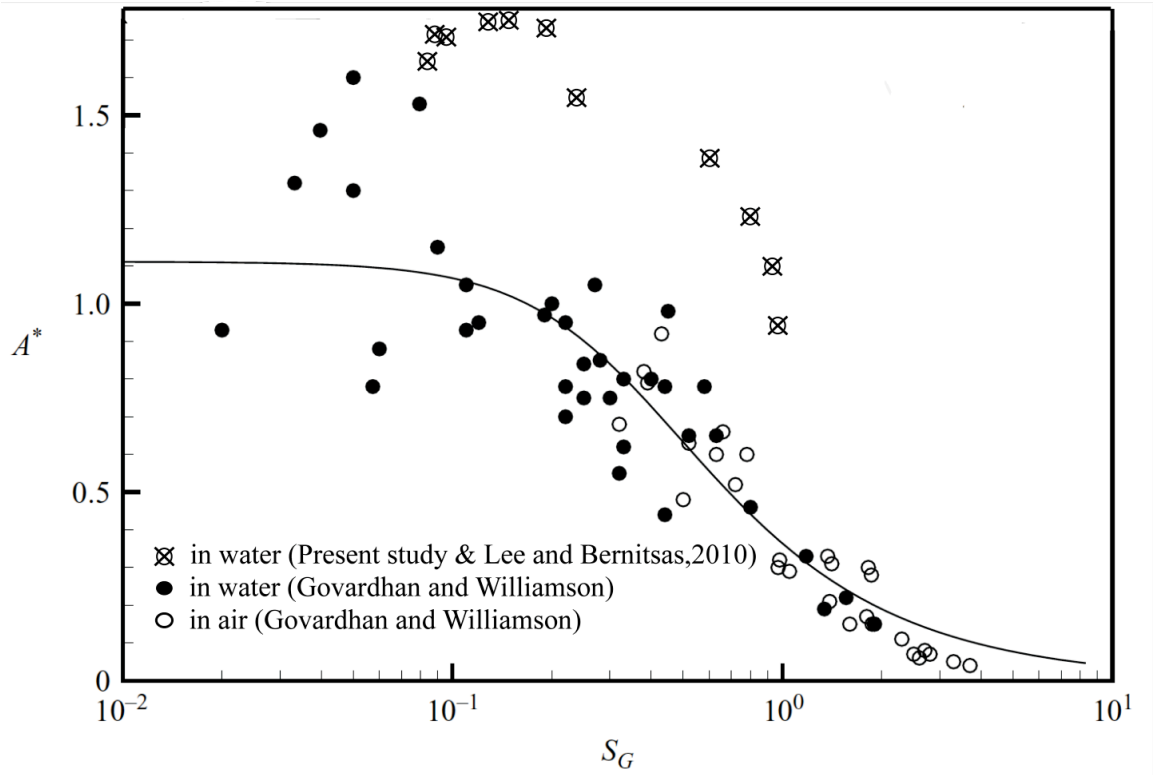

Figure 3.5. Skop-Griffin plot with the A* values from Table 1

Govardhan and Williamson (2006) defined A^*_M as to include Reynolds number to account for this scatter of data. By using experimental data and regression, they introduce a modified non-dimensional amplitude $A^*_M = A^*/\log_{10}(0.41\ Re^{0.36})$. The experimental data presented by Bernitsas et al. (2006b), and Raghavan and Bernitsas (2009, 2010) for A^*_{max} are higher than those extrapolated by the modified Skop-Griffin plot by a factor of two. It should be noted, though, that the formula derived by Govardhan and William-

son (2006) captures the trend of the dependence of A^*_M on α even for the high Reynolds number data of the present study.

In the present study at higher Reynolds numbers, even though the number of response branches in general agrees with the results predicted by Govardhan and Williamson (2006), the wake dynamics of the cylinder is found to be very different from what has been previously observed at low mass ratios. To elucidate this point, a qualitative flow visualization analysis illustrating this wake dynamics is presented later in Chapter 11.

3.3. Comparison of rough and smooth cylinder response

As presented in the previous section, Figure 3.2 shows the oscillating amplitude response of the 3.5" cylinder with different strip locations for the roughness strip P120. The smooth cylinder response is also given in the same figure for comparison. As can be seen in Figure 3.2, all the cases of roughness (except for P120 at 64°-80°) exhibit a response trend similar to that of the smooth cylinder up to a reduced velocity of about 10. For U* >10, for the smooth cylinder, the amplitude ratio A/D reduces precipitously indicating the end of synchronization, whereas for all the cases of rough cylinder A/D drastically increases. In the range of reduced velocity $5 < U^* < 10$, it should be noted that the amplitude of oscillation of rough cylinders is notably less than that of the smooth cylinder and for U* >10, the excitation level of rough cylinder (except the case with P120; 64-80) is significantly higher. For the roughness case of P120 at 64-80, a drastic reduction of both the maximum amplitude of vibration as well as shortening of synchronization range has been observed as seen in Figure 3.2.

From the response trends, it could be observed that the smooth cylinder exhibits a 'build-up drop-off" behavior suggesting the typical 'self-limiting' characteristic of Vortex-Induced Vibrations (VIV). The response clearly shows the existence of an initial branch ($4.0 \leq U^* \leq 5.5$), an upper branch ($5.5 \leq U^* \leq 10.0$) followed by desynchronization (U* >10.0) as mentioned in Section 3.2. Whereas, for the rough cylinder cases (except for the case of P120 at 64°-80°) up to $U^* \cong 10$, the trend reveals that the response could be due to VIV followed by a continuous build up of amplitude for U* >10,

indicating a galloping phenomenon. Thus, from Figure 3.2, it could be inferred that, roughness partially suppresses VIV amplitude until a reduced velocity of about 10 is reached. Thereafter, roughness promotes severe galloping oscillations (fully developed galloping) for the majority of the cases. Jubran et al. (1992) have made a similar observation on the effect of surface roughness on the flow-induced oscillations of a circular cylinder. Particularly, they have noticed that for U* < 12.5, roughness tends to reduce oscillation amplitudes and for U* > 12.5, roughness increases the oscillatory amplitudes. It should be noted that, even though this oscillatory feature is similar between results observed in present study and in Jubran et al. (1992), the Reynolds number range used in the latter is $6.0x10^3 \leq Re \leq 4.6x10^4$, which is significantly lower than that of the present research.

For the roughness case of P120 with strip location at 64°, the response trend does not exhibit any galloping even when higher reduced velocities (U* >10) are introduced. Instead, the oscillations could be assessed to be purely due to VIV similar to the smooth cylinder but with amplitude of oscillation significantly reduced and synchronization range severely shortened.

3.4. Critical PTC location for galloping

As previously discussed (Section 3.3), for strip location with α_{PTC} = 64°, the cylinder does not go into VIV-Galloping transition for U* > 7.5. Instead, oscillations are completely suppressed as shown in Figure 3.2. Interestingly, when the strip is placed very close to the front stagnation point (α_{PTC} =0°), the cylinder undergoes only vortex-induced vibrations and the vibrations die out for U* > 12.5 (Figure 3.6). The same figure shows that when the strip location is moved slightly farther downstream (α_{PTC} =10°), the cylinder undergoes galloping with inception of this phenomenon at about U*~9.8 further manifesting itself fully (i.e., fully-developed galloping) at U* ~ 11.0. These results reveal the range of critical PTC locations for the occurrence of galloping for higher reduced velocities of U* > 10. It could be inferred that, transition from VIV to galloping occurs in the reduced velocity range 9.8<U*<11.0 for the strip configuration P60 at 10deg-26deg. Figure 3.7 shows the corresponding frequency characteristics. For the case of VIV (0°-

16°), frequency ratio increases with reduced velocity as in all cases clearly indicating the absence of galloping. It exhibits, however, a small 'trough' at U* = 10.5 whereas, for the galloping case (α_{PTC} =10° to 26°), the frequency ratio decreases at U*~9.8.

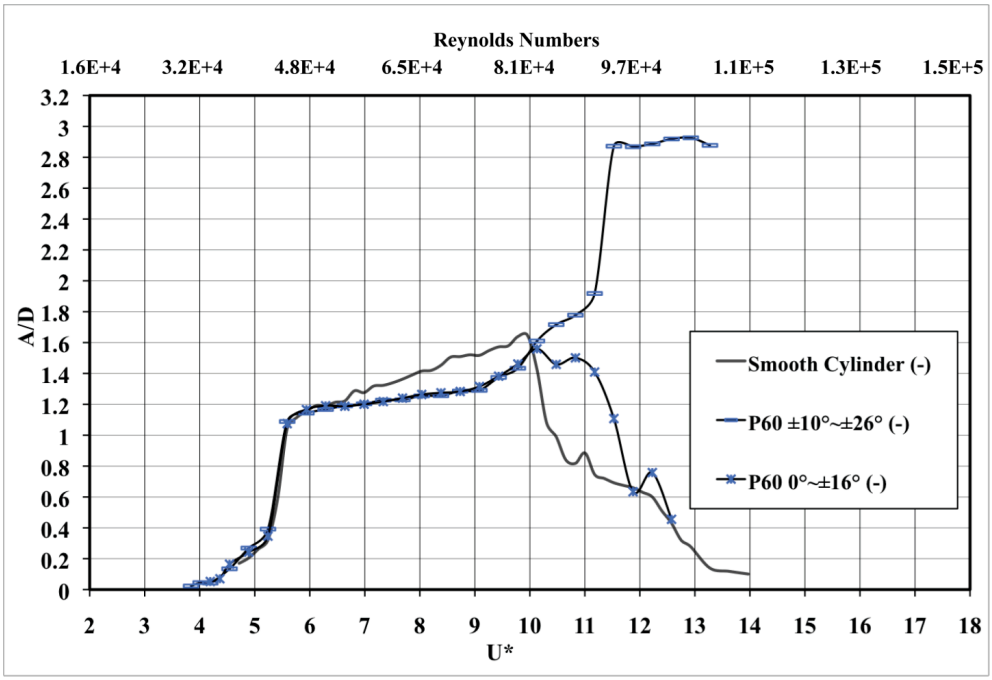

Figure 3.6. Amplitude plots showing critical strip locations for galloping.

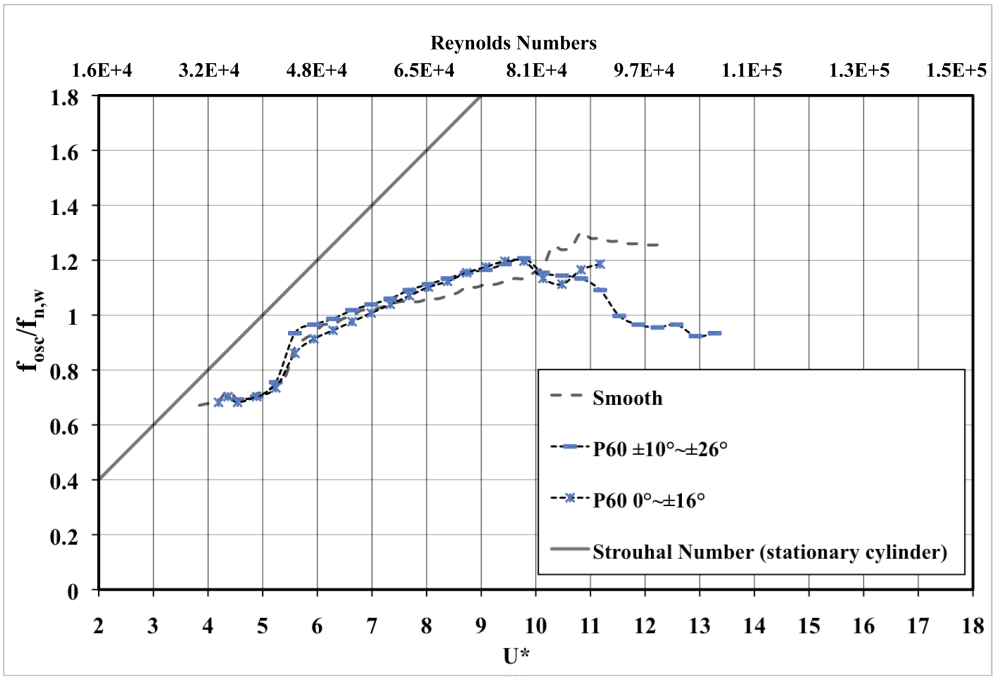

Figure 3.7. Frequency plots corresponding to Figure 3.6.

3.5. Conclusions

The following conclusions could be drawn from this section:

a) For rough cylinders, the VIV initial branch starts in lower reduced velocity compared to smooth cylinder.
b) In all rough cylinder cases, PTC partially suppresses VIV amplitude but promotes galloping.
c) The smaller the strip placement angle, the lesser the amplitude reduction in the VIV synchronization range.
d) The smaller the strip placement angle, the lower the oscillation frequency in the VIV synchronization range.
e) When the strip placement angle decreases, the oscillation frequency drops down at lower reduced velocity implying an early start of galloping instability.
f) The closer the strip to the front stagnation point, the steeper is the fully developed galloping branch.
g) A fully developed galloping is observed through a broad range of strip angles (10^o to 64^o).
h) A smaller strip placement angle marginally brings down oscillation frequency in the VIV-galloping transition zone.

CHAPTER 4

EFFECT OF PASSIVE TURBULENCE CONTROL ROUGHNESS ON VIVACE

4.1. Background

The effect of PTC roughness height is assessed in Chapter 4 after establishing its relation to the boundary layer thickness. Impact of roughness height on cylinder oscillatory characteristics is discussed in this chapter followed by a comparison between the smooth and rough cylinder (PTC) cases.

4.2. Roughness height versus boundary layer thickness

The boundary layer thickness (δ) of a steady, uniform flow passed a circular cylinder varies depending on the circumferential location as well as the Reynolds number. Following the approximate method of Pohlhausen (Schlichting, 1979), the boundary layer thickness is calculated under various strip placement angles (α_{PTC}) and Reynolds numbers as presented in Table 4. Then, the corresponding ratios between the total strip height k+P, where 'k' is the roughness height and 'P' is the paper thickness, and boundary layer thickness (δ) can be calculated for various cases. Table 5 shows the average height of roughness elements (k) for each of the roughness strips used and also the total thickness (T) of the strip including the paper thickness (p). The calculated values of boundary layer thickness at various Reynolds numbers and circumferential locations in conjunction with the strip dimensions are utilized to discuss the vibratory results in later sections of this chapter.

TABLE 4. BOUNDARY LAYER THICKNESS Δ(mm) FOR VARIOUS RE AND A FOR THE D= 8.9CM CYLINDER

Re → / α_{PTC} ↓	10,000	40,000	70,000	80,000	90,000	100,000	118,000
10	1.322	0.6608	0.4995	0.4672	0.4405	0.4179	0.3847
15	1.270	0.6348	0.4799	0.4489	0.4232	0.4015	0.3696
20	1.283	0.6416	0.48500	0.4537	0.4277	0.4058	0.3735
25	1.247	0.6234	0.4712	0.4408	0.4156	0.3943	0.3629
30	1.219	0.6092	0.4605	0.4308	0.4062	0.3853	0.3547
35	1.249	0.6246	0.4721	0.4417	0.4164	0.3950	0.3637
40	1.235	0.6175	0.4668	0.4366	0.4116	0.3905	0.3595
45	1.245	0.6248	0.4723	0.4418	0.4166	0.3952	0.3638
50	1.303	0.6516	0.4926	0.4608	0.4344	0.4121	0.3794
55	1.347	0.6736	0.5092	0.4763	0.4490	0.4260	0.3922
60	1.410	0.7050	0.5329	0.4986	0.4700	0.4459	0.4105
65	1.445	0.7225	0.5462	0.5109	0.4817	0.4569	0.4207
70	1.508	0.7541	0.5700	0.5332	0.5027	0.4769	0.4391
75	1.559	0.7796	0.5893	0.5512	0.5197	0.4930	0.4539
80	1.641	0.8207	0.6204	0.5803	0.5472	0.5191	0.4778

TABLE 5. PHYSICAL DIMENSIONS OF ROUGHNESS AND STRIP APPLIED ON CYLINDER

	P60	P80	P100	P120	P150	Strip I	Strip II	Strip III	Strip IV	Deouble-Side Tape
k: Averaged Grit size (10^{-6}m)	260	195	141	127	97	0	0	0	0	0
k_{max}: Max. Grit size (10^{-6}m)	416	302	213	175	150	0	0	0	0	0
k_{min}: Min. Grit size (10^{-6}m)	175	112	73	60	48	0	0	0	0	0
P: Thickness of sieve (10^{-6}m)	587	554	508	454	492	847	590	190	95	95
T: Total Thickness (10^{-6}m)	847	749	649	581	589	847	590	190	95	95
k/D (10^{-3})	4.68 ~1.97	1.26 ~3.4	0.81 ~2.4	0.67 ~1.97	0.54 ~1.69	0	0	0	0	0
T/D (10^{-3})	9.53	8.43	7.30	6.40	6.63	9.53	6.64	2.14	1.07	1.07

4.3. Impact of roughness height on the cylinder oscillatory characteristics

The effect of roughness height on cylinder vibratory response is shown in Figure 4.1 presenting a strip placement location at α_{PTC}=20° (PTC roughness: P150, P120, P80 and P60). In VIV regime, 5.5< U* < 9.8, the roughness height appears not to influence significantly the trend or the magnitude of cylinder vibrations. It is worth noting that the rougher the strip (lower P-value), the steeper the growth rate of fully-developed galloping oscillations commencing at U*>10.5. Fully-developed galloping is observed in lower reduced velocity with rougher strip, meaning with rougher PTC, a narrower VIV-galloping transition regime occurs. Such association suggests a significant impact of roughness height on the cylinder oscillatory characteristics under the galloping regime, $U^* \geq U^*_{galloping}$.

The maximum excitation amplitude of fully-developed galloping (U* ≅ 12 to 13) is not significantly affected by the roughness of the PTC as Figure 4.1 shows. It should be noted, however, that occasionally the oscillating cylinder was hitting the mechanical stopps located at A/D=3.0 to prevent possible damage of the flow channel by the cylinder. This is not considered as a major issue, because the A/D plotted is the average of the top 10 peaks of the entire recorded time series (60 seconds) for each test. It may further be noted that, when comparing to the smooth cylinder response, roughness partially suppresses VIV (in the synchronization range) though it promotes galloping at higher reduced velocities. Also, there is a slight shift in the VIV synchronization range towards lower U* values for the rough cylinder cases compared to the smooth cylinder response. Strikingly, the reduced velocity at which the amplitude fall-off (de-synchronization) occurs for smooth cylinder and onset of galloping for rough cylinder coincides at U*= 9.8.

As Figure 4.2 shows, the height of roughness elements does not significantly influence the response frequency neither in the VIV synchronization range (5.5 < U* < 9.8) nor in the fully-develop galloping excitation regime (U* ≥ 12). In all cases presented in this section (PTC at 20deg to 36deg), the frequency ratio increases up to about U* = 9.8 where the galloping instability starts and decreases thereafter. However, in all these cases, the frequency ratio for rough cylinders is considerably higher than that of the smooth cylinder case.

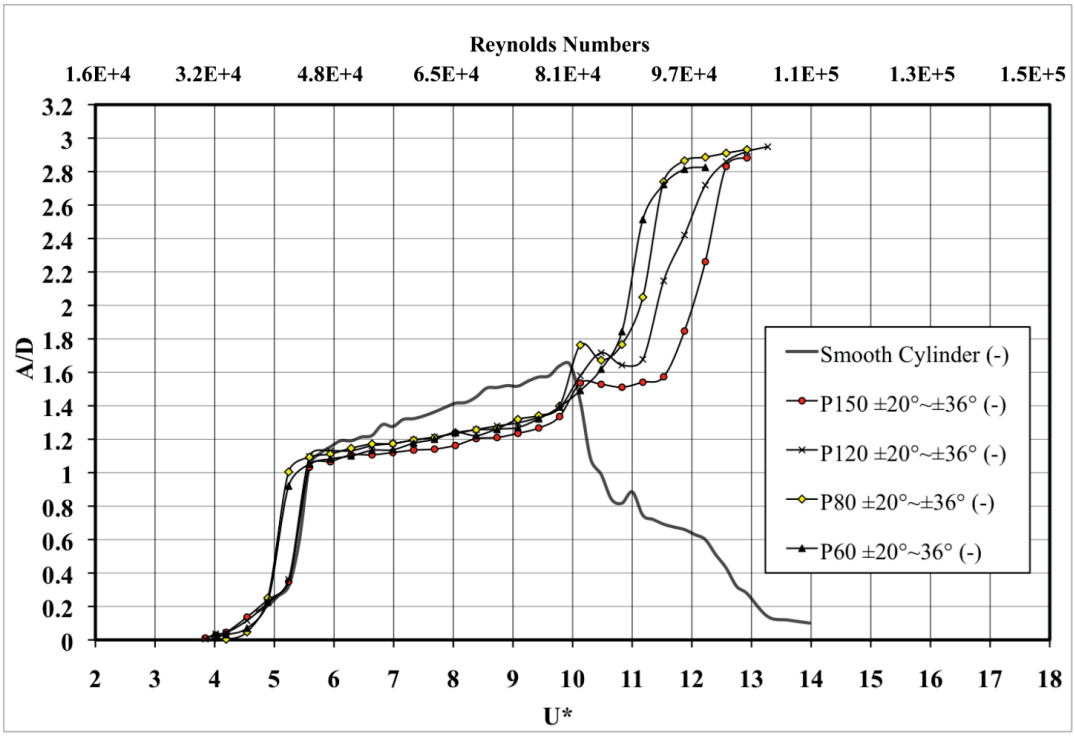

Figure 4.1. Cylinder response for different roughness heights; strip placement angle α_{PTC}=20°.

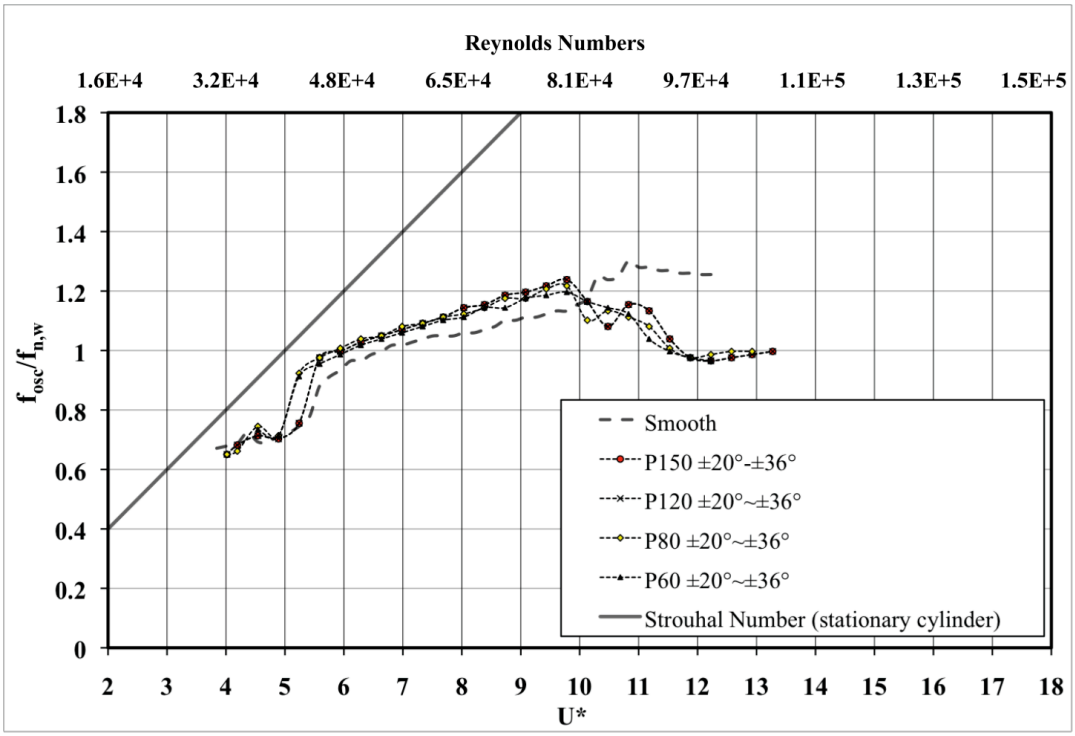

Figure 4.2. Response frequency versus reduced velocity for different roughness heights; strip placement angle α_{PTC}=20°.

4.4. Impact of smooth surface PTC on the cylinder oscillatory characteristics

This section deals with the influence of smooth PTC strips, i.e., strips without any roughness protrusion (k=0), on the oscillatory response of the cylinder. In the cases presented in this section, the PTC placement angle is 30deg from the front stagnation point with area coverage equivalent to 16deg. It should be emphasized that a higher damping VIVACE is used to conduct the experiments in this section. Vibratory amplitude responses are shown in Figure 4.3 and Figure 4.5 with smooth cylinder response so as to better highlight the effect of surface protrusion. Dimensions of strips I, II, III and IV are listed in Table 5 in Section 4.2.

There are two sets of tests corresponding to different study purposes in this section. The description of each set of tests is listed as below.

Test A: Study the effect of total thickness, T: From the results presented so far, it can be inferred that there are two main properties of PTC roughness influencing the vibratory response: (1) Roughness: To examine its effect a smooth PTC strip is used. (2) Total height: To study its effect a smooth surface PTC with varied thickness (0.095mm, 0.190mm, 0.587mm and 0.847mm) is used in this set of tests. Results are presented in Figure 4.3 and Figure 4.6.

Test B: Study the effect of roughness element k with fixed T rough and smooth strips: To better understand the effect of roughness element height k, a total height (T=0.875mm) of smooth strip is set equal to the total thickness of P60 and P150 PTC for testing.

Test C: Study the effect of roughness element (k) with fixed "p" rough and smooth strips: To better understand the effect of roughness element height (k), a total height (T=0.587mm) of smooth strip is set to equal to the "p" of P60 PTC (p=0.587mm) for testing.

Results of test B and C are presented in Figure 4.4, Figure 4.5, Figure 4.7 and Figure 4.8.

It is interesting to note that, for the thinnest strip used (T=0.095mm), no galloping

instability was observed and the cylinder undergoes only vortex excitation, similar to the response of the smooth cylinder (Figure 4.3). Whereas, for T≥0.19mm, cylinder is initiated to galloping instability at U*=9.4 ($Re \geq 7.7\times10^4$). The higher the T value, the steeper is the galloping branch with higher maximum amplitude of oscillation (A/D), which also commences at lower U*. In all cases (with strips), oscillatory amplitude is partially suppressed in the VIV synchronization range when compared to the smooth cylinder. These results also indicate that, a minimal surface protrusion is necessary to initiate galloping. Below certain value of T, hydro-dynamically, the cylinder behaves as a smooth cylinder even if a strip is introduced. Once T crosses a critical value, the geometry is sufficient enough to alter the system damping by generating negative hydrodynamic damping which causes galloping. However, the exact value of T at which this transition takes place cannot be fully investigated in this study, yet the research presents an initial start to search of the critical value. T/D (D = cylinder diameter) should lie between $1.069\text{x}10^{-3}$ and $2.14\text{x}10^{-3}$. It could also be seen that, with the introduction of strips, oscillations commence early compared to the smooth cylinder (Figure 4.3). The corresponding frequency features for these configurations are shown in Figure 4.6. In the initial branch, frequency values vary for different strips yet there is no systematic trend with respect to T. In the upper branch, the frequency values follow the same magnitude and trend irrespective of T. Meanwhile, in the post-VIV regime (galloping), oscillation frequencies do differ for different T values, where thinner strip contributes to higher frequency of oscillation also with greater fluctuations with respect to U*. For cylinder with the thinnest strip (minimum T), the oscillation frequency closely follows the smooth cylinder trend and magnitude as expected, except for a short range of U* (between 7.0 and 9.5).

Experimental results associated with PTC strips further indicate that roughness k is not necessary for the promotion of galloping instability. Meanwhile, as Figure 4.4 shows, when the total thickness T=k+P remains the same, a steeper fully-developed galloping branch and higher maximum amplitude is observed in the test with an introduction of roughness. In the same case, critical velocity for galloping ($U^*_{galloping}$) slightly shifts to higher flow speed as well. That is, roughness can act as a 'catalyst' to promote galloping fully-developed. Additionally, PTC roughness appears to initiate an early start of oscillations as shown by Figure 4.4. It is also interesting to note that the critical reduced velocity

to initiate galloping remains unchanged with the introduction of roughness. Such feature can be observed from the corresponding frequency responses shown in Figure 4.7. For $U^*<6.0$, oscillation frequency for rough cylinder is slightly higher over short range of U^*. For the range $5.5\leq U^*\leq 8.30$, roughness height k seems to affect the frequency of oscillation. Further, for $8.30<U^*<12.0$, the smooth strip case exhibits higher oscillation frequencies and for still higher U^* values, again, oscillation frequency is seen to be not affected by roughness.

Also, from the results of test B, Figure 4.5 provides more features of cylinder oscillation. When the total thickness (T) being the same, rougher PTC (larger k) leads to higher and steeper amplitude of oscillation but with a loss of amplitude in the VIV synchronization range. Also, the figure further depicts that, for the same paper thickness P, the increase in roughness k appears to be more significant. Roughness leads to substantial increase in the excitation amplitude as Figure 4.5 shows. Particularly, when comparing to rough cylinder cases, in the case of smooth strip (k=0), stepping up of excitation to the galloping branch is delayed. Further, it is found that, the introduction of higher roughness reduces the frequency of oscillation though the trend is not altered due to roughness (Figure 4.8). In all cases, frequency drops to lower values at about $U^*=9.4$. Furthermore, as seen in the previous cases, rough cylinder oscillation frequencies are higher than that of the smooth cylinder in the VIV synchronization range but comparatively lower, thereafter (Fig.1.8). Hence the total thickness T markedly influences the excitation of the cylinder. The effect of higher roughness at higher T is much more pronounced than that of higher roughness at T being constant. That is, as evidenced in Figure 4.3, the total thickness T is the major deciding factor with regard to the occurrence of fully-developed galloping. As pointed out earlier, roughness can act as a ‘catalyst’ to promote galloping fully-developed.

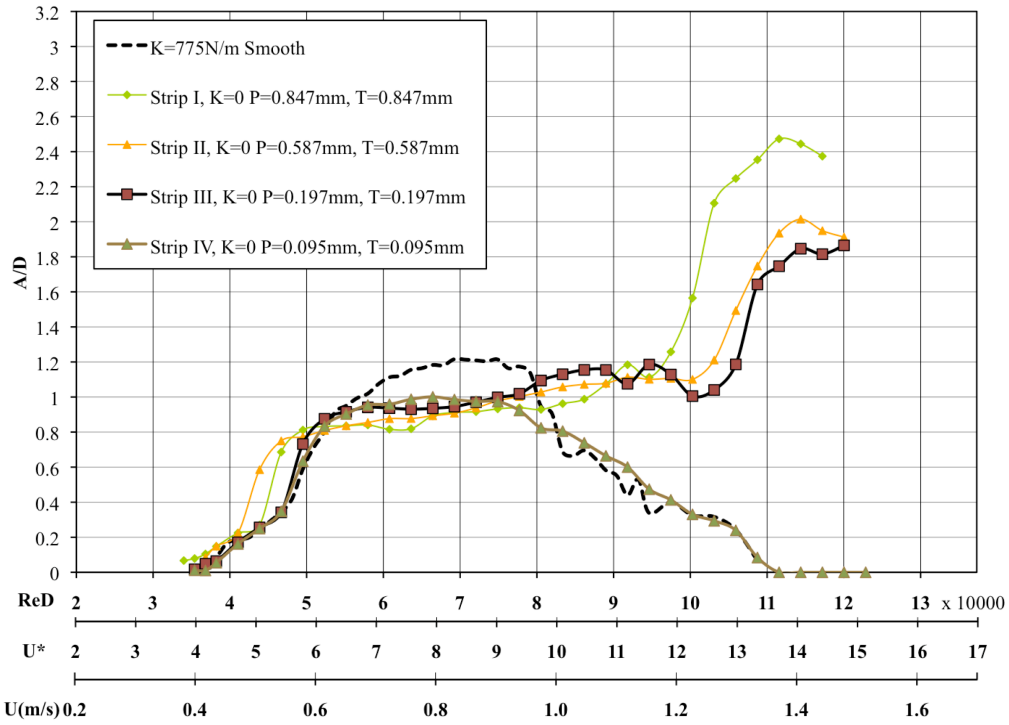

Figure 4.3. Response amplitudes for cylinder with smooth strips at 30deg

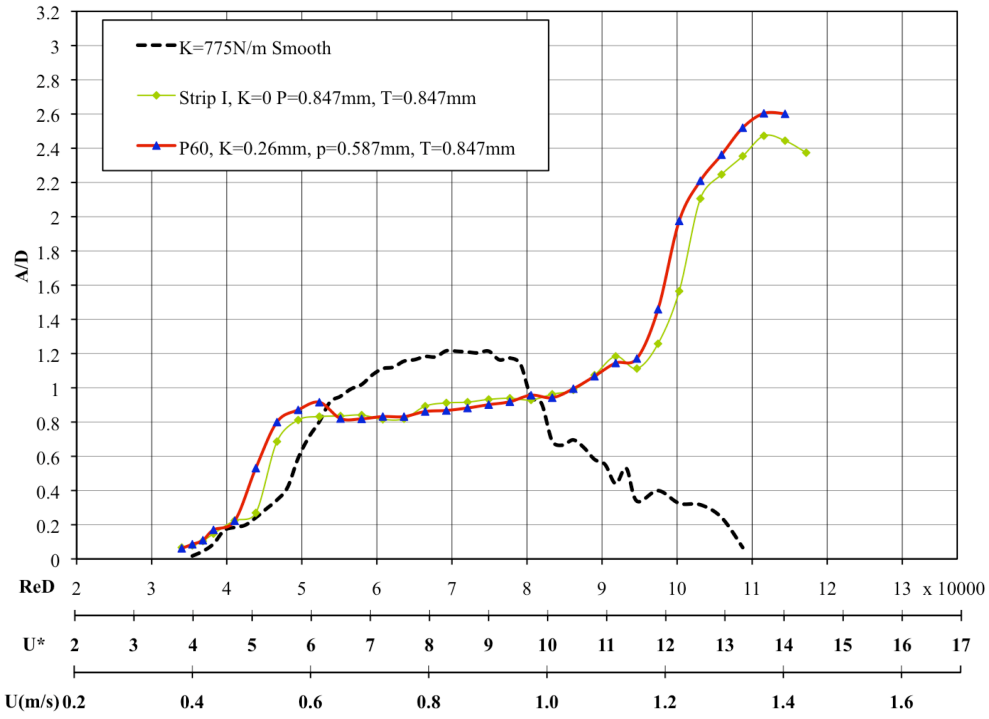

Figure 4.4. Oscillatory response of cylinder with smooth and rough strips with fixed value of T at 30deg.

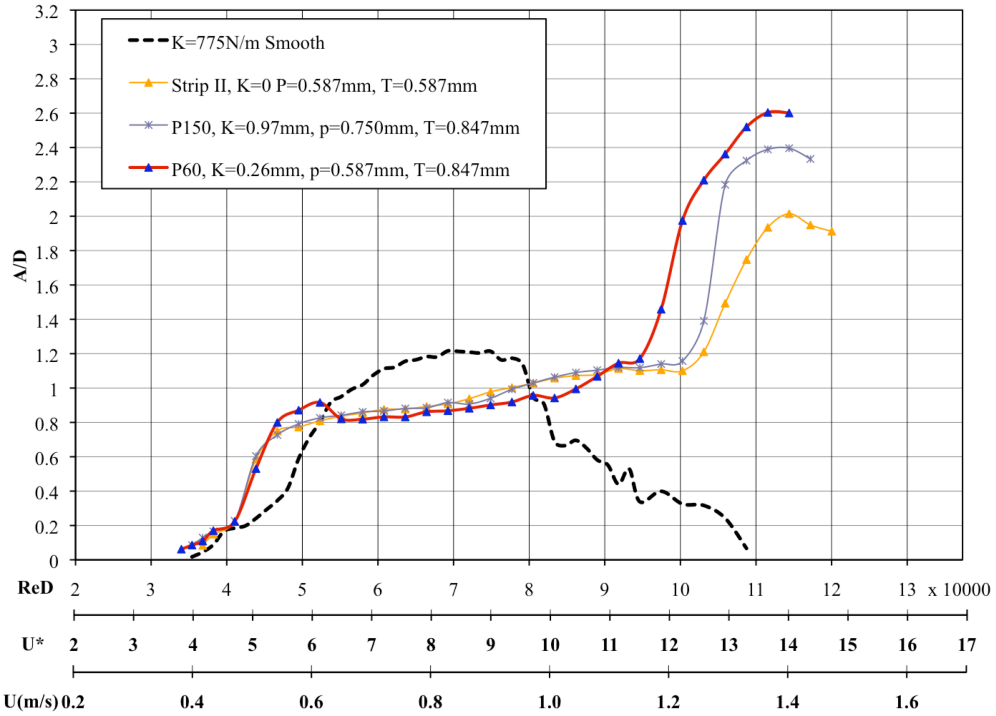

Figure 4.5. Cylinder oscillation with smooth and rough strips at 30deg.: a comparison

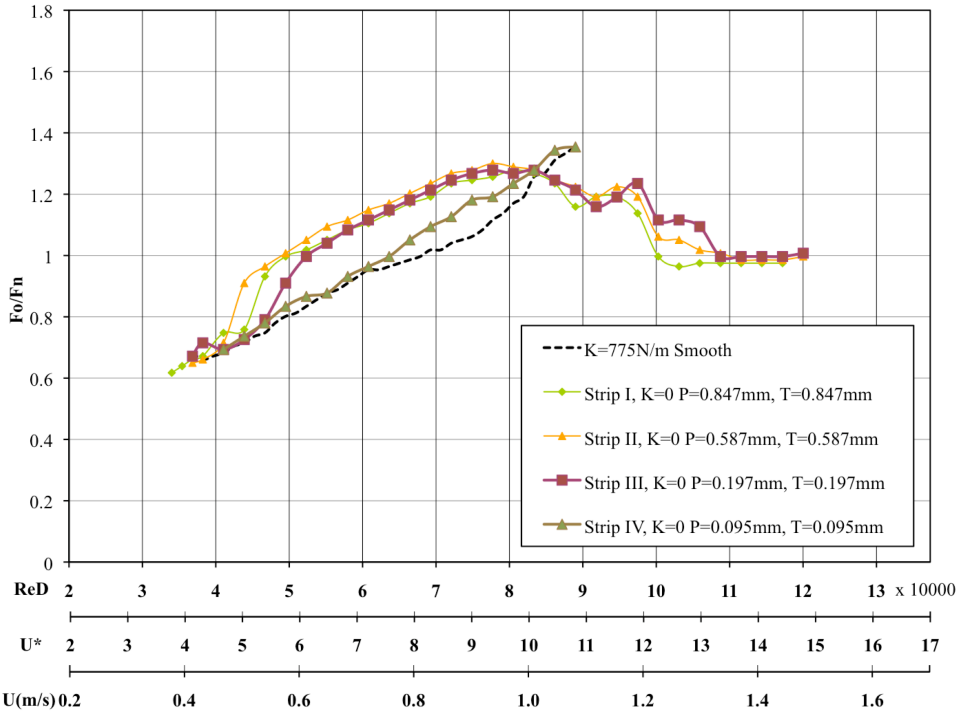

Figure 4.6. Frequency response for cylinder with different smooth strips at 30deg.

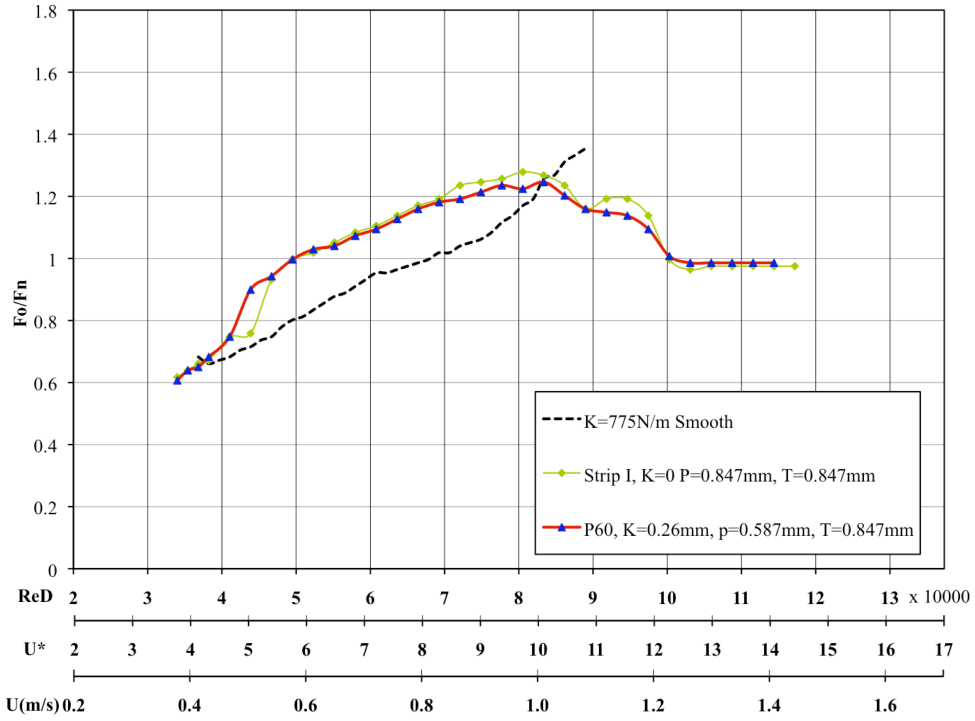

Figure 4.7. Frequency response for cylinder with smooth and rough strips with fixed value of T at 30deg.

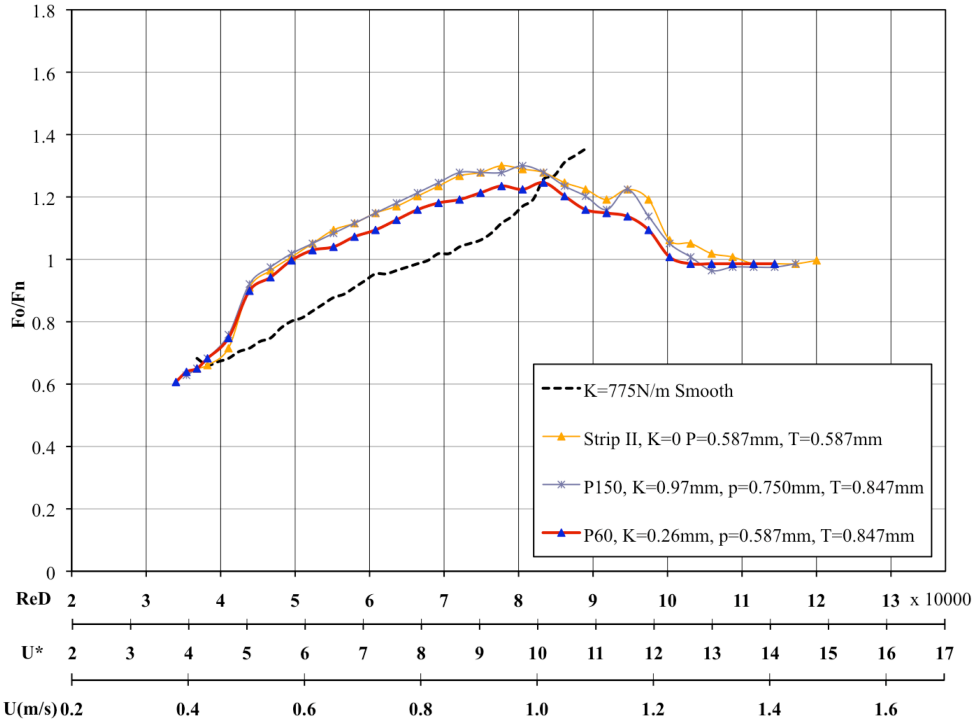

Figure 4.8. Frequency response of cylinder with smooth and rough strips: a comparison

4.5. Conclusions

The following conclusions can be drawn from this chapter:

a) Compared with smooth cylinder, the cylinder with PTC shows different oscillatory characteristics. The smooth cylinder exhibits an overall increasing-decreasing amplitude trend, which is typical of vortex-induced oscillations. Whereas, as the reduced velocity U* is increased, rough cylinder oscillations pass over from VIV to galloping at a particular U* value. This is particularly true for rough strips. For smooth strips (k=0), galloping was observed only if the strip thickness is greater than a specific value.

b) For a smooth cylinder, its response is characterized by an initial branch, an upper branch and a weak lower branch, which is finally followed by the de-synchronization branch. In the upper branch, amplitude appears to nearly follow a linear increase with respect to the reduced velocity.

c) At a particular strip location, a higher roughness (larger the roughness height) leads to an earlier amplitude pick up initiated in the galloping branch.

d) For smooth cylinders, the oscillation frequency shows an overall, continuous increase with respect to the reduced velocity. Whereas, for cylinders with rough strips, frequency of oscillation increases up to a particular U* value (VIV synchronization range) and then, drops-off for further increases in U* (indicating the starting of galloping).

e) The oscillation frequency values for both smooth and rough cylinders are, in general, less than the Strouhal frequency values throughout the entire tested range of U*. Roughness does not significantly alter the frequency characteristics except minor modifications.

f) Surface disturbance (smooth as well as rough strips), in general reduces the amplitude of oscillations in the VIV synchronization range while promotes galloping at higher reduced velocities.

g) Roughness is not necessary to initiate galloping instability as shown by the results with smooth strips. Yet when below a threshold value of total strip thickness, cylinder exhibits only VIV throughout the entire range of reduced velocity and not gallop-

ing.

h) For smooth strips, a higher thickness promotes earlier initiation of the galloping branch with higher maximum amplitude of oscillation.

i) For the same total thickness T (strip paper thickness plus roughness height), rough strips induce marginally higher amplitude than smooth strips.

j) As paper thickness p remains the same, rough strips contribute to considerably higher oscillatory amplitudes than smooth strips.

CHAPTER 5

EFFECT OF PSSIVE TURBULENCE CONTROL COVERAGE ON VIVACE

5.1. Background

In this chapter, the effects of passive turbulence control coverage are examined by conducting experiments in low damping with cylinder with PTC. The latter consists of roughness strips of varied width (1/4", 1/2", ¾" and 1"). The PTC placement angle (α_{PTC}) is fixed at 40deg. P120 sandpaper strips are used in the tests in this section.

5.2. Effect of roughness coverage

The effects of area coverage are illustrated in Figure 5.1 and Figure 5.2 for the rough cylinder cases with strips P120 attached. For all of these cases, the upstream tip of the roughness strip is placed at α_{PTC}=40deg. As can be seen in Figure 5.1, when the strip area coverage increases from 8 degrees (1/4 inch width of each strip) to 32 degrees (1 inch width per strip), the vibrations are increasingly suppressed in the VIV synchronization range. But, for U*>11, as the area coverage increases from 8deg to 24deg per strip, the growth rate of galloping oscillations increases and becomes steeper. As area coverage further increases to 32 degrees, the slope of galloping branch decreases (to an intermediate value). Also, for the case with area coverage of 32°, the Vortex-Induced Vibrations are clearly demarcated and separated from galloping oscillations as Figure 5.1 shows. In summary, as can be observed in all these roughness cylinder cases, there is a significant amplitude suppression in the VIV synchronization range compared to the smooth cylinder case.

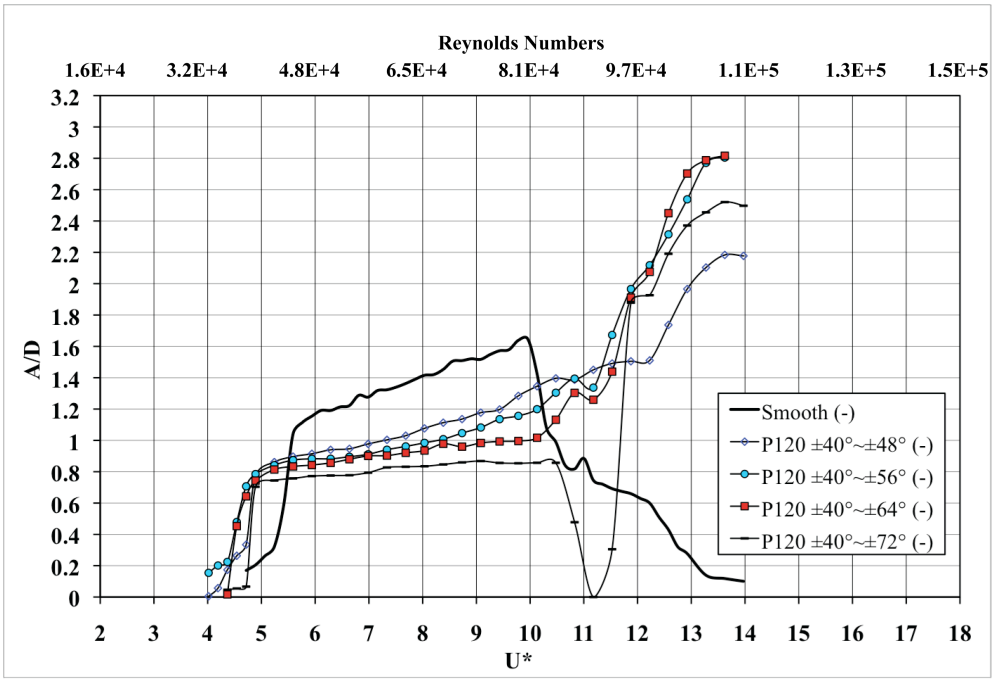

Figure 5.1. Cylinder responses at different strip area coverage.

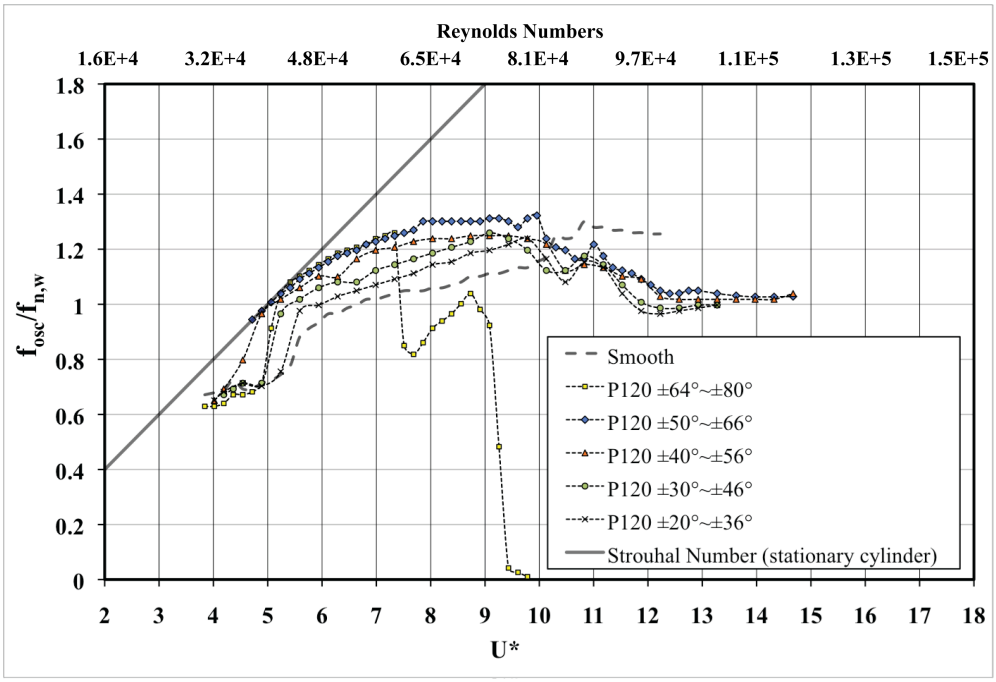

Figure 5.2. Frequency ratio versus reduced velocity for different strip area coverage.

Figure 5.2 shows the dependence of oscillation frequency on reduced velocity $U^*=U/(f_{n,w}D)$, which is proportional to Reynolds number. In the VIV synchronization range as well as the galloping range, the oscillation frequency is not significantly influenced by the surface area covered by roughness strips. For all roughness cases presented in this dissertation, the oscillation frequency for the roughness cylinders is constantly higher in the VIV synchronization range, compared to the smooth cylinder cases. However, in all cases of cylinder with PTC, the slope of oscillation frequency registers a declining trend for $U^* > 8.03$, where galloping begins.

As can be observed in Figure 5.2, in the VIV synchronization range ($5 < U^* < 8.03$) with roughness strips, the amplitude is less than that of the smooth cylinder; whereas PTC gives rise to galloping for $U^* > 8.03$. In addition, the closer the strips are to the front stagnation point - smaller strip placement angles (α_{PTC}) - the higher the maximum galloping amplitude in the range $20° \leq \alpha_{PTC} \leq 64°$ is. Also, in this range of α ($20° < \alpha_{PTC} < 64°$) corresponding to higher amplitudes (VIV synchronization range), the oscillation frequency is lower (Figure 5.2).

5.3. Effect of PTC on amplitude reduction in VIV

Overall, a significant reduction on oscillating amplitude is observed among all the studies of effect of PTC in Chapter 3, 4 and this chapter when the cylinder is in VIV. The flow mechanism on the circular cylinder attached with roughness under VIV is discussed in this section.

The effects from the sharp edge of PTC and surface roughness play a significant role in the lower reduced velocity range where VIV force dominates the cylinder response. The sharp edge and surface roughness can be both considered as a disturbance on the boundary layer at different level. Two flow mechanisms are observed:

a) Flow re-attachment: The edge of PTC functions like a “step” and in a sense it acts like a tripping wire being conjugated with three-dimensional roughness after the tripping wire. By introducing an isolated or distributed roughness surface around the cylinder body, discrete vortices in the scale of the roughness are formed. These

highly energetic eddies formed behind the roughness elements are produced within the prevailing boundary layer and energize the boundary layer. The small-scale vortices in the boundary layer result in a partially or even fully turbulent boundary layer if it is initially laminar or enhance the turbulence within the turbulent boundary layer. In the case of an initial laminar boundary layer on a smooth circular cylinder at subcritical Reynolds numbers, the transition of boundary layer from laminar to turbulent results in gaining momentum and it could possibly help to overcome an adverse pressure gradient and to delay flow separation as seen in Figure 5.4 (A) (Batham 1973, Huang 2006). As shown in Table 4 , the boundary layer thickness (δ) increases with α_{PTC} and decreases with Re. At smaller α_{PTC} values, flow separated at the upstream edge of the strip would possibly re-attach and stabilize as the flow progresses further downstream (as shown in Figure 5.4 (B)). When the VIV force dominates the vibratory response, due to the delay of separation point, there is less fluctuation of surface pressure distributed on cylinder surface. It results in a smaller F_y exerted on the cylinder. Comparing with results of circular cylinder without isolated or distributed roughness attached, a reduction of amplitude response is observed. Whereas, at larger α_{PTC} values, the flow would be more perturbed (less stabilization) because of roughness elements. This could be the reason for the higher response amplitudes in the VIV synchronization range at smaller α_{PTC} values in rough cylinder cases.

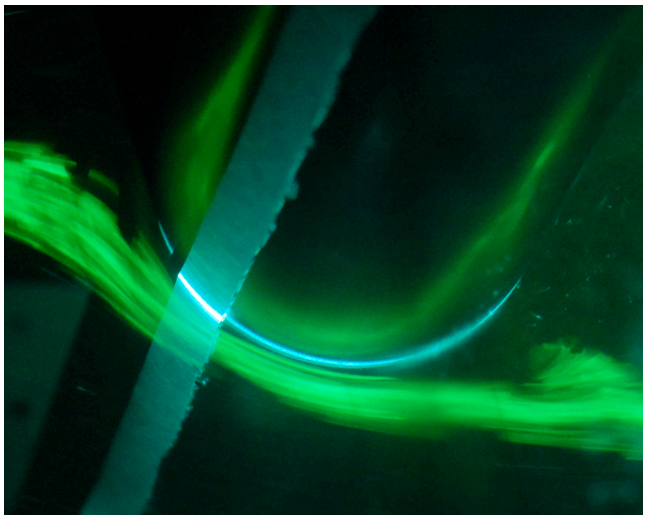

Figure 5.3. Visualization image of flow re-attachment.

(A)

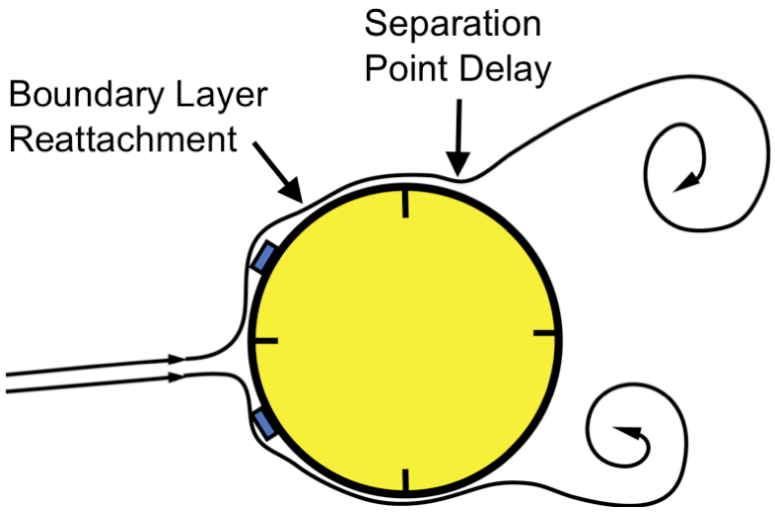

(B)

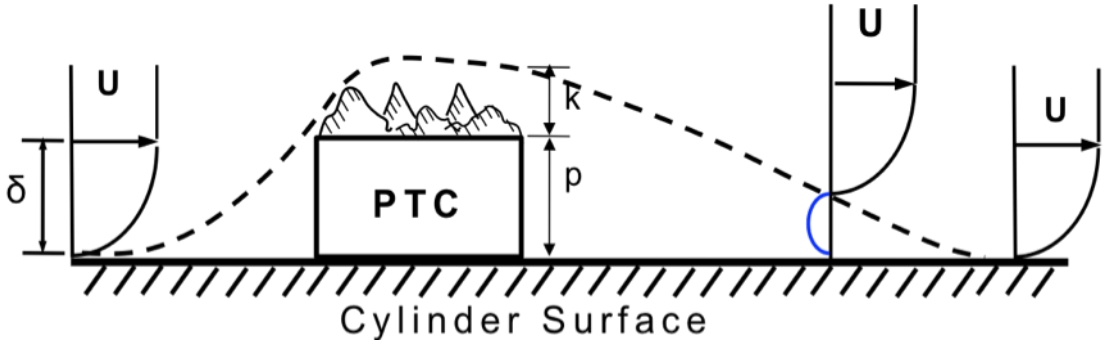

Figure 5.4. Simple schematic of flow attachment around circular cylinder with PTC.

b) **<u>Roughness protrusions</u>**: Furthermore, roughness protrusions could be expected to enhance the mixing of boundary layer δ'making the resultant vortices more diffused and hence, weaker, compared to a smooth cylinder case. This is reflected in the lower oscillating amplitudes in the VIV synchronization range for rough cylinder cases compared to the smooth ones. A simple schematic of this flow mechanism is shown in Figure 5.5.

The effect of roughness protrusions can be seen in the study on roughness coverage. In the case of a smaller coverage area of PTC (for instance, a one inch wide PTC strip), the flow re-attaches to a smooth surface area on the cylinder after being

triggered by the up-stream edge of PTC. Roughness protrusions only have a slight influence on VIV amplitude response. On the other hand, in the case of large coverage area of PTC, the flow re-attaches to the surface of cylinder covered by roughness and the effect of roughness protrusions weakens the vortices and results in reduction of vibratory amplitude. It can be verified by the results presented in Figure 5.1, the broader the strip (larger coverage area) is, the lower the VIV amplitude becomes.

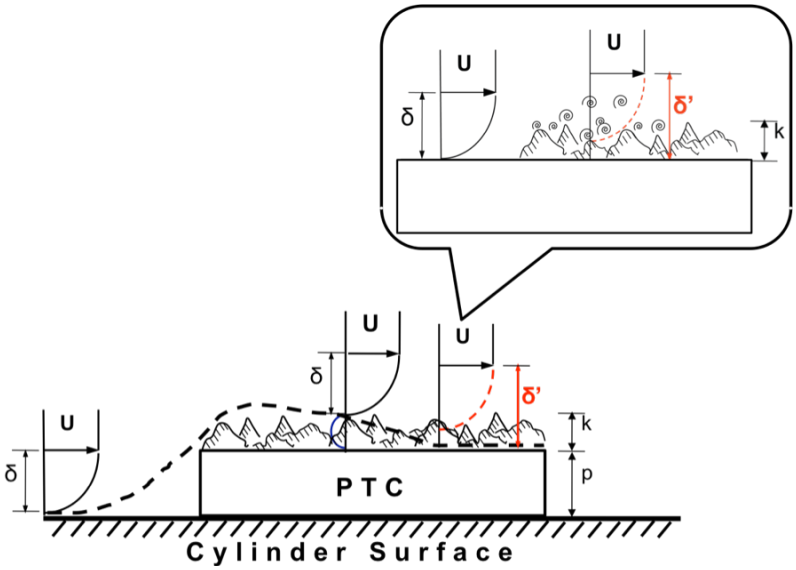

Figure 5.5. Simple schematic of flow around surface protrusions.

5.4. Critical location on the cylinder surface covered by roughness

Continuing the discussion from last section, for the strip angle α_{PTC} = 64°, VIV amplitudes are drastically suppressed which completely eliminate galloping. Frequency also exhibits a sharp decline for U* > 7 but with a local peak at U* ≅ 8.1 (Figure 5.2). For a circular cylinder, the natural separation point is near 76deg in the range of Re of the present study (Nishimura and Taniike, 2001; Achenbach, 1968). Hence, a re-attachment of the flow separating at the upstream edge of the roughness strip at α_{PTC} ≅ 64° is least possible. Further, in this case, the presence of roughness protrusions near the separation point would directly interfere with the roll up of shear layers adversely affecting it leading to this drastic diminution in the response amplitude as shown in Figure 5.1. It is worth noting that (k+P)/ δ <1 is placed at the start of synchronization for this case, where Re ≅

40,000. This is in agreement with the observations from Fage & Warsap (1929) that even small surface protrusions, which are smaller than the boundary layer thickness, may affect the flow characteristics particularly at higher Re values. Hover et al. (2001) also have noticed a significant reduction in the amplitude response, similar to the present case, with trip circular wires attached to a circular cylinder at an angle of 70deg from the front stagnation point.

As mentioned earlier, these results also show that the lower the strip angle is the higher the maximum amplitude of galloping excitation becomes. The exact reason for this correlation is not yet clearly understood. However, it can be inferred that there may be a relationship between the PTC placement angle α_{PTC} and the maximum flow incidence angle Φ_{max} in connection with the vibratory response of the cylinder. Specially, at a lower placement angle, the maximum flow angle of attack Φ_{max} is higher, where $\tan(\Phi_{max}) = 2\pi A/D/U^*$ (Luo, 1992), where A/D is the non-dimensional amplitude and U* is the reduced velocity. Φ_{max} is calculated at $U^* \cong 10$, where the oscillation frequency starts to decline indicating the onset of galloping. The Φ_{max} values are given in Table 6. It can be easily observed that the lower the α value is, the higher the Φ_{max} value becomes. To particularly note, for α_{PTC} =20° and α_{PTC} =30°, $\Phi_{max} > \alpha_{PTC}$, whereas for α_{PTC} values of 40° and 50°, $\Phi_{max} < \alpha_{PTC}$. That is, when the angle of attack fully encompasses the strip placement angle, higher galloping amplitudes occur. Otherwise, the amplitudes would be smaller.

As already mentioned in Section 3.4, there is a critical location (position of upstream edge of the strip) initiating galloping at α_{PTC} between 0° and 10°. For the upstream edge of the strip located at 0°, the vibratory response follows a trend similar to that of a smooth cylinder but with a slightly broader synchronization range. For strip edge at 10°, response exhibits galloping oscillations (Figure 5.1). It is interesting to note that, this range of 10° wide is within the range of oscillation of the front stagnation point (Ling Guocan, 1988). In this case, it is conjectured that change of the angle of attack does not introduce drastic geometric changes in the form of asymmetry in the flow structure, when the strip placement angle (considering the upstream edge of the strip) is within the angle of swing of the front stagnation point (~10°) disabling the possibility of galloping. Sur-

prisingly, the oscillation frequency is not affected at this critical location as Figure 5.2 shows. It may be inferred that, in this critical range of α_{PTC} , (k+P)/ δ is greater than 1.0, but appears to be not a deciding factor here.

Figure 5.1 shows that, in the VIV synchronization range (40,000<Re<80,000), the roughness height does not play a significant role in determining the magnitude of oscillatory amplitudes at a particular strip location. In fact, in this range of Reynolds number, at this specific strip location of α_{PTC}= 20°, the (k+P)/ δ ratio assumes values greater than 1.0 and less than 1.0, indicating that this ratio does not significantly contribute to the oscillatory characteristics, contrary to the expectations. However, Figure 4.1 shows that the roughness height markedly influences the oscillations of the cylinder under higher reduced velocities (U* > 10). It could be seen that the galloping branch is steeper for rougher strip. Furthermore, the roughness height does not considerably influence the oscillation frequency except for minor variations both in the VIV branch and in the galloping branch. In calculating the maximum angle of attack Φ_{max} at U* = 10, where the frequency of oscillation shows a sharp decline, the result indicates the commencement of galloping. It is observed that Φ_{max} decreases with increasing strip coverage area (θ), as Table 6 shows.

These results indicate that the broader the strip (larger coverage area) is, the lower the VIV amplitude becomes. For area coverage of 32deg, VIV oscillations are brought to near–zero amplitudes at U*≅11. It can also be observed that the broader the strip coverage in the range of 8° < θ < 24° is, the smaller the Φ_{max} becomes and the steeper the galloping branch appears. For a strip coverage area of θ = 32°, a complete separation occurs between VIV and galloping with a less steep slope. It is conjectured here that, as the strip becomes wider, it prolongs the interaction between the boundary layer and roughness because the boundary layer would be subjected to increased mixing and diffusion resulting in vortices with less strength. This could be the reason for the decreased amplitudes in the VIV synchronization range. However, the exact reason for the vibratory trends in the galloping branch is not yet understood, which warrants further investigation. In addition, the oscillation frequency is not significantly affected by the strip area cover-

age, as Figure 5.2 shows. It may be noted that, at α_{PTC}= 40° (location of upstream edge of the strip), for all these cases, the ratio (k+P)/ δ bears a value greater than unity at U* = 10 (Re~80,000) at which the difference in VIV amplitudes between various cases of strip area coverage reaches the maximum. However, at the end of the strip at 72deg, the ratio (k+P)/ δ comes closer to the unity value.

TABLE 6. MAXIMUM ANGLE OF ATTACK

Effect of Location

P120 PTC @	U*	Φ_{max} (degrees)	Slope
20°-36°	9.7	41.92	0.2450
30°-46°	9.08	40.03	0.2146
40°-56°	8.03	47.32	0.0770
50°-66°	7.8	48.15	0.0590
64°-80°	7.5	16.63	N/A

Effect of Roughness

PTC @ 20°~36°with	U*	Φ_{max} (degrees)	Slope
P150	9.7	40.86	0.1274
P120	9.7	41.92	0.2450
P80	9.7	41.92	0.2544
P60	9.7	41.92	0.3689

Effect of Coverage

Coverage area (degrees)	U*	Φ_{max} (degrees)
8° (40°-48°)	10	39.9°
16° (40°-56°)	10	36.25°
24° (40°-64°)	10	32.14°
32° (40°-72°)	10	28.57°

5.5. Conclusions

The following conclusions can be drawn from this chapter:

a) For certain PTC placement angles (location of upstream edge of PTC), the broader the PTC (larger coverage area) is, the lower the VIV amplitude becomes.
b) The broader the PTC is, the steeper the fully developed galloping branch becomes in lower reduced velocity.
c) The strip coverage area does not significantly influence the oscillation frequency.
d) All the rough cylinder cases exhibit higher oscillation frequency than that of the smooth cylinder cases.

CHAPTER 6

EFFECT OF PASSIVE TURBULENCE CONTROL ON VIVACE UNDER HIGH DAMPING

6.1. Background

Damping plays a very important role on VIV and galloping response. The energy generation of VIVACE is accomplished by the additional damping term imposed through the generator. A high damping is mandatory for energy extraction using VIVACE. The design optimization process requires that a high oscillating amplitude motion is maintained, under a high damping condition over a board range of synchronization. A high oscillation amplitude response (A/D >3.0) of galloping in low damping system has been achieved and discussed in the previous three chapters. High damping effects on VIV and galloping should be studied first before proceeding to the next step of study, introducing virtual damping for energy harnessing purpose. A complete study on the effects of PTC configuration - similar to the study in the previous three chapters - is reproduced in real spring damping (Real ck system) VIVAVE with an additional physical resistance (damping) generated by switching the type of bearings in the transmission system. With the additional damping, lower amplitudes result. The harnessed power from VIVACE is calculated and presented at the end of this chapter.

6.2. Damping identification for VIVACE

In order to have an extra damping force added to the existing system, modifications of transmission have to be made to adjust the system damping. The upper bearings of both sides are replaced by two less smooth types. The extra friction force is generated between bearings and shafts and results in an additional viscous damping ($c_{additional}$) in the system. The additional damping is assumed to be linear and only proportional to velocity

of motion. Through such a modification, the effects of PTC on VIVACE under high damping are investigated.

In this section, the total damping in the system (c_{system}) is divided into two component, structural damping ($c_{structure}$) and additional damping ($c_{additional}$) as follow.

$$c_{system} = c_{structure} + c_{additional} \quad , \tag{6.1}$$

where $c_{structure}$ is the damping coefficient found in the low damping real ck system used in the previous three chapters. $c_{additional}$ is the additional damping added to the system by adjusting linear bearing and this damping is assumed as harnessed damping for harnessed power calculation. The value of the system damping coefficient c_{system} can be obtained by performing free decay test as presented in Chapter 2.

To perform free decay tests, the restoring force is given by two real springs with total spring stiffness of 775N/m. Several free-decay tests were performed with three different values of initial displacement to find out the total damping coefficient C_{total} in the system. By performing these free-decay tests, the C_{total} can be estimated. Given equation (6.1), $C_{additional}$ can be calculated by subtracting $C_{structure}$ from C_{total}. The results of the nine tests and estimated damping are listed in Table 7.

TABLE 7. SYSTEM DAMPING INDENTIFICATION RESULTS

	initial displacement (m)	C_{total} (Ns/m)	ζ_{total}	$C_{additional}$ (Ns/m)	$\zeta_{additonal}$
Test 1	10	17.27	0.099	14.07	0.081
Test 2	10	17.05	0.098	13.85	0.079
Test 3	10	16.89	0.097	13.69	0.079
Test 4	15	18.04	0.104	14.84	0.085
Test 5	15	17.8	0.102	14.6	0.084
Test 6	15	18.12	0.104	14.92	0.086
Test 7	20	18.01	0.103	14.81	0.085
Test 8	20	17.78	0.102	14.58	0.084
Test 9	20	18.23	0.105	15.03	0.086
Average		17.688	0.101	14.488	0.083
Standard deviation		0.493	0.0028	0.493	0.0028

The less-smooth type bearings were the first time used in the test. The linearity of this additional damping needs to be verified. To complete the validation, a smooth cylinder test is carried on in the LTFSW channel and vibratory response is used to compare with the results from the Vck system with the most similar system setup.

System properties of both real spring-damper VIVACE and virtual ck VIVACE are listed in Table 8. A comparison on oscillation amplitude is plotted in Figure 6.1. In Figure 6.1, the vibratory amplitude from the real spring-damping and V_{ck} VIVACE systems exhibit a very similar trend and synchronization range from real-damper spring system shifts slightly to right-hand side of plot (higher flow speed) due to the slightly higher value on natural frequency of the device.

TABLE 8. SYSTEM PROPERTIES OF REAL SPRING VIVACE AND V_{CK} VIVACE

	Real Spring 775N/m	V_{CK} system 800N/m
D, cylinder diameter (m)	0.0889	0.0889
m_{osc}, oscillating mass (Kg)	9.78	10.75
K, stiffness (N/m)	775	800
C_{total}, total damping coefficient (Ns/m)	17.69	19.17
ζ_{total}, total damping ratio	0.102	0.103
$f_{n,water}$, natural frequency in water	1.127	1.111

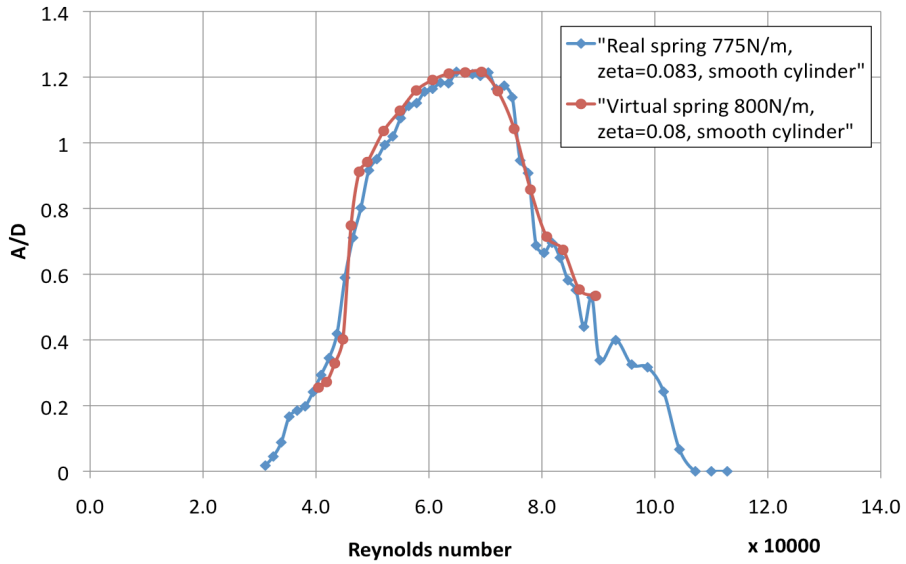

Figure 6.1. Amplitude response from system calibration test.

6.3. Experimental results and discussion

Results of effects of PTC under high damping conditions are presented in this section. The following observations and discussion are made based on examining the two significant vibratory responses of FIM, oscillating amplitude and frequency. Harnessed power is calculated and effects of PTC on power generation on VIVACE are investigated.

oscillating amplitude

Results of the amplitude ratio versus flow velocity U, reduced velocity U*, and Reynolds number Re_D for different PTC configuration are shown in Figure 6.2 through Figure 6.4. Several observations are made below.

Response of cylinders with PTC location at 30deg in low damping (ζ_{system}= 0.016) and high damping (ζ_{system}= 0.102) are presented for an overall comparison in Figure 6.3, which shows the cylinder response features for two damping ratios, ζ_{system}=0.016 (low damping VIVACE) and 0.102 (damping added), respectively. Smooth cylinder response is also plotted to better demonstrate the effect of damping. As seen inigure 6.2, even though the overall oscillatory trends for rough and smooth cylinders are similar, distinct differences can be observed. For smooth cylinder, a higher damping ratio subdues the excitation amplitude and reduces the range of synchronization. The reduction in amplitude response is about 24.24% for an increase in the mass-damping parameter by a 637.5%. Additionally, the initial branch becomes less steep (gradual) with an increase in damping, though the amplitudes are higher (at higher damping) in the quasi-periodic regime (very beginning) of the initial branch.

Interestingly, for the rough cylinder cases with PTC, an increase in damping brings a notable reduction in amplitude both in the VIV synchronization range and also in the galloping branch as can be seen in Figure 6.2.

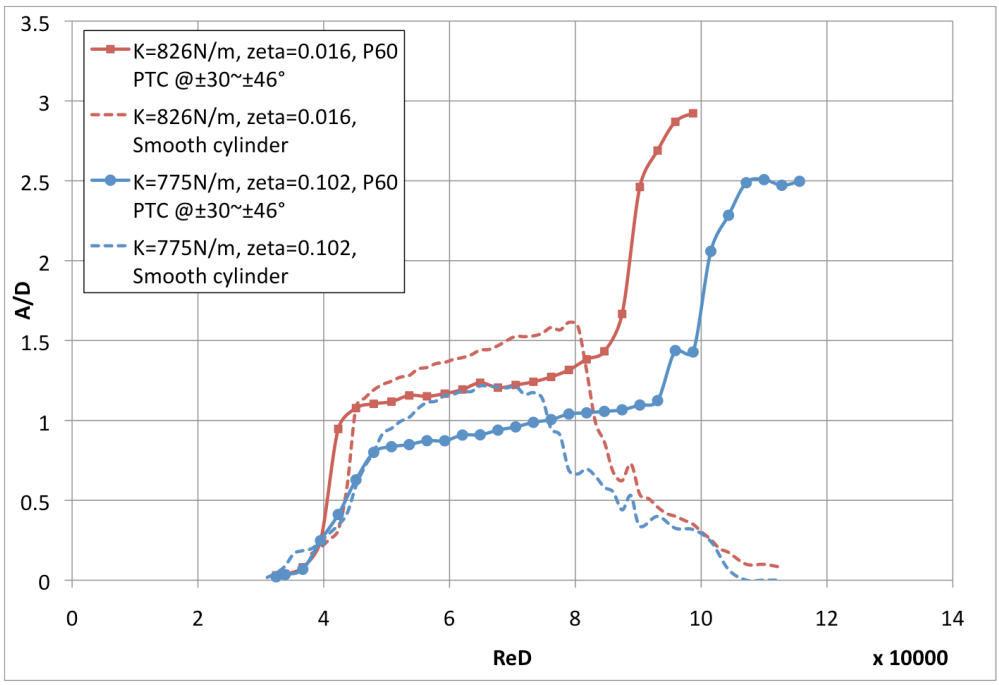

Figure 6.2. Cylinder oscillatory response characteristics at higher damping.

Figure 6.3 shows the effect of PTC location under higher damping. The results at various PTC locations ranging from PTC placement angle α_{PTC} from 10deg to 60deg for the roughest strip surface P60 are plotted. It is to be noted that locations specified correspond to the upstream edge of the roughness strip (strip placement location). The smooth cylinder response is also in the background to better appreciate the effect of surface roughness. It can be noticed that, except for the case with PTC at 10deg, the response switches from VIV to galloping without any significant amplitude drop for U*>11.0 (Re: 8.31×10^4). It can be observed that amplitude drops-off resembling smooth cylinder desynchronization at about U*=11.5 (Re: 9.0×10^4), and then, sharply picks-up after U*=12.0 (Re: 9.4×10^4). In addition, at this angle (α_{PTC}=10°), the VIV branch and galloping branch are better separated compared to other cases. Furthermore, it can be seen that, for lower damping cases (Chapter 3, Sections 3.3, 3.4, Figure 3.2), the peak amplitude during galloping is higher. For the strip location at 60deg, an acute suppression of oscillatory amplitudes occurs with maximum A/D<0.40 with the complete absence of galloping. For all other strip locations, the overall vibratory trend is more or less the same but it exhibits notable differences. For instance, in the range of α_{PTC}=30deg to 50deg, the farther

the strip is from the front stagnation point, the lower the maximum galloping amplitude becomes, as demonstrated in Figure 6.3. In the lower range of strip location, i.e., between 10deg and 30deg, no specific trends are recorded. In general, the strip location closer to the front stagnation point makes the galloping branch steeper. It is further noted that, in all these roughness cases, the cylinder suffers loss of amplitude in the VIV upper branch compared to the smooth cylinder, this phenomenon is similar to what has been observed in the case of lower damping ratio (discussed in the Chapters 3, 4 and 5). Again, in the VIV synchronization branch, higher amplitude response is observed at smaller strip placement angles. It can also be seen that, roughness (PTC) triggers an early onset of oscillations that is at lower reduced velocities, compared to the smooth cylinders.

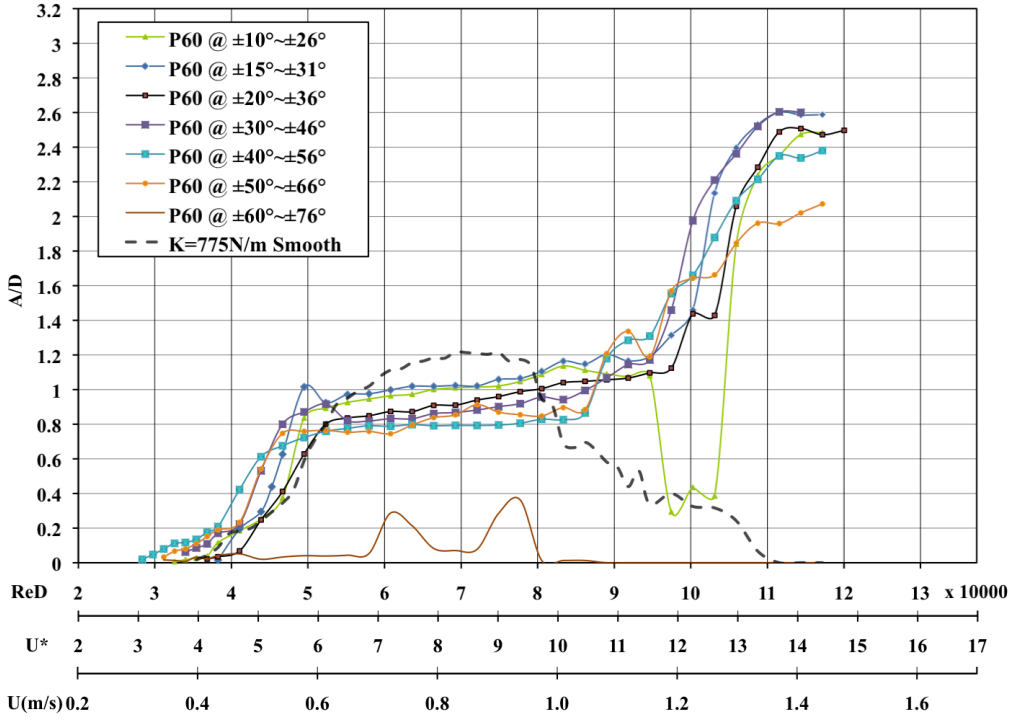

Figure 6.3. Effect of PTC location on oscillations at higher damping.

The results of response featuring at different roughness heights are shown in Fig.6.4. As can be seen, with rougher PTC surface, the steeper fully developed galloping branch is shifted to lower reduced velocity, along with a higher maximum of excitation amplitude. As observed from results from effect of PTC location, rough cylinder VIV upper

branch suffers loss of excitation amplitude compared to the smooth cylinder but with early onset of oscillations also exhibiting a steeper initial branch. To recall, a frequency drop (at U*~10, Re~7.9×10^4) indicates the point at which a negative hydrodynamic damping starts to act, thus, indicating the onset of galloping whereas the steeper galloping branch (amplitude shoot up) occurs at a higher reduced velocity (U*~11.5, Re~9.0×10^4). In other words, there is a transition region where the hydrodynamic damping grows more negatively with a reduced velocity until it is sufficient enough to cause an abrupt increase in the response amplitude. A great deal of interaction between VIV and galloping is expected to take place in this transition zone. A combined response of VIV and galloping is quite possible as perceived by previous investigators (Blevins, 1977; Corless and Parkinson, 1988).

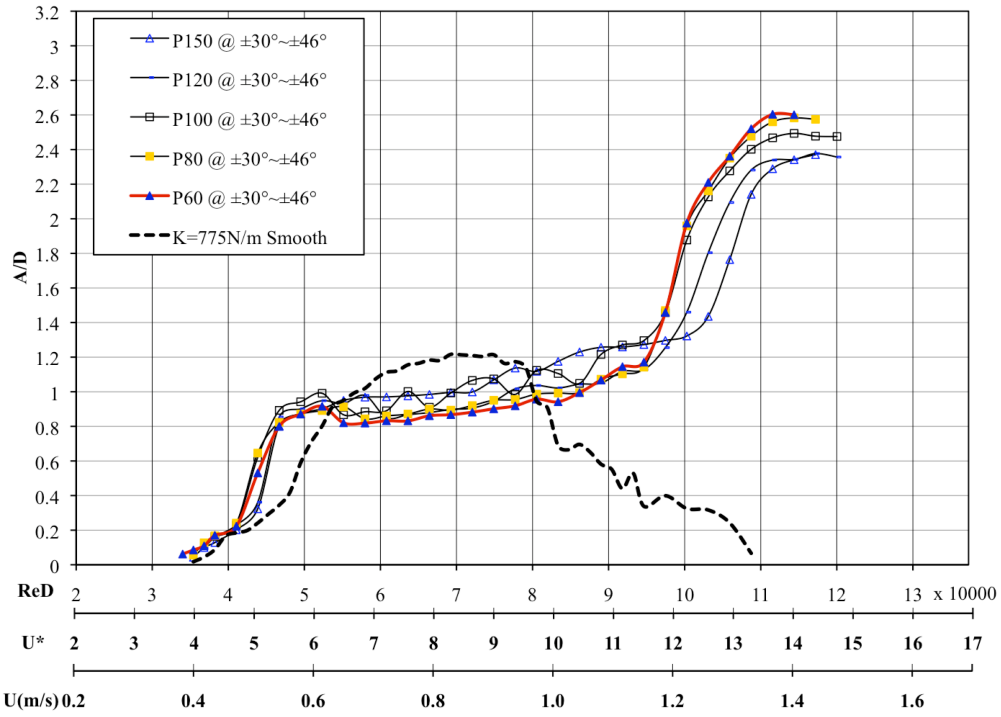

Figure 6.4. Effect of PTC roughness on oscillations at higher damping.

oscillating frequency

The results of oscillating frequency ratio versus flow velocity U, reduced velocity U*, and Reynolds number Re_D for different PTC configuration are shown in Figure 6.5 and

Figure 6.6. As shown in these figures, the overall frequency response characteristics in high damping are similar to that of lower damping, which exhibit an increasing trend up to a certain value of reduced velocity and then decline to lower values. As noted in the lower damping cases presented in Figure 3.3, U^*_{gallop} occurs from 7.2 to 9.7 with a decrease of the PTC placement angle. That means that in the galloping range, the smaller the placement angle is the higher the reduced velocity at which the galloping instability occurs is. This trend can be observed from the results presented in Figure 6.5.

In general, the oscillation frequency is higher for the configuration P60 at 40deg to 56deg over the entire range of reduced velocity. Up to a strip placement angle of 40deg, the higher the roughness is, the higher the oscillation frequency becomes. Thereafter, the oscillation frequency shows a marginal decline exhibiting a more uniform profile (much less pronounced 'kink' at U*=10.2), unlike other cases. It is critical to note that a rough cylinder undergoes faster oscillations in the VIV branch ($U^* \leq 8.5$) and slower oscillations at the onset of galloping ($U^* > 8.5$).

It is surprising to see that roughness does not significantly influence the magnitude of response frequency throughout the reduced velocity as Figure 6.6 shows. More or less, this is what is observed in the lower damping cases as well (Figure 3.3). All other general characteristics are similar to what was presented in Figure 6.5.

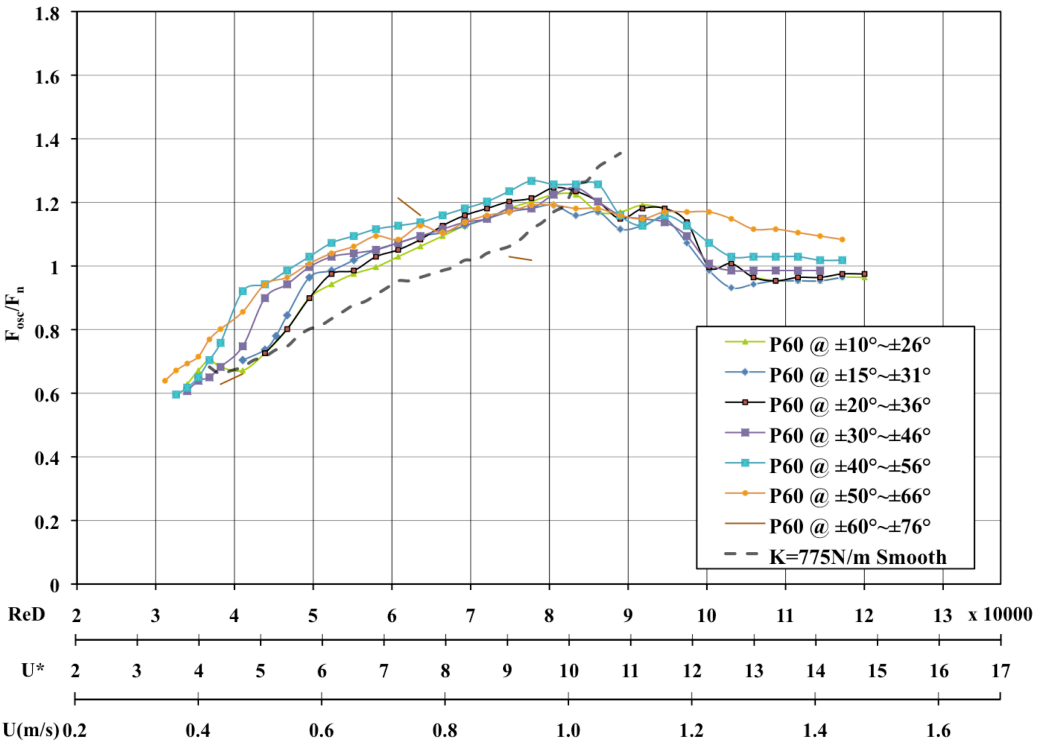

Figure 6.5. Effect of PTC location on frequency response at higher damping.

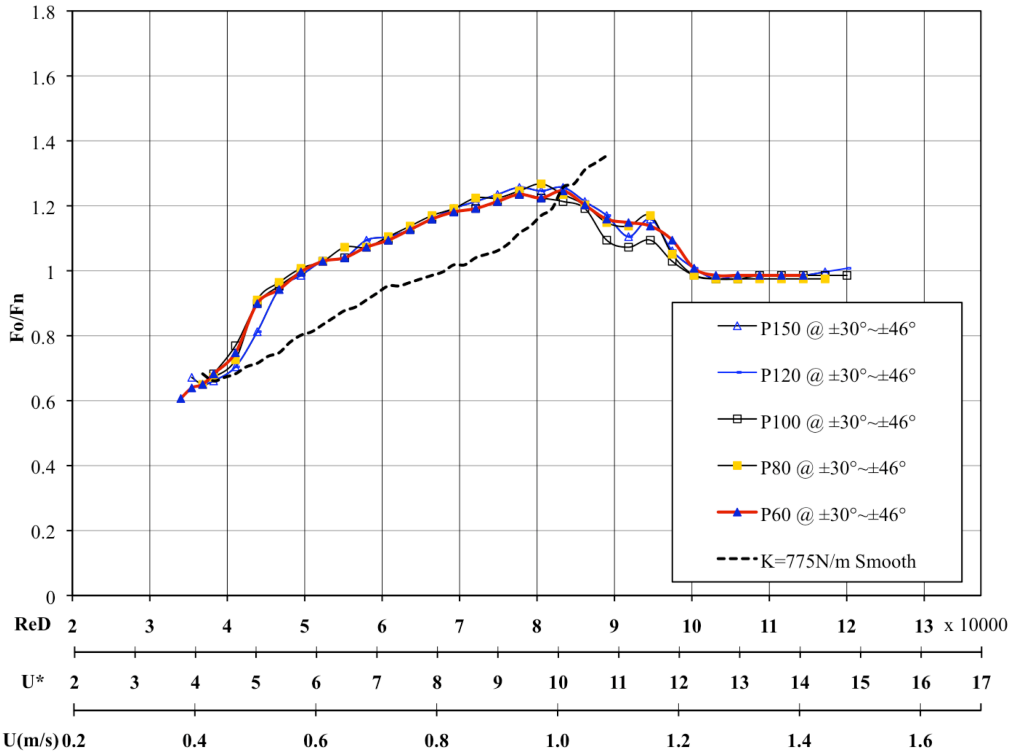

Figure 6.6. Effect of PTC roughness on frequency response at higher damping.

harnessed energy

The power that can be harnessed by VIVACE is the power extracted by the generator, which is equal to the power VIVACE extracts from the fluid minus the power dissipated by structural, transmission, and internal generator losses (see Section 9.6). To simplify calculations, we assume that the damping force from the generator, which converts the mechanical energy to electrical energy, is in phase with the velocity term and it behaves in the same way as the structural and transmission damping. Harnessable power on VIVACE can be calculated as following (see Section X.X for derivation):

$$P_{VIVACE-mech} = 8\pi^3 (m_{osc} + m_a)(\zeta_{system} - \zeta_{structure})(y_{\max} f_{osc})^2 f_{n,water} \tag{6.2}$$

Where ζ_{system} is defined as $\zeta_{system} = \zeta_{structure}+\zeta_{harn}$ where the additional damping, $\zeta_{additional}$ represents harnessed damping, ζ_{harn} in this chapter. Thus, harnessed power can be calculated based on the known factors from the experimental results.

The calculated harnessed power versus flow velocity U, reduced velocity U*, and Reynolds number (Re_D) for different PTC configurations are depicted in Figure 6.7 through Figure 6.11.

One of the major objectives of the present study is to examine the hydrokinetic energy harnessed from flow-induced motions of the cylinder with PTC. Figure 6.10 portrays the power plots for various PTC configurations with P60 PTC. The general trend of power curves is quite similar to those of the amplitude plots for these cases. It can be seen that the power generated in the range of fully-developed galloping (U*>11.0) is much higher than that harnessed contributed when the system is undergoing VIV. This fact categorically proves the main advantage of PTC application with respect to energy harnessing. For PTC location closer to the front stagnation point, harnessable energy from VIV is higher than other cases. Among all the strip locations, the poorest performance is observed in the test with PTC at 60deg-76deg. For the configuration P60 at 50deg to 66deg, power production appears to be the second lowest but with a higher value in the transition reduced velocity range, 11.0≤U*≤12.5. It is further seen that, in this PTC placement location, energy harnessed from rough cylinders is higher even in the VIV

synchronization range compared to that for smooth cylinders.

An advanced investigation aims to study the effect of surface roughness. Results at a particular PTC location, 30deg, are presented in Figure 6.11. Among all the cases tested, the roughest strip P60 is found to be associated with higher harnessable power for $U^*>11.5$, corresponding to the fully developed galloping branch yet generating only minimum power in the lower reduced velocity range ($U^*\leq 9.5$). In general, all the PTC roughness cases invariably deliver higher power than smooth cylinders except in a range of reduced velocity $6.5\leq U^*\leq 9.4$, where the power output for the smooth cylinder is of comparable magnitude with the rough cylinder cases. Interestingly, the maximum power value at $U^* \cong 14.5$ is higher for rougher cylinder. Also, as the strip roughness increases, the power curves shift towards the lower reduced velocity in tune with the amplitude response as depicted in Figure 6.4. PTC roughness enables higher power production even at lower reduced velocities, compared to smooth cylinder, as Figure 6.11 shows.

Harnessable power results with smooth PTC of varied thickness are shown in Figure 6.7. As Figure 6.7 illustrates, the higher the strip thickness is, the greater is the power output. Such correlation is particularly evident at higher U^* values $U^*\geq 11.5$. For $U^*<11.0$, under all other T values except for T=0.095 (lowest value tested), the power trends are close to each other with only minor differences between them. For T=0.095mm, the power profile is somewhat similar to that of the smooth cylinder but with surprisingly lower values. That is, there is a limiting thickness above which only a substantial power output can be expected. The exact value of this limiting thickness is not ascertained in this study though it is obvious that it lies between 0.095mm and 0.197mm for a 3.5inch cylinder. Non-dimensionally, T/D (D=cylinder diameter) should lie between 0.001069 and 0.002216. The results further suggest that, strips with thickness lower than the limiting thickness disable power generation.

It is interesting to observe that, roughness promotes better power harnessing as shown in Figure 6.8. For the same total thickness of PTC, a rough strip performs better since it enables higher power production than a smoother strip. This is particularly evident in the fully-developed galloping excitation zone $U^*\geq 11.5$. However, in the VIV up-

per branch regime, the smooth PTC power production marginally overtakes the rough PTC. Interestingly, the smooth PTC performance outplays that of the rough cylinder in the VIV upper branch regime essentially because both smooth and roughness PTC partially suppress the amplitude of excitation.

The power generation potential for smooth and rough PTC is further explored for comparison purposes, and the results are shown in Figure 6.9. It can be seen that, a higher roughness contributes to higher power generation at higher reduced velocities U*>11.5. At lower reduced velocities U*<11.5 on the other hand, an introduction of rougher PTC leads to lower power output in the cases that the total thickness of both PTC are the same. Furthermore, results from a smooth PTC with smaller total thickness are introduced in the same figure for comparison. The power curve of smooth strip is found to follow closely the trend of the smaller roughness case (P150) up to U*=11.5. Thereafter, it exhibits significantly lower values than that of the rough cylinder case which follows an increasing trend with U*.

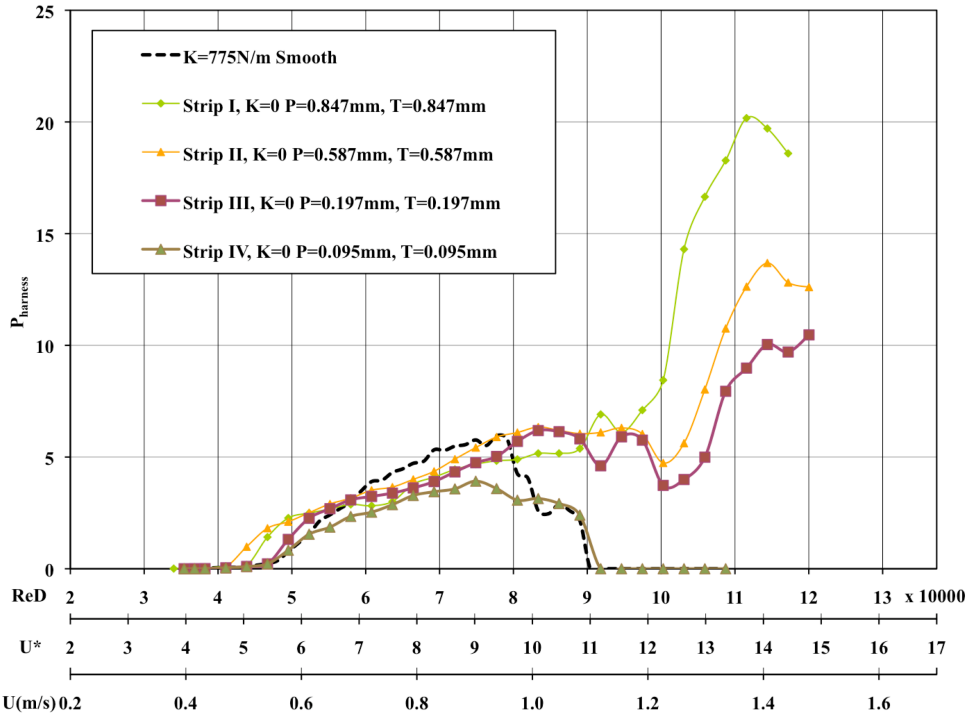

Figure 6.7. Harnessed power with different smooth PTC: effect of strip thickness.

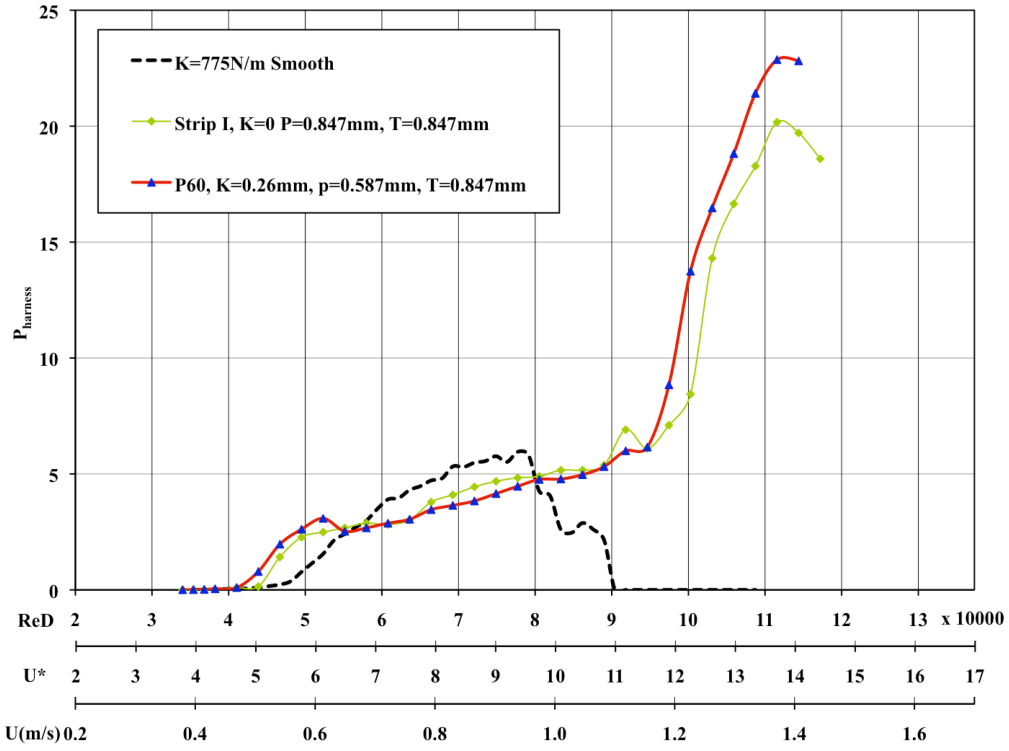

Figure 6.8. Power harnessed for smooth and rough PTC having same total thickness.

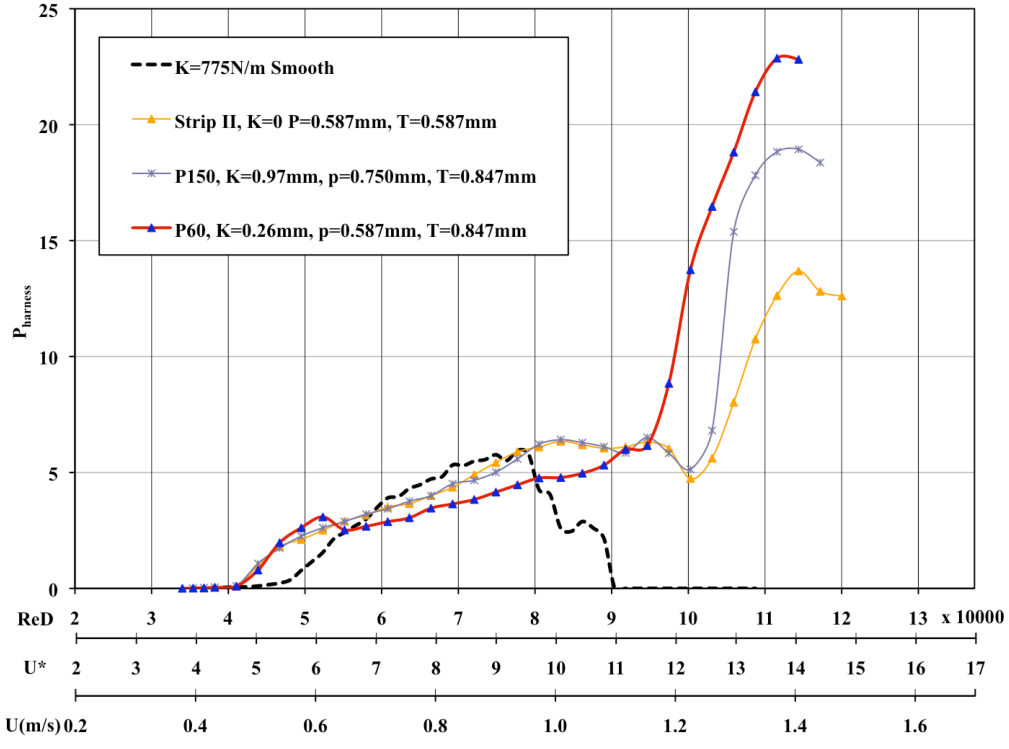

Figure 6.9. Comparison of harnessed power for smooth and rough PTC.

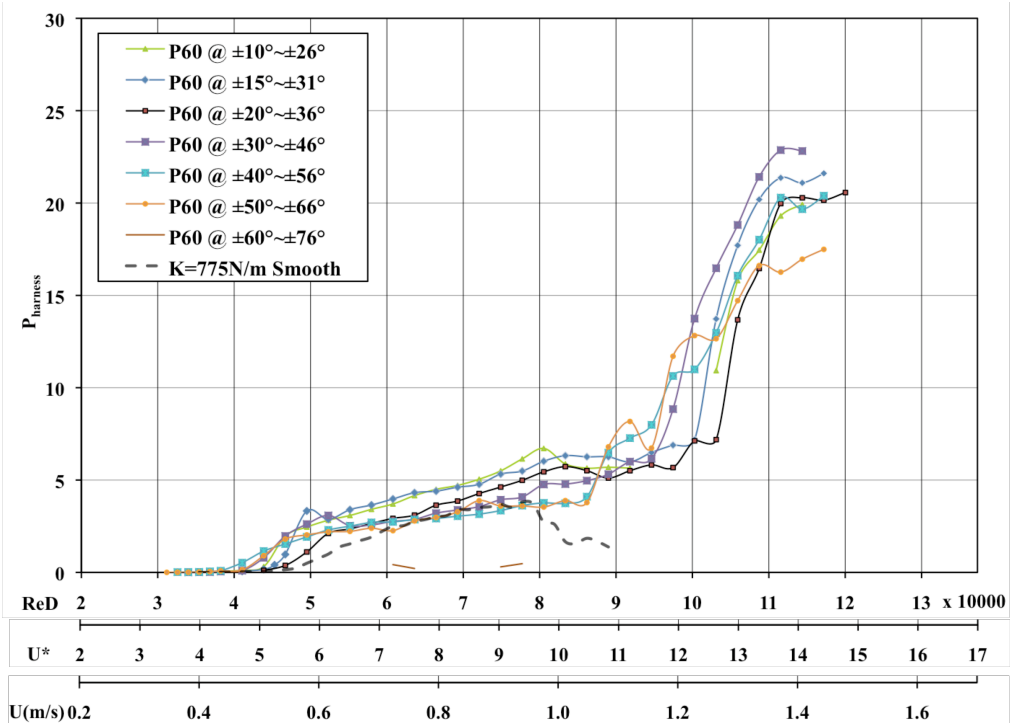

Figure 6.10. Harnessed power with PTC at different PTC locations.

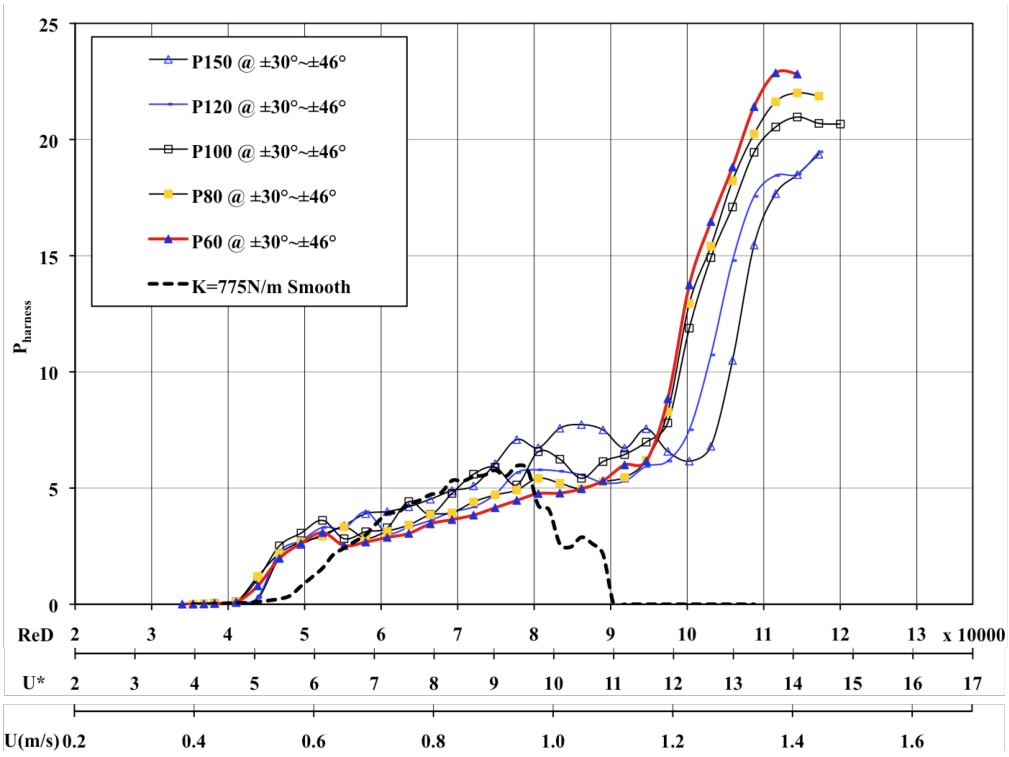

Figure 6.11. Harnessed power for different PTC roughness at a strip location of 30deg.

6.4. Conclusions

The following conclusions can be drawn from the study in this chapter:

a) Higher damping subdues amplitude of oscillation while all other parameters remain the same.

b) PTC roughness induces higher oscillatory amplitudes at higher reduced velocities where fully-developed galloping takes place, while partially suppressing amplitude at lower reduced velocities where VIV occurs.

c) PTC height influences the oscillatory amplitude of the cylinder. Thicker PTC enables higher power production at higher U* values. Frequency response is least influenced by PTC roughness.

d) Apart from the magnitude of PTC roughness, its location plays an important role in the oscillatory amplitude and frequency features of the cylinder. There appears to exist an optimal PTC placement angle, which can contribute to higher power output occurring at higher reduced velocities. At some location, at lower U* values, power output is 'de-generated' irrespective of the roughness value and position.

e) A thicker PTC is proven to facilitate higher power generation at higher reduced velocities. At lower reduced velocities, the power output is much lower and is not significantly different from that of a smooth cylinder irrespective of the roughness value.

f) As is true for amplitude, for the power output, there appears to exist an optimum circumferential strip location contributing to maximum power production. Up to a certain circumferential angle, there is increased power output. Thereafter, it is attenuated for farther downstream locations of the strip. Power generation is much higher at higher reduced velocities (galloping zone). At lower U* values, there occurs a collapse of power data somewhat close to those of smooth cylinder except for minor differences.

g) Cylinders with smooth surface PTC also deliver power output similar to rough cylinders in comparable but slightly lower magnitudes. This indicates that, roughness is not mandatory to promote higher power generation but certainly displays as a desirable factor.

CHAPTER 7

EFFECT OF VARIED DAMPING AND STIFFNESS ON VIVACE WITH PTC FOR POWER HARNESSING

7.1. Background

As presented in Chapter 6, Lee's (2009) V_{ck} model has been verified to function correctly under high damping conditions, where the Passive Turbulence Control (PTC) is introduced. In this chapter, experimental results at high damping conditions with PTC for power harnessing using the V_{ck} model are further investigated. With PTC, apart from Vortex-Induced Vibrations (VIV), high amplitude galloping oscillations are also observed in the present study. The primary reason to test galloping under high damping is to find the optimized level of energy generation with the introduction of surface roughness to the system.

A virtual damper/spring (V_{ck}) VIVACE converter was built by Lee (2009) to study effect of stiffness and damping on VIV. System damping is modeled by a proposed nonlinear dynamic damping model, which add artificial electrical damping (external damping) for energy harnessing. Damping model identification have been successfully preformed in the Low Turbulence Free Surface Water Channel at University of Michigan. Through many VIV tests the V_{ck} system has been extensively verified. However, the V_{ck} VIVACE converter has not been tested in high amplitude, high flow velocity conditions until the commencement of the present study.

A series of experiments at various damping ratios and spring constants were conducted using the V_{ck} VIVACE converter with PTC applied on the cylinder surface. Experimental parameters are listed in Table. 1. The results are presented in form of amplitude and frequency response plots.

TABLE 9. EXPERIMENTAL SYSTEM PARAMETERS FOR V_{CK} SYSTEM

Operating system	Virtual damping spring VIVACE converter
D: diameter of cylinder (m)	0.0889 (3.5" cylinder)
L: length of cylinder (m)	0.9144
Aspect ratio	10.29
m_{osc}: total mass of oscillation (kg)	10.75
m_{eff}: effective mass (kg)	2.05
m_d: displaced mass (kg)	5.67
m*: mass ratio	1.88
K: stiffness (N/m)	400 to 2000
$f_{n,water}$: natural frequency in calm water (Hz)	0.78 to 1.76
$C_{structure}$: structural damping (Ns/m)	3.2
ζ_{harn}: extra damping ratio for energy harnessing (Ns/m)	0.04, 0.08, 0.12, 0.16

7.2. Effect of stiffness on the V_{ck} VIVACE with PTC

This section aims to examine changes in amplitude and frequency characteristics of the oscillatory system with the introduction of surface roughness (PTC) under varying stiffness and damping. Experimental data with varied stiffness are presented and discussed. Lee (2009) has conducted various sets of experiments, using VIVACE without roughness surface (PTC) i.e., for a smooth cylinder. This section compares the results of VIVACE with PTC and VIVACE with smooth cylinders obtained by Lee (2009). Output consists of amplitude and frequency response and energy output.

Furthering the studies conducted using the V_{ck} system on a smooth cylinder by Lee (2009), studies with rough cylinders (PTC applied) are conducted primarily aiming at generating more power from the V_{ck} oscillatory system besides investigating the dynamic response of the same. All the results presented here correspond to a PTC configuration of P60:20-36deg. Amplitude response of a rough cylinder at different K values is shown in Figure 7.2. As previously pointed out, these results essentially show the variation of amplitude, frequency response, and power output on the system damping ratio ς and stiffness K. With the softest spring (lowest K value), a very broad VIV synchronization region is obtained before the cylinder goes into galloping and exhibits the highest peak amplitude in VIV among all the cases tested. In the VIV synchronization range, maximum

amplitude reduces with increase in K value. It can also be noted that, onset of oscillations commence at lower Re values as K becomes smaller. It is clearly seen that the higher the stiffness is the lower peak galloping amplitude is attained. Also, at higher K the galloping branch is steeper and picks up at lower Re.

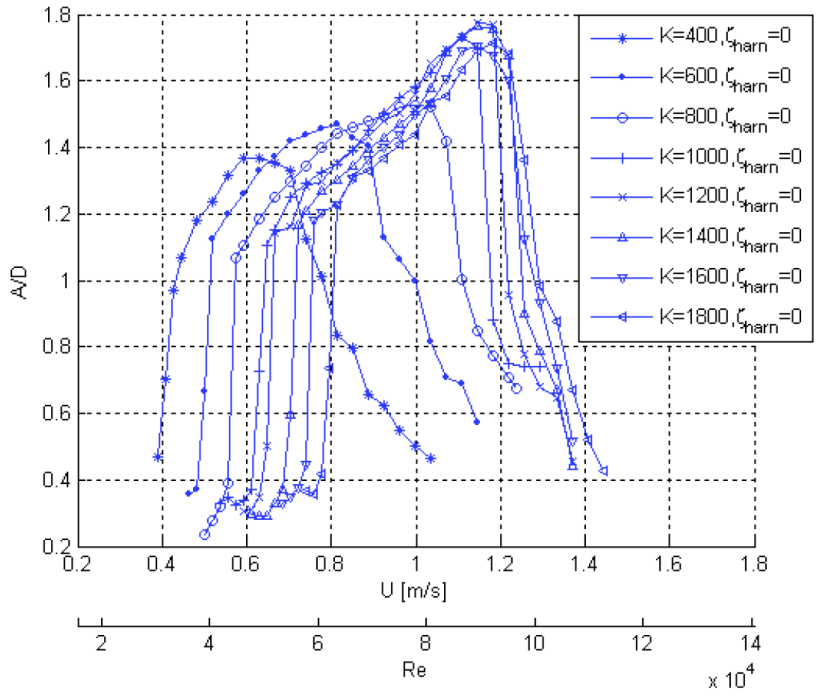

Figure 7.1. Smooth cylinder responses at different stiffness values with no external damping. (Lee, 2009)

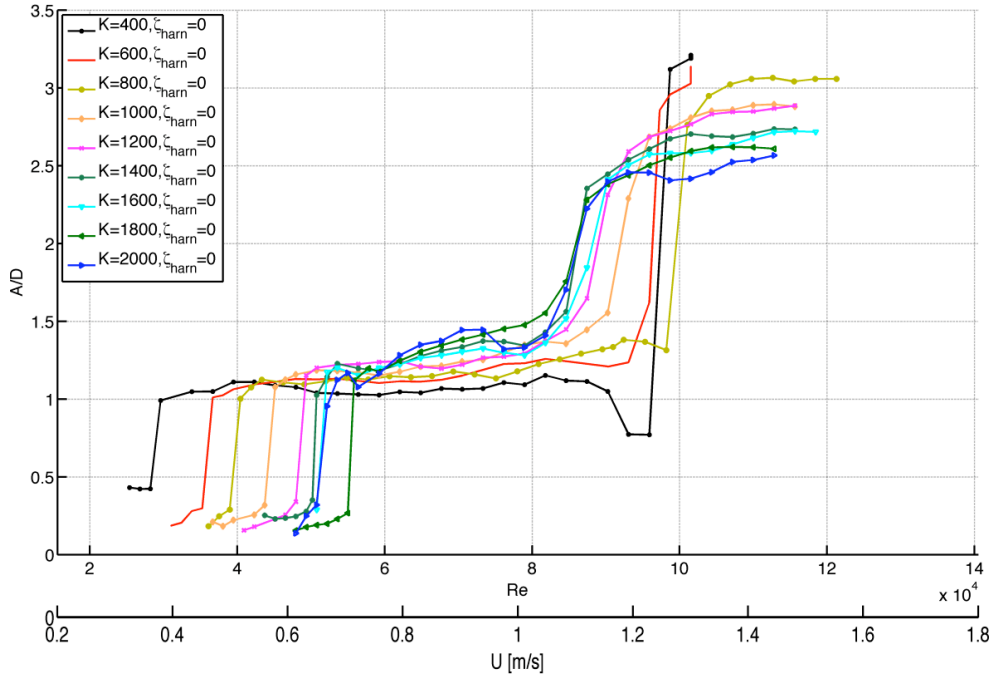

Figure 7.2. Rough cylinder oscillatory responses at different stiffness values at no external damping.

As depicted in Figure 7.2, cylinder oscillations show the characteristics of vortex-induced vibrations up to a certain value of Reynolds number. Thereafter, galloping occurs. This is ascertained from the amplitude and frequency features further evidenced by flow visualization results. For each case of K value, it can be seen that, oscillations are initiated at certain Re value determined by the natural frequency of the system. Ensuing oscillations increase following the initial branch, which is further followed by the upper branch exhibiting higher amplitudes of oscillation. As can be seen, till an abrupt increase takes place, amplitude increases only very gradually with respect to Reynolds number or reduced velocity clearly exhibiting 'self-limiting' characteristic that are typical of VIV. Furthermore, a study of near-wake structure (Chapter 11) shows that respective vortex structures are nearly consistent in the initial and upper branches. To particularly note, vortex shedding frequency is nearly invariant with respect to reduced velocity particularly in the upper branch, as present visualization studies show. This demonstrates that, vortex-shedding frequency is 'locked-on' to the natural frequency of the system, which further confirms that the cylinder is experiencing VIV and not any other kind of instability. On the contrary, wake structure in the high amplitude (following an abrupt increase)

and lower frequency branch, is very different with significantly higher number of vortices shed per cycle of oscillation (about 10 per cycle) as evidenced in the present visualization study and therefore, ascertained as galloping. Due to system limitations, galloping response features cannot be studied at Re values larger than 118,000. Yet since the vibratory traits confirm galloping type of instability at higher Re as mentioned before, it is conjectured that, vortex shedding frequency should show an increase with further increase in Re value or a reduced velocity.

As pointed out earlier, a steeper galloping branch picks up at lower Re for higher K. Further, it should be noted that, the separation between VIV and galloping increases as K value decreases (or damping ratio increases). For all these cases, oscillation frequency starts to decline at about $Re=8.0\times10^4$. Meanwhile, an abrupt increase in amplitude (galloping branch) occurs at a still higher Re value. For lower stiffness cases, the VIV upper branch is extended beyond the point of frequency drop before it collapses to the galloping branch. This is probably due to the fact that for lower stiffness cases, the damping ratio will be higher. For galloping to fully commence, the total damping should become negative. Note that, the hydrodynamic damping is proportional to the flow velocity or Reynolds number. Therefore, starting from the point of frequency drop (where negative hydrodynamic damping starts to act), for lower stiffness cases (higher damping ratio), higher Re aims to induce sufficient negative hydrodynamic damping so as to cause an amplitude up shoot. Whereas, at higher stiffness and the system damping ratio being smaller, induction of small amount of negative hydrodynamic damping is sufficient for the galloping to fully commence and this will occur at relatively low Re values as evident from Figure 7.2. Due to this reason, at high K values, the transition from VIV to galloping happens without any ‘kink’ in the response branch and the slope of transition is positive (upwards).

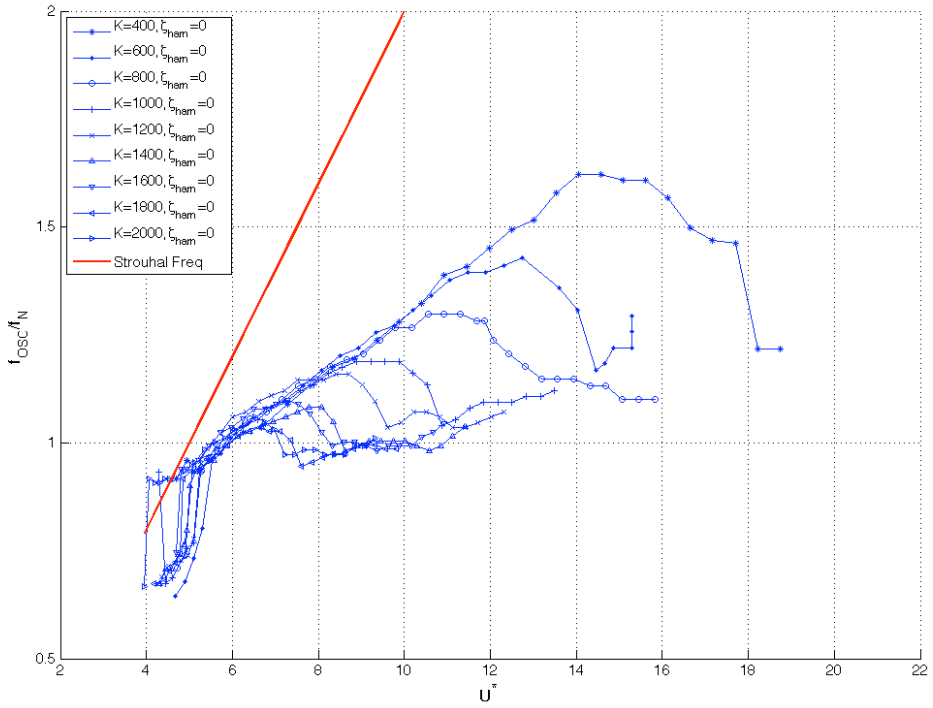

Figure 7.3. Oscillation frequency features at different stiffness values at no external damping.

The frequency response features are shown in Figure 7.3. In all cases, as can be seen, the oscillating frequency follows an increasing-decreasing trend. The higher the K value is, the higher is the reduced velocity at which frequency drops. But, the Re value at which this drop occurs is nearly the same in all the cases irrespective of the K value, viz., at $Re=8x10^4$. It is suggested that, at this Re value, roughness induces an early transition of the boundary layer from laminar to turbulent due to the 'drag crisis' being shifted to a lower Re value (for a smooth cylinder, drag crisis occurs at about $Re=3x10^5$). It is to be noted that, as the name indicates, C_D undergoes a significant drop at the drag crisis (Achenbach and Heinecke 1981). It is thought that, simultaneous with drag crisis, hydro-dynamic damping becomes negative indicating the onset of galloping instability as could be shown by the basic derivation of the pertinent physics modeled by equations (10.12) to (10.18) (Blevins 1977). It is also reflected that there is a progressive induction of negative hydrodynamic damping with increasing Reynolds number or reduced velocity till a point is reached where the total hydrodynamic damping becomes sufficiently negative to cause an amplitude up-shoot. It can be observed from the expression of hydro-dynamic damp-

ing in galloping in equation.

Rough cylinder oscillation frequencies are much lower than the Strouhal frequency values (shown by red lines in Figure 7.3) except at very low values of U*, irrespective of the value of K. This is primarily due to the effect of added mass.

The galloping instability is proportional to cylinder's cross-section geometry. In the case of a circular cylinder applied with the same configuration of PTC and system damping, galloping instability starts at the same flow speed ($U_{galloping}$). In this section, all experiments are conducted with rough cylinder (P60 PTC at 20deg to 36 deg), and the critical velocity for galloping occurs around U=1.0m/s ($Re_D= 8\times10^4$). Galloping vibratory amplitude can be fully developed in the following two different situations:

a) If the critical velocity for galloping (U^*_{gallop}) lays at flow speed range of smooth cylinder VIV upper branch (synchronization), the up-shooting amplitude response is observed immediately. The VIV-galloping transition is eliminated by the interaction effect from VIV and galloping. It can be seen on the results of K=1000N/m to 2000N/m (Figure 7.8 to Figure 7.14). In modeling of vortex-induced and galloping combined vibrations, when $U_{critical}$ is close to VIV (or even lower), galloping excitation amplitude is amplified by the effect of VIV.
b) Alternatively, for K=400N/m to 800N/m, the fully developed galloping does not occur till C_D undergoes a significant drop at the drag crisis. In this circumstance, a rougher PTC brings the C_D crisis to a lower Reynolds number (Figure 7.4, Achenbach and Heinecke 1981), in which galloping can be fully developed earlier. This result can be seen on the study of PTC roughness in Chapter 4, Figure 4.1.

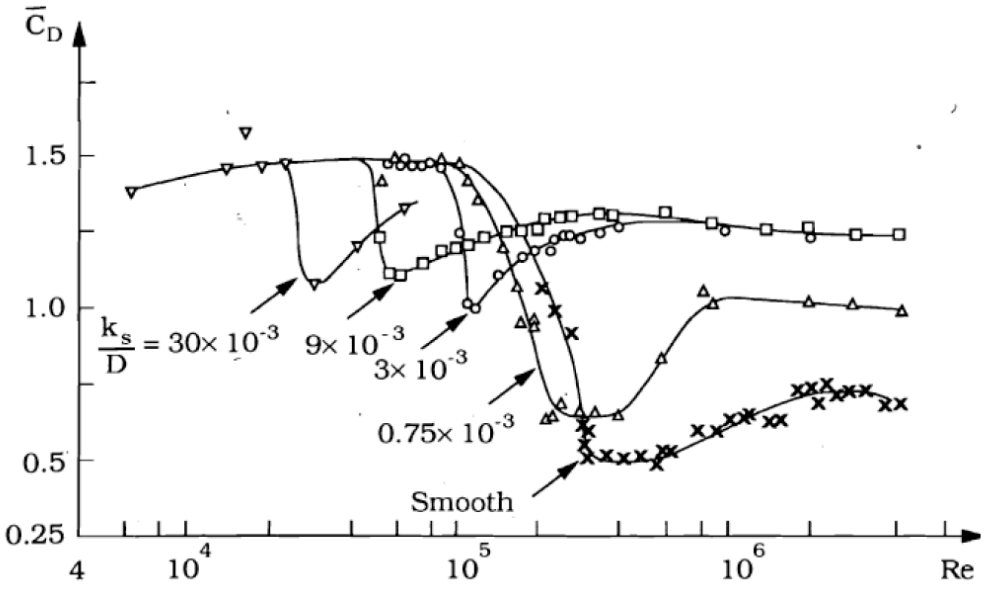

Figure 7.4. Drag coefficient of a circular cylinder at various surface roughness parameters ks/D. [Reproduced from Achenbach and Heinecke (1981)].

7.3. Effect of damping on the V_{ck} VIVACE with PTC

As mentioned in previous sections, for this study, roughness is selectively applied on the surface of a circular cylinder by attaching roughness strips having certain paper backing thickness. This alters the geometry of the cylinder to an effective non-circular cylinder section, and consequently exhibits oscillatory features, which are significantly different from those of a smooth cylinder. To specifically note, this has produced very high-amplitude response branches understood to be caused by galloping. Changing the externally imposed damping results in varied response characteristics of the system, which are presented and discussed in this section. This external damping is imposed on the oscillatory system by means of changing the torque of the motor in the V_{ck} system.

Effects of external damping on the oscillatory characteristics of the cylinder are illustrated in Figure 7.5 to Figure 7.22 at different stiffness values. The smooth cylinder response is also given in the background of these figures to facilitate analysis and discussion. Figure 7.5 presents the results at K=400N/m. In all the cases with roughness strips, it is found that, the synchronization range is broadened compared to that of the smooth

cylinder. An abrupt increase in oscillation amplitude takes place at about U*=17.8 for all the cases indicating galloping. Except for ζ_{harn}=0.16, at higher damping, lower is the excitation amplitude in the VIV synchronization range (initial and upper branches) also contribute to a sloping fully-developed galloping (less steeper) branch at U*~17.8. Surprisingly, for ζ_{harn}=0.16, amplitudes in the VIV regime are comparatively higher, which also exhibit a steeper galloping branch. Frequency of oscillation is not significantly influenced by the damping ratio in the VIV regime (Figure 7.14) except during the onset of oscillations where higher damping results in slower oscillations. However, in the galloping regime (U*>14.5), cylinder oscillation frequencies are affected by damping ratio as shown in Figure 7.14. In the range of VIV-galloping transition, 14.5≤U*≤18, higher damping ratios correspond to higher oscillation frequencies, whereas for U*>18 the trend is reversed. There is an abrupt drop off of frequency values at about U*~18 irrespective of the value of the damping ratio. Rough cylinders oscillate with a higher frequency than smooth cylinders for all the roughness values tested.

Specifically, due to the introduction of roughness, the VIV synchronization branch is extended (compared to the smooth cylinder). That is, roughness does help cylinder oscillations and thus energy is harnessed in two ways: (a) by extending the VIV synchronization range and (b) by promoting galloping. It is thought that, the roughness-boundary layer interaction contributes to the extension of the VIV synchronization range.

Figure 7.6 and Figure 7.7 show the response amplitudes at higher values of K, viz., 600N/m and 800N/m respectively illustrating the effect of damping. At these stiffness values, the relative amplitude trends are nearly the same as indicated by a decrease of response amplitudes in the VIV synchronization, while sloping down the galloping branch with increasing damping ratio. In general, roughness is seen to initiate early oscillations compared to the smooth cylinders as evidenced in Figure 7.6 and Figure 7.7. Furthermore, the higher the damping ratio, the greater is the separation between VIV and galloping branches. At lower damping ratios, the VIV branch smoothly merges with or collapses to the galloping branch. The maximum excitation amplitude is achieved for the lowest damping ratio, as expected. Results at still higher stiffness values (K=1000N/m, 1200N/m, 1400N/m, 1600N/m, 1800N/m and 2000N/m) are presented in Figure 7.8 to

Figure 7.13 for amplitude response and Figure 7.17 to Figure 7.22 for frequency response. The basic trends of amplitude and frequency variation are nearly the same as those of the lower stiffness values discussed in section7.2. Meanwhile, specific differences are observed between these cases as following. At higher stiffness values (at higher system damping ratios), a higher damping ratio (due to external damping) brings more distinct gradation to the amplitude characteristics. That is, the reduction between the amplitude values becomes wider both in the VIV as well as in the galloping regime, at higher stiffness values as demonstrated in Figure 7.8 to Figure 7.13. In addition, the maximum amplitude of oscillations undergoes a significant reduction at higher stiffness values particularly at higher damping ratios. It could also be noted that, the upper branch is more slopping when stiffness is increased.

As for frequency trends, some interesting features can be observed. To recall, for the case with lowest K value (=400N/m), up to about U*=8.5, a higher damping ratio brings slower cylinder oscillations (lower frequency). In the range $8.5 \leq U^* \leq 15.0$, oscillation frequency does not exhibit any gradation with respect to damping ratio. Further in the range of $15 \leq U^* \leq 18$, a higher damping ratio increases the oscillation frequency (trend is reversed) and then, for $U^* > 18$, the trend is set back to the VIV initial regime. That is, there are trend frequency reversals as the reduced velocity is progressively increased. Similar to amplitude gradation noticed at higher stiffness values, frequency values also become more distinct and separate (without collapsing) at higher damping ratios both in the VIV and galloping regimes; collapse of frequency values at different damping ratios can be clearly seen in Figure 7.14 particularly in the VIV regime. Also, the frequency distribution becomes more non-uniform at higher damping ratios. Up to K=1600N/m, rough cylinder oscillation frequencies are lower than those of the smooth cylinder in the VIV regime for all damping ratios tested. But, at still higher K values, oscillation frequency at the highest damping ratio (ζ_{harn}=0.16) is lower than that of the smooth cylinder, registering a significant drop in the VIV regime.

Basically, when a cylinder undergoes flow-induced motion, there operates a feedback mechanism between the oscillating body and the wake (Bishop and Hassan 1964). The physics of the fluid-structure interaction involved is understood to be highly non-

linear in nature (Benaroya & Gabbi 2008). With the introduction of surface roughness (PTC), additional complexities are brought in to the feedback system via roughness-boundary layer interaction. To clarify, with PTC introduction and the body geometry being changed, flow structures become asymmetric with changing flow incidence angle possibly inducing negative hydrodynamic damping. Needless to say, the oscillations are also very much dictated by reduced velocity and free stream turbulence intensities (if any). The resulting oscillations described in this section are thus a function of all these parameters apart from the externally imposed damping element.

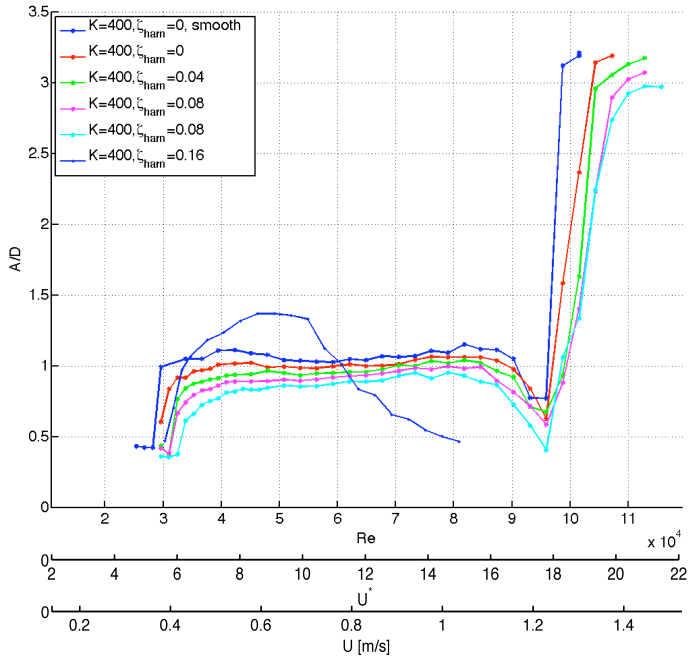

Figure 7.5. Rough cylinder amplitude response at various damping values at K=400N/m.

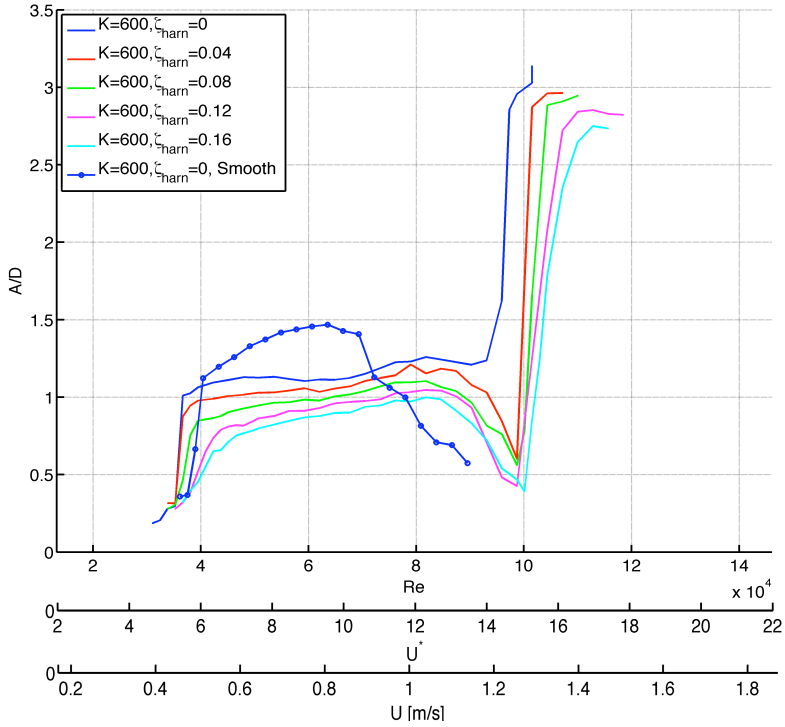

Figure 7.6. Rough cylinder amplitude response at various damping values at K=600N/m.

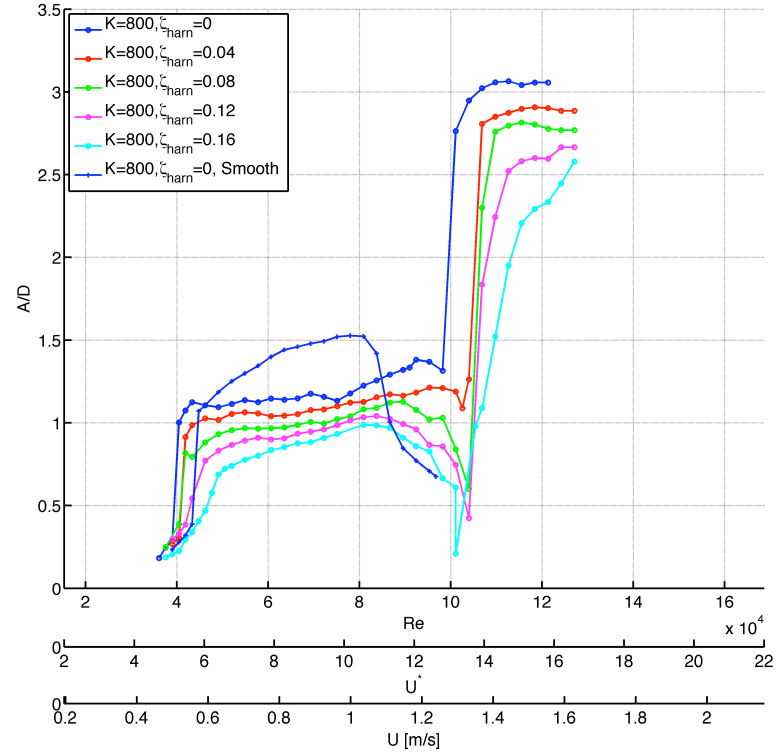

Figure 7.7. Rough cylinder amplitude response at various damping values at K=800N/m.

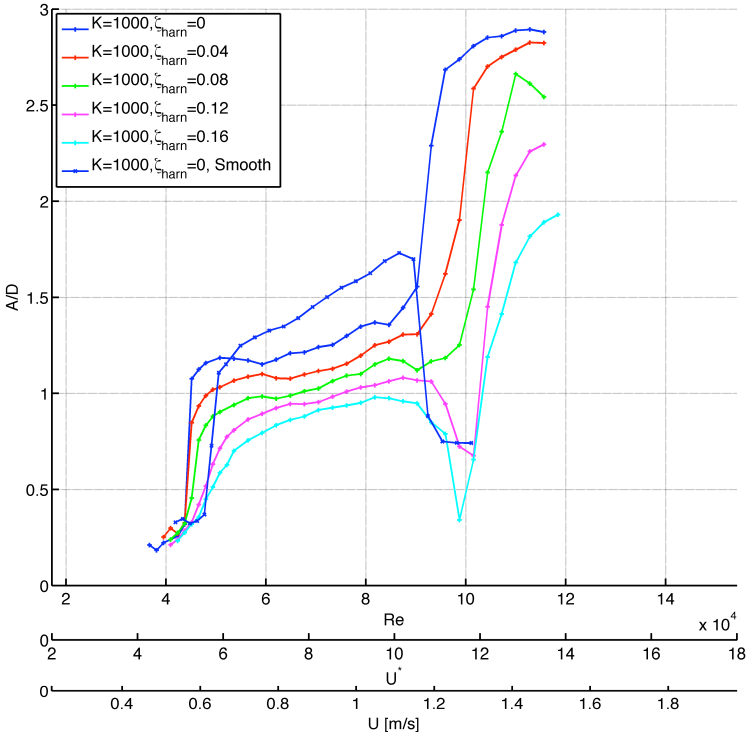

Figure 7.8. Rough cylinder amplitude response at various damping values at K=1000N/m.

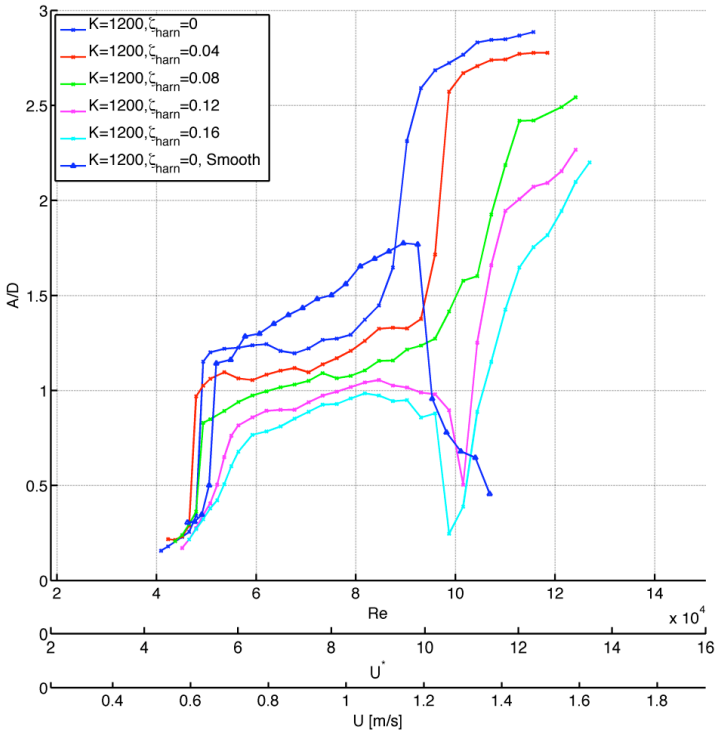

Figure 7.9. Rough cylinder amplitude response at various damping values at K=1200N/m.

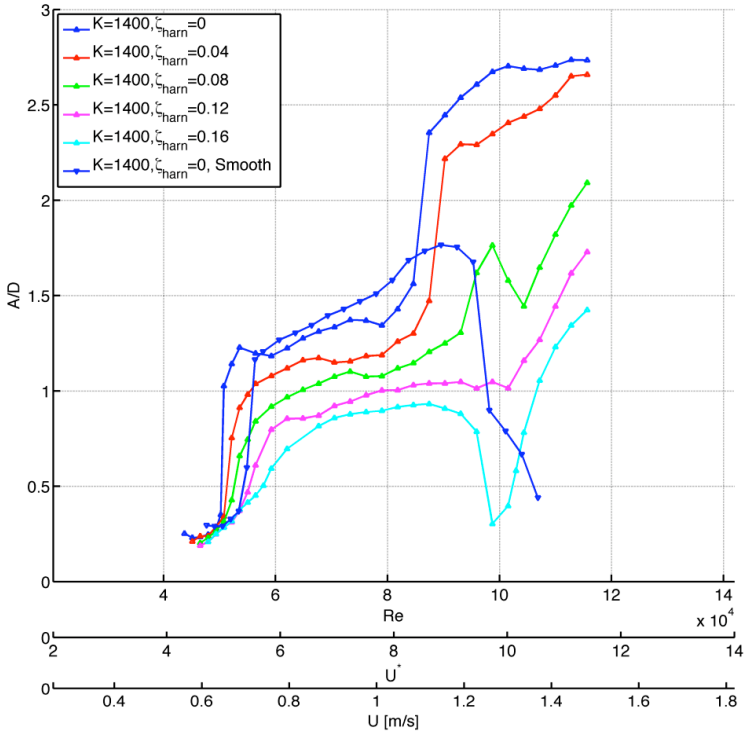

Figure 7.10. Rough cylinder amplitude response at various damping values at K=1400N/m.

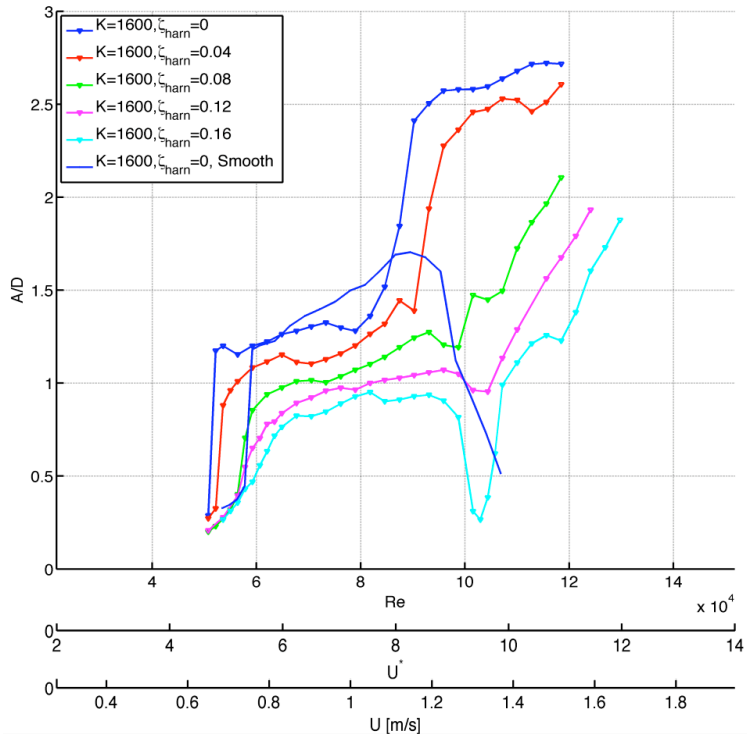

Figure 7.11. Rough cylinder amplitude response at various damping values at K=1600N/m.

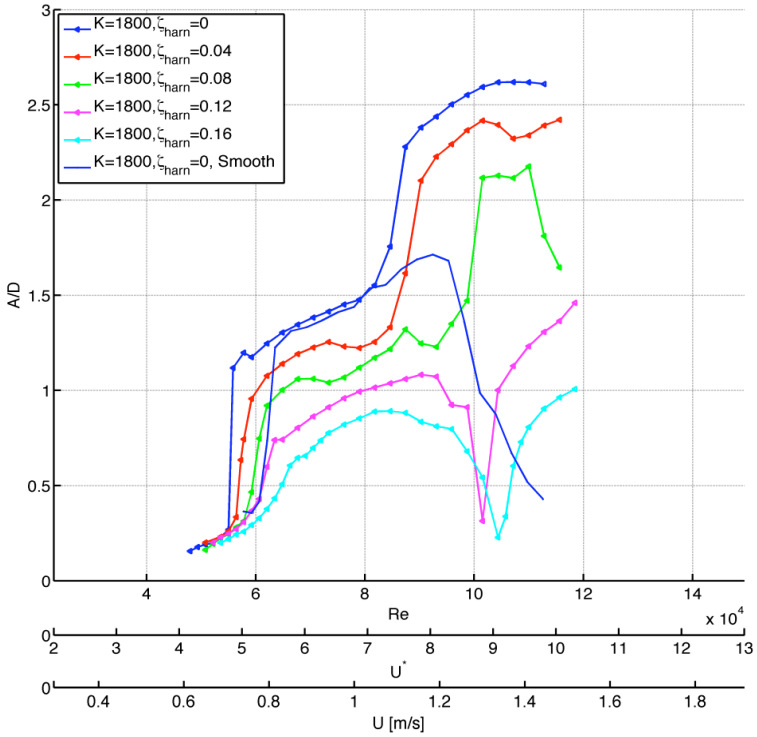

Figure 7.12. Rough cylinder amplitude response at various damping values at K=1800N/m.

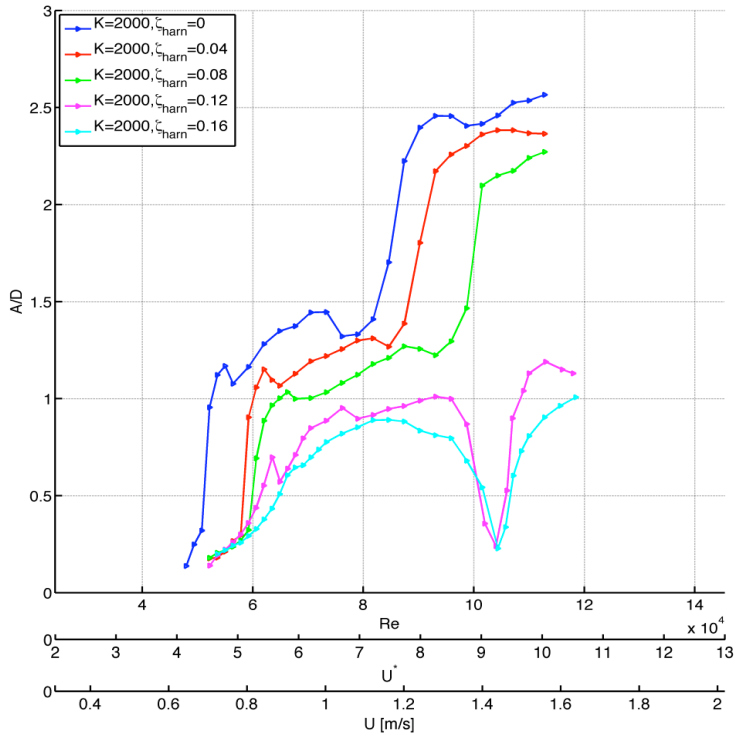

Figure 7.13. Rough cylinder amplitude response at various damping values at K=2000N/m.

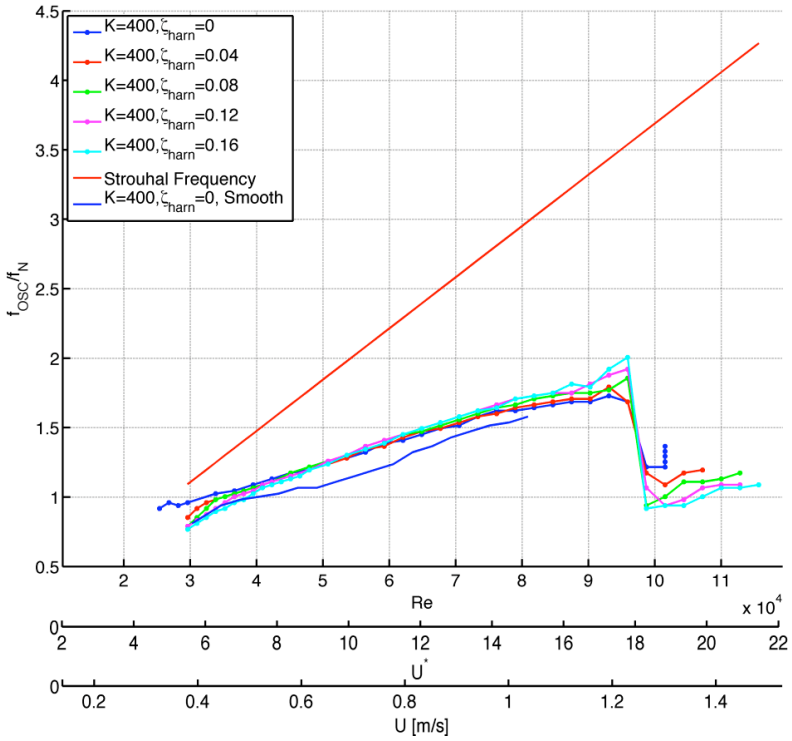

Figure 7.14. Rough cylinder frequency response at various damping values at K=400N/m.

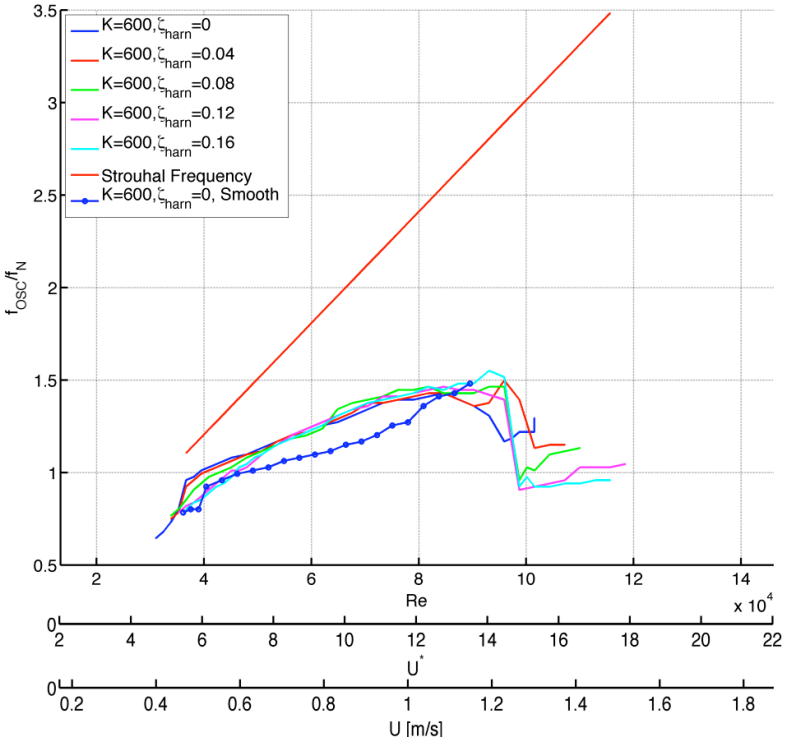

Figure 7.15. Rough cylinder amplitude response at various damping values at K=600N/m.

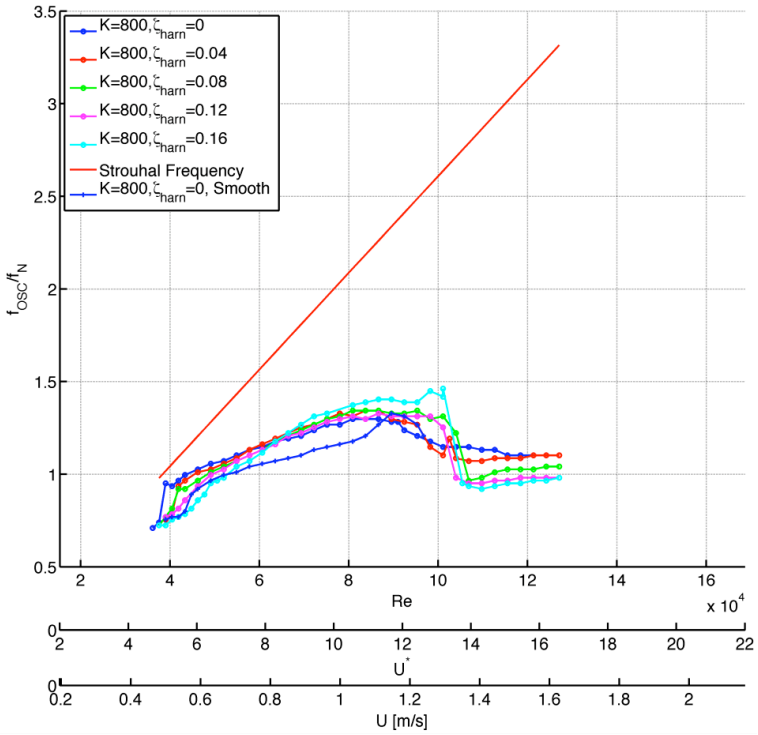

Figure 7.16. Rough cylinder amplitude response at various damping values at K=800N/m.

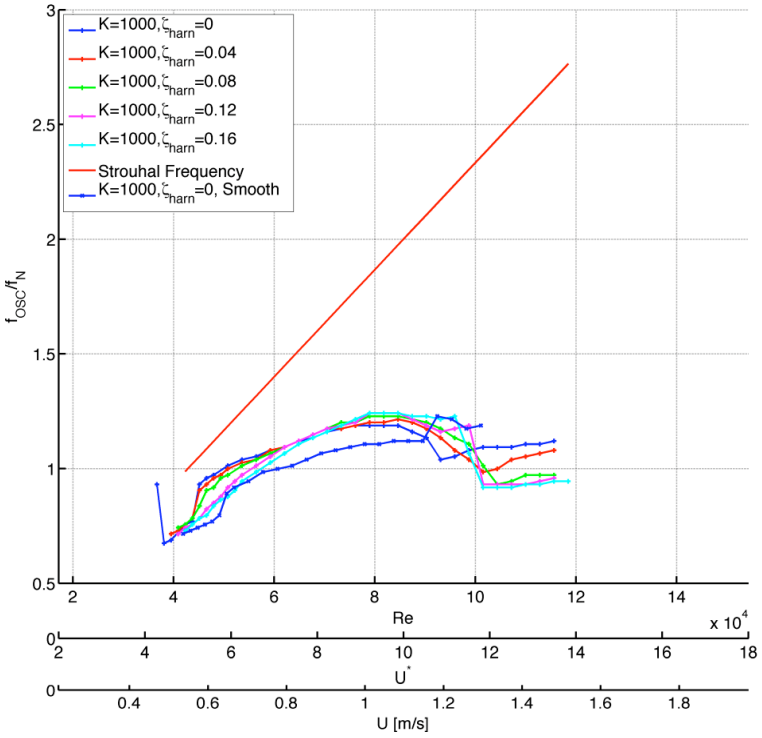

Figure 7.17. Rough cylinder amplitude response at various damping values at K=1000N/m.

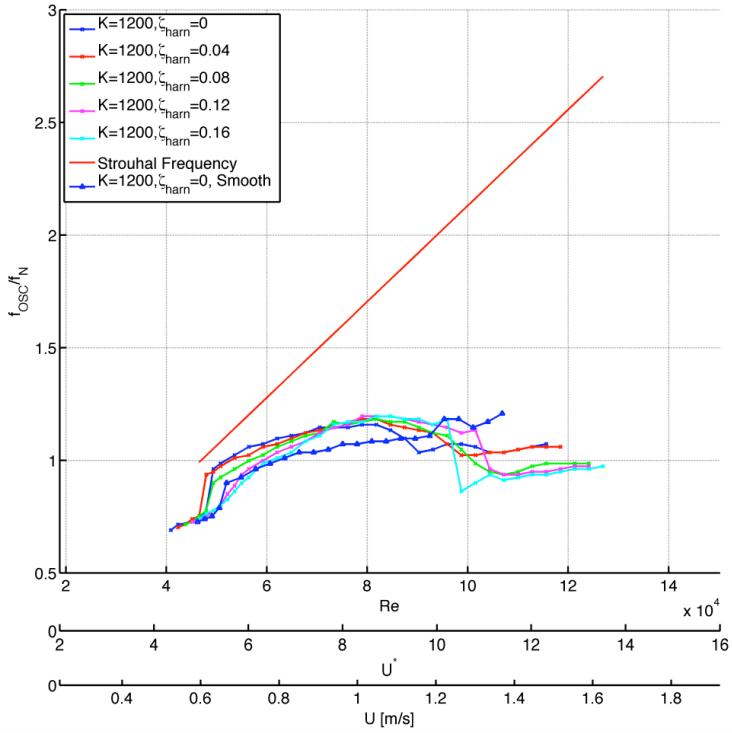

Figure 7.18. Rough cylinder amplitude response at various damping values at K=1200N/m.

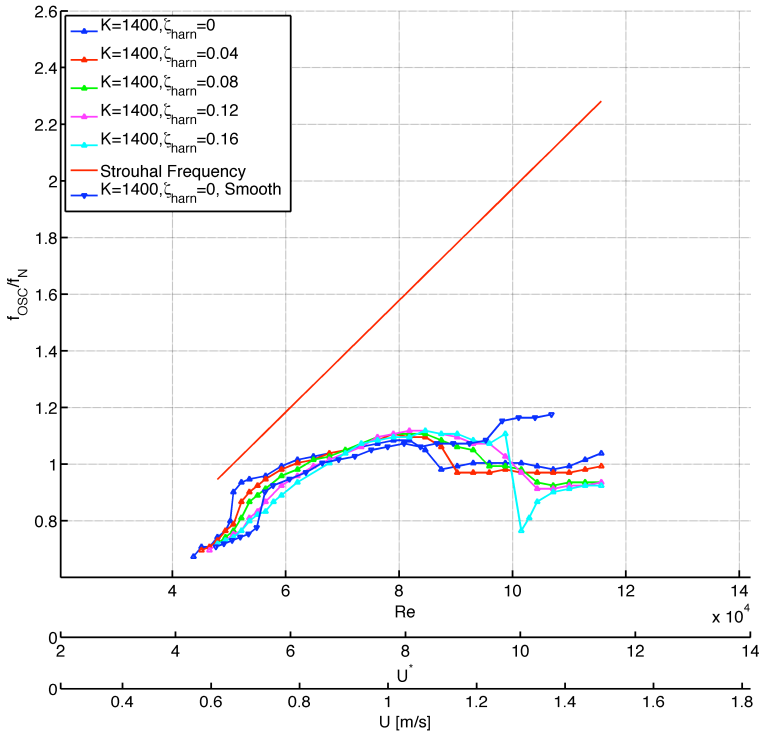

Figure 7.19. Rough cylinder amplitude response at various damping values at K=1400N/m.

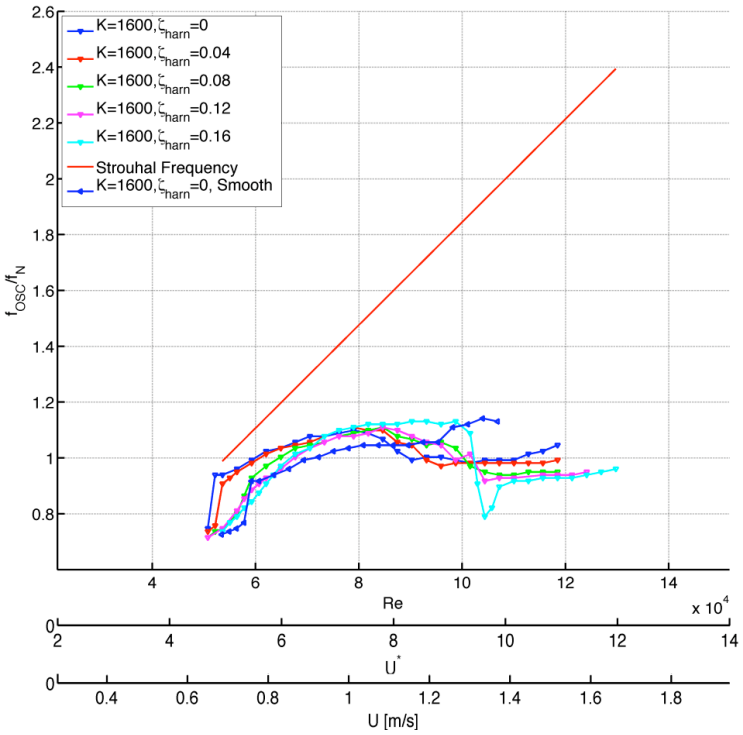

Figure 7.20. Rough cylinder amplitude response at various damping values at K=1600N/m.

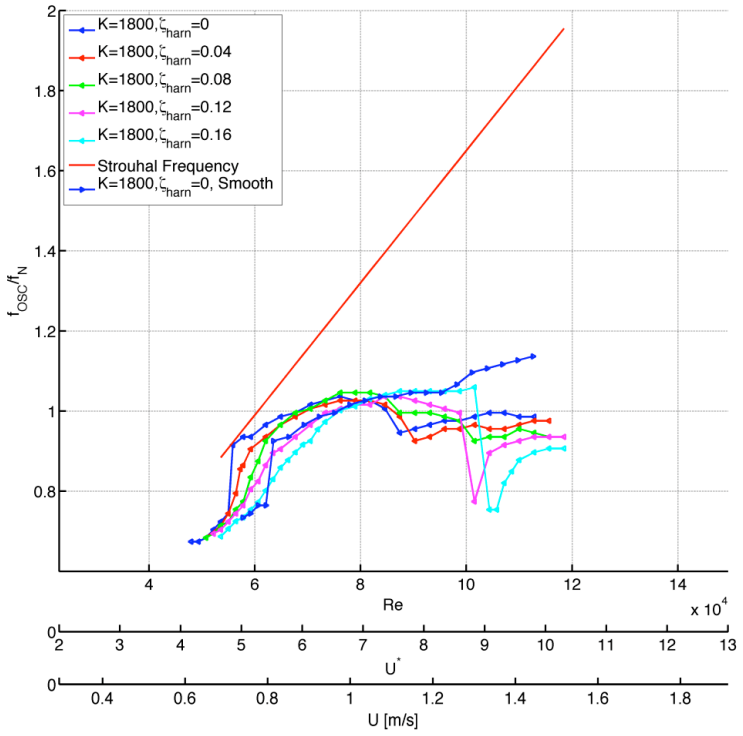

Figure 7.21. Rough cylinder amplitude response at various damping values at K=1800N/m.

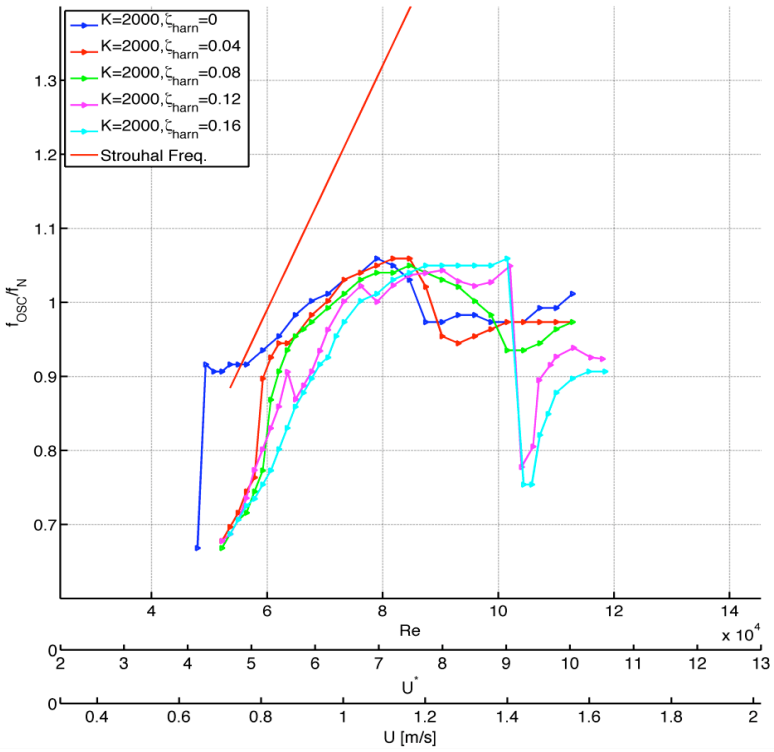

Figure 7.22. Rough cylinder amplitude response at various damping values at K=2000N/m.

7.4. Conclusions

From the study in this chapter, the following conclusions are drawn:

a) The external damping significantly influences the cylinder oscillatory characteristics, viz., amplitude, and frequency features.

b) Changing spring stiffness brings considerable changes to the cylinder oscillatory features, even in the absence of external damping. Increasing stiffness decreases the VIV synchronization range in terms of Reynolds number. Furthermore, it also reduces the maximum attainable galloping amplitude. Higher stiffness delays the onset of oscillations in terms of Re.

c) The higher the stiffness, the more gradual is the transition from VIV to galloping type of oscillation.

d) Oscillation frequency first increases and then, drops to lower values with a progressive increase in reduced velocity in all the rough cases tested irrespective of the stiffness value.

e) In all the rough cylinder cases, excitation amplitudes are lost in the VIV regime followed by significant amplitude gain thereafter due to galloping promoted by change of geometry.

f) Irrespective of the value of spring stiffness, the general rough cylinder oscillatory trends are similar to first VIV regime characterized by an initial and upper branches followed by galloping.

g) Lower stiffness, amplitude and frequency values at different damping ratios show greater collapse on each other. At a very high stiffness value, significant differences are observed between amplitude values at various damping ratios both in the VIV and galloping regimes. The same concept applies to frequency values as well.

h) As the reduced velocity is progressively increased, the reversal occurs in the frequency trend with respect to damping ratio.

CHAPTER 8

POWER DENSITY CALCULATION AND ASSESSMENT

8.1. Background

This chapter presents a comparison between energy sources by using a universal metric, the footprint power density. The mathematical model for the harnessed and dissipated power is summarized in the beginning of Section 8.2. The expression for various stages of available power and VIVACE energy density are calculated and presented later in section 8.3. Power density is also calculated and optimal power envelope is generated.

8.2. Mathematical model of harnessed and dissipated power

In this section, the mathematical model for harnessed and dissipated power is summarized. Let us consider a simplified configuration, which consists of a spring-mounted body (cylinder) in FIM under the action of an incoming flow in the transverse direction. The motion of the cylinder in y-direction, which is the direction perpendicular to the flow and cylinder axis, is modeled by a 2nd order linear differential equation as

$$(m_{osc} + m')\ddot{y} + c_{total}\dot{y} + Ky = F_{fluid}\hat{y} \tag{8.1}$$

Note that a V_{ck} VIVACE is used to complete the experiments in this section. A virtual stiffness is used in expression. (Please see Chapter 8 and 9 for more detail and discussion on mathematical model of VIV and galloping)

In order to to calculate the MHK energy that can be harnessed, an additional damping is introduced into the system. The total damping coefficient (c_{total}) is defined as

$$c_{system} = c_{structure} + c_{harness}, \tag{8.2}$$

where $c_{structure}$ is the excisting damping coefficient due to losses in the transmission system, $c_{harness}$ is as the damping coefficient added through the generator to converts the mechanical energy in the oscillating cylinder to electrical energy simulating the real world. The equation of motion of the V_{ck} VIVACE model dynamics is:

$$(m_{osc} + m')\ddot{y} + c_{system}\dot{y} + K_{virtual}y = F_{fluid}\hat{y} \tag{8.3}$$

Next, based on the information provided in equation (8.3), we further integrate the left hand side after multiplying it by the instantaneous velocity and average it over one cycle of period T_{osc} to obtain the total mechanical power in the VIVACE converter as

$$P_{mechinical} = \frac{1}{T_{osc}}\int_0^{T_{osc}}[(m_{osc} + m_a)\ddot{y} + (c_{structure} + c_{harness})\dot{y} + ky]\dot{y}dt \tag{8.4}$$

We can assume that the VIV and galloping responses are approximately sinusoidal as shown in Figure 11.8. The only non-zero term in Equation (8.4) on the left hand side will be the velocity term. This results in the mechanical power of V_{ck} VIVACE converter:

$$P_{mechinical} = \frac{1}{T_{osc}}\int_0^{T_{osc}}(c_{structure} + c_{harness})\dot{y}^2 dt \tag{8.5}$$

From Equation (8.5), we obtain the harnessed power and the dissipated power as:

$$P_{harness} = \frac{1}{T_{osc}}\int_0^{T_{osc}} c_{harness}\dot{y}^2 dt \tag{8.6}$$

$$P_{dissipated} = \frac{1}{T_{osc}}\int_0^{T_{osc}} c_{structure}\dot{y}^2 dt \tag{8.7}$$

The harnessed power in V_{ck} system is dissipated at a heat bank (resistor box) and it is assumed as available electrical power in real life design of VIVACE.

Note that, the method for calculating harnessed power in this section is different from what has been presented in Chapter 7. For the V_{ck} system, the real time velocity signal can be recorded by embedding an encoder inside the motor. All cycles over the recorded time period (60 second) are used to calculate the harnessed/dissipated power.

8.3. Harnessed power calculation using experimental results

In this dissertation, five $\zeta_{harness}$ values ($\zeta_{harness}$=0.04, 0.08, 0.12 and 0.16) and nine virtual stiffness values ($K_{virtual}$ =400, 600, 800, 1000, 1200, 1400, 1600,1800 and 2000N/m) are used in experiments to study energy harnessing. The corresponding damping coefficient (C_{total}) values are shown in Table 10. All tests are conducted at the LTFSW Channel and the flow speed varies from 0.35m/s to 1.51m/s. (Re: $2.5 \times 10^4 \sim 1.18 \times 10^5$, D=3.5") Test information is also listed in Table 11.

TABLE 10. DAMPING C_{TOTAL} VALUES FOR VARIOUS VALUES OF $\zeta_{HARNESS}$ AND K

ζ_{total}	400N/m	600N/m	800N/m	1000N/m	1200N/m	1400N/m	1600N/m	1800N/m	2000N/m
0	2.40	2.40	2.40	2.40	2.40	2.40	2.40	2.40	2.40
0.04	7.69	8.88	9.89	10.77	11.57	12.31	12.99	13.63	14.24
0.08	12.99	15.37	17.38	19.14	20.74	22.21	23.58	24.86	26.08
0.12	18.28	21.85	24.86	27.51	29.91	32.12	34.17	36.09	37.92
0.16	23.58	28.34	32.35	35.89	39.08	42.02	44.76	47.33	49.76
in Ns/m									

TABLE 11. SYSTEM INFORMATION FOR STUDY OF HARNESSED AND DISSIPATED POWER ON V_{CK} VIVACE

Operating system	Virtual damping-spring VIVACE converter
D: diameter of circular cylinder (m)	0.0889 (3.5" cylinder)
L: length of cylinder (m)	0.9144
$U_{current}$: flow velocity range (m/s)	0.35 to 1.51
Re_D: Reynolds number range	$2.5 \times 10^4 to 1.2 \times 10^5$
Aspect ratio	10.29
m_{osc}: total mass of oscillation (kg)	10.75
m_{eff}: effective mass (kg)	2.05
m_d: displaced mass (kg)	5.67
m*: mass ratio	1.88
K: stiffness (N/m)	400 to 2,000
$f_{n,water}$: natural frequency in water (Hz)	0.78 to 1.76
$C_{structure}$: structural damping (Ns/m)	3.2
ζ_{harn}: extra damping ratio for energy harnessing (Ns/m)	0.04, 0.08, 0.12, 0.16
PTC roughness (type)	P60 (k=0.26mm, p=0.587mm)
PTC location (degree)	20 to 36 (1/2" wide)

For each combination of $\zeta_{harness}$ and K, the harnessed power ($P_{harness}$) and the dissipated power (P_{dissip}) are calculated using a trapezoidal integration scheme with a 0.01sec time step, which is the resolution of a recorded signal. An average of sequential 30 cycles of time history of harnessed/dissipated power are presented as $P_{harness}$ and P_{dissip} for each stiffness value K. Results of harnessed power from VIVACE with PTC versus Reynolds number (Re), reduced velocity (U*), and flow speed (U) are shown in Figures 8.1 to 8.17. Smooth cylinder results by Lee (2009) are superposed for comparison. Following observations can be made from the results presented:

a) Overall, power is harnessed over a broader range of velocity from 0.38m/s to 1.56m/s.
b) Comparing to VIVACE with smooth cylinder (Lee, 2009), VIVACE with PTC and low value of stiffness harnesses energy from a lower flow speed with lower value of stiffness in the system.
c) Comparing to VIVACE with smooth cylinder (Lee, 2009), under all the test values of stiffness, when $\zeta_{harness}$=0.04 and $\zeta_{harness}$=0.08, the harnessed energy of VIVACE with PTC is consistently higher.
d) At the beginning of the VIV range (the initial branch), it can be seen that, for all values of K, the lower the $\zeta_{harness}$ of the system, the higher the energy harnessed.
e) For VIVACE with PTC, the maximum value of harnessed energy corresponds to a damping value of $\zeta_{harness}$=0.16; whereas for smooth cylinder VIVACE, the maximum energy is harnessed at a lower damping value of $\zeta_{harness}$=0.12.
f) For tests within stiffness values 400N/m, 600N/m and 800N/m, the quantum of harnessed energy significantly drops in the flow speed interval from 1.2m/s to 1.38m/s ($9.3\times10^4 \leq Re \leq 1.1\times10^5$). An increase in the value of stiffness corresponds to a higher speed for VIV synchronization. More energy can be harnessed utilizing galloping-VIV associated vibrations as can be seen in Figure 8.2 to Figure 8.14. VIVACE with higher value of stiffness generates more energy during the transition range from VIV to galloping before galloping becomes fully developed.
g) On the commencement of fully-developed galloping, a greater level of energy can be generated by increasing the value of damping. The maximum of stiffness value and damping value in our parametric space are limited to K=2,000N/m and $\zeta_{harness}$=0.16, respectively. In addition, the fastest flow speed achievable in the LTFSW Channel is

1.5m/s. These are functional limitations of our device. The maximum value of harnessed power could be noted from Figure 8.17 as 48W which corresponds to K=2,000N/m and $\zeta_{harness}$=0.08. In summary, an even greater level of energy can be harnessed with higher damping level or a greater stiffness value at higher flow speeds provided the experimental model is adequately modified. This result certainly warrants future investigation.

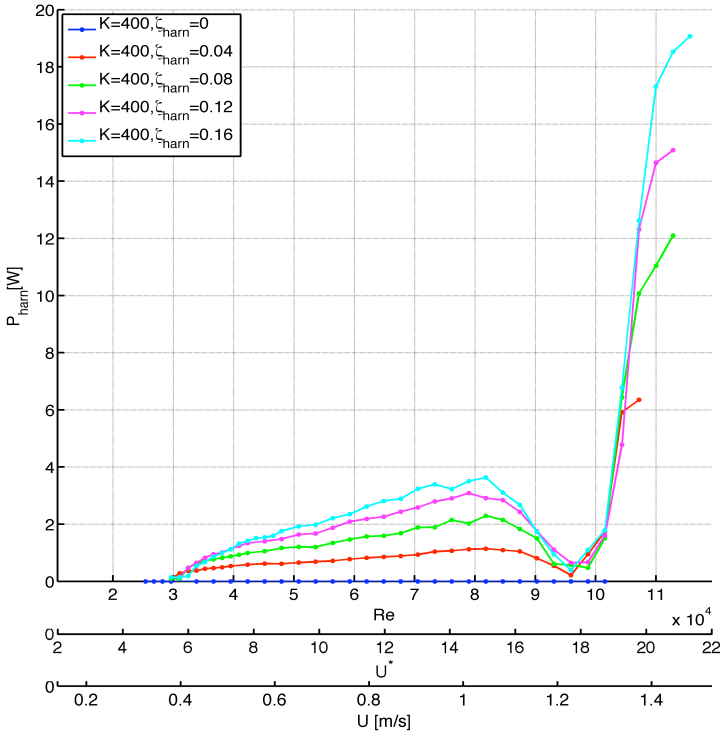

Figure 8.1. Averaged P_{harn} of VIVACE with PTC for K=400N/m.

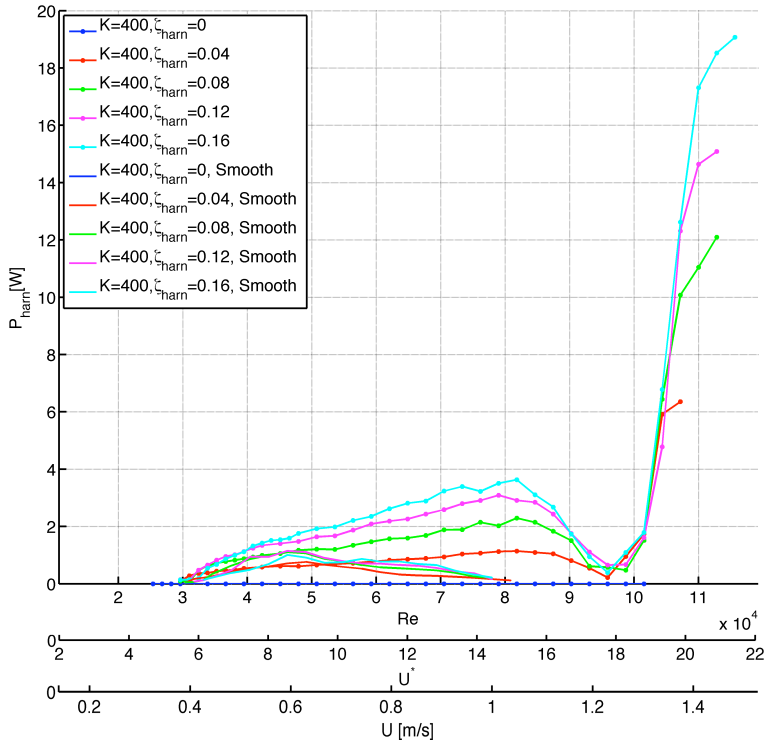

Figure 8.2. Averaged P_{harn} of VIVACE with/without PTC for K=400N/m.

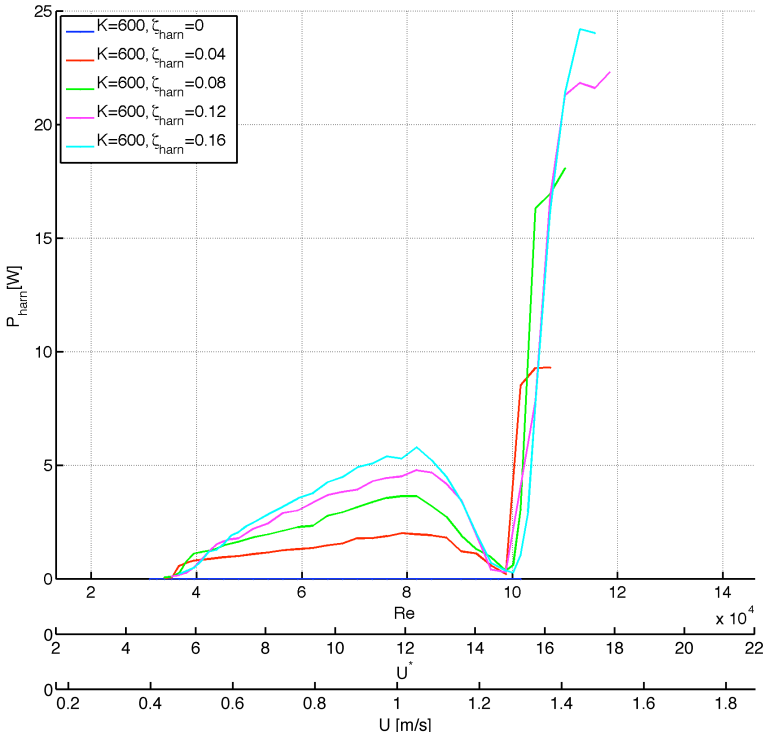

Figure 8.3. Averaged P_{harn} of VIVACE with PTC for K=600N/m.

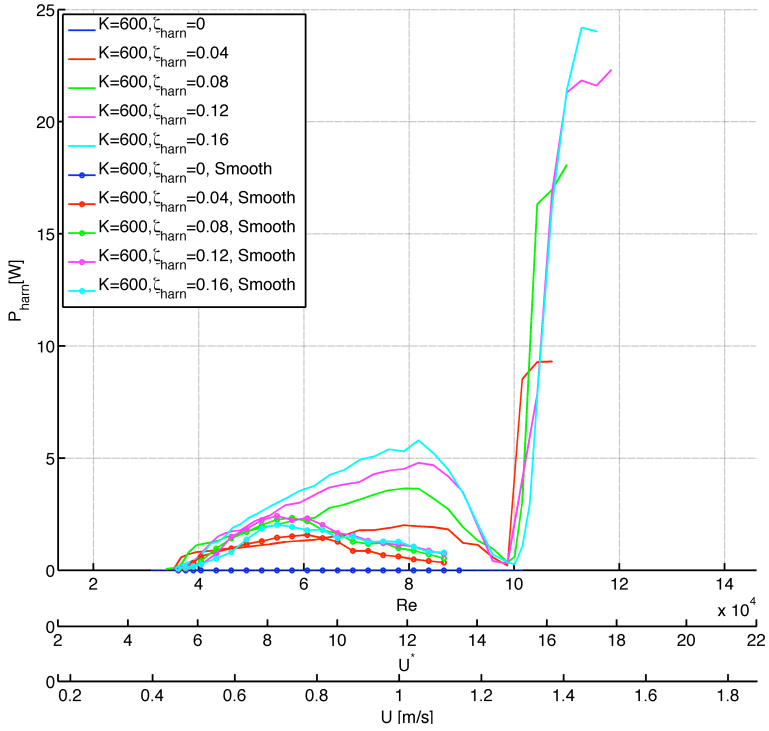

Figure 8.4. Averaged P_{harn} of VIVACE with/without PTC for K=600N/m.

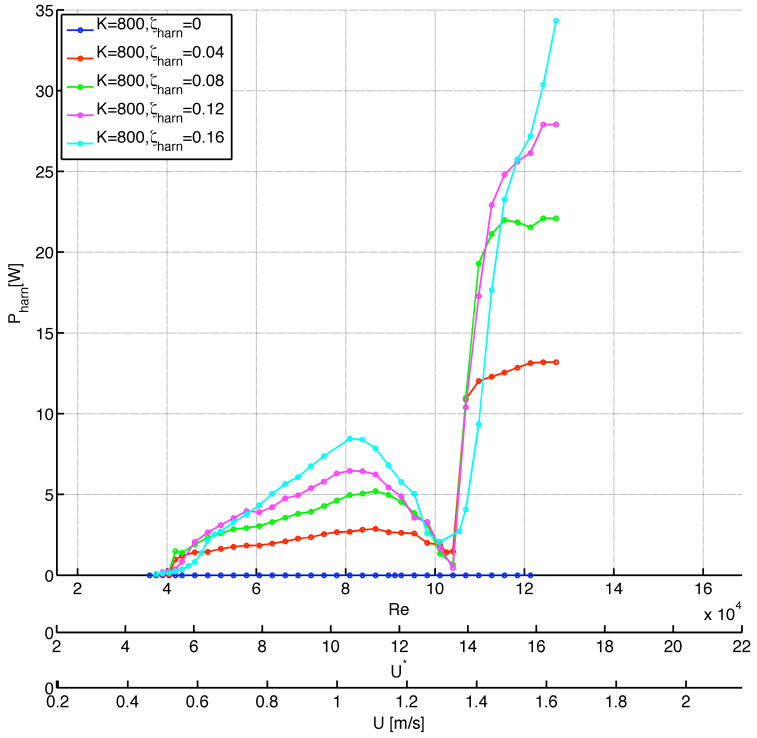

Figure 8.5. Averaged P_{harn} of VIVACE with PTC for K=800N/m.

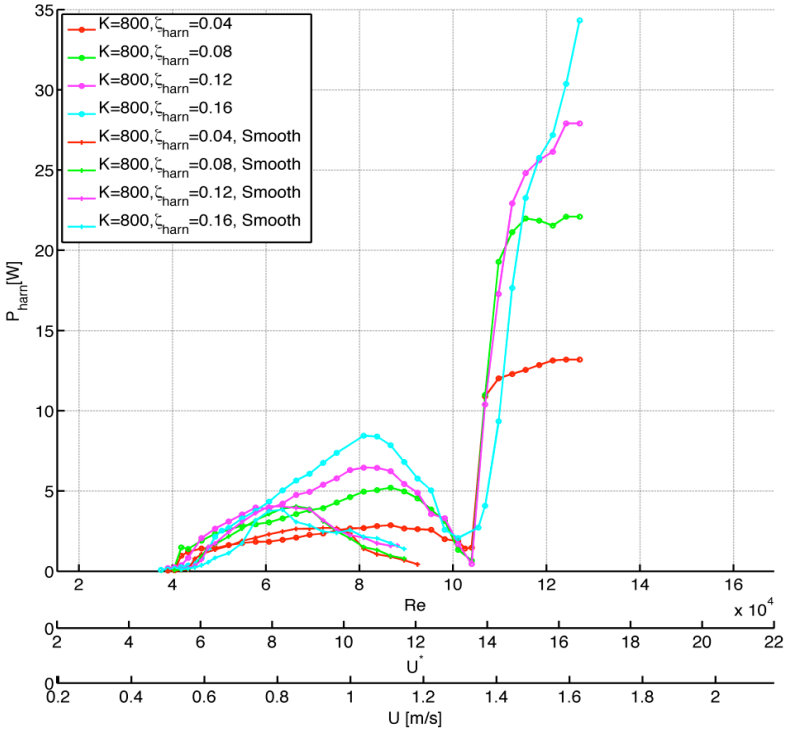

Figure 8.6. Averaged P_{harn} of VIVACE with/without PTC for K=800N/m.

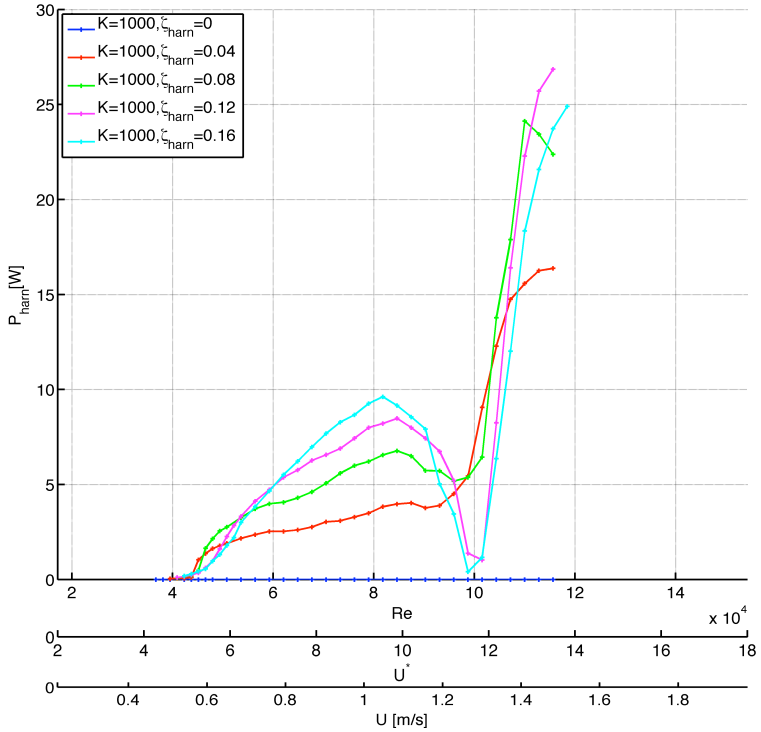

Figure 8.7. Averaged P_{harn} of VIVACE with PTC for K=800N/m.